Single Cell Transcriptomics Reveals the Hidden Microbiomes of Human Tissues

Gita Mahmoudabadi[1], Sheela Crasta[2], Tabula Sapiens Consortium[3], Stephen R. Quake[1,2,4,*]

[1]Department of Bioengineering, Stanford University, Stanford CA, USA
[2]Authors and their affiliations are listed at the end
[3]Department of Applied Physics, Stanford University, Stanford CA, USA
[4]Chan-Zuckerberg Initiative, Redwood City CA, USA
*Corresponding author. Email: steve@quake-lab.org

Abstract

The human microbiome has been studied extensively across those sites in the body that are readily accessible to sampling. Internal organs and tissues, however, have remained largely unexplored and, in the absence of infectious disease, are widely assumed to be free of microorganisms. Using single-cell transcriptomic data from the Tabula Sapiens spanning 11 human organ donors, 19 tissue types, 400,000+ annotated cells, 100+ cell types, and ~70 billion sequences, we created an atlas of the human tissue microbiome with cell type resolution across three domains of life which we refer to as the Tabula Sapiens Microbiome. Together with data from 8 additional donors derived from a different set of experimental techniques for validation, we identified sequences from numerous bacterial, viral and fungal species in human tissues. We mapped the likely microbial flow routes in the body from external-facing microbiomes and natural environments to internal tissues and tumors, demonstrating the existence of several unexpected routes. In the case of tumor microbiomes, we find a considerable number of bacterial genera found in tumors are detectable across tumor-free tissues, suggesting that tumor microbiomes are in part sourced from adjacent normal tissues, even those from distant sites. Finally, by increasing the resolution of sampling from tissues to cell types, we quantified the microbial load and diversity across different human cell types to reveal a network of host cell type and microbe associations. For example, we identified traces of both latent and active Epstein Barr Virus infections in various cell types such as splenic plasma cells. Broad exploration of the human tissue microbiomes may provide insights which ultimately are of clinical importance.

Introduction

Microbial life contains a vast repertoire of biochemical pathways that enable it to colonize even the most extreme environments on the planet. It is no wonder that the human body, an energy-rich environment for trillions of our own cells, would be host to many highly diverse microbes[1,2]. Historically, understanding of microbes in connection to human health has emerged from waves of encounters with devastating pathogens such as *Mycobacterium tuberculosis*, *Vibrio cholerae*, and most recently, SARS-CoV2. In the last two decades our view of human-microbe interactions has been transformed through increasingly powerful sequencing technologies which have enabled broad surveys of the microbial world[3–8]. As such, previously held dogma has been upended; one such example of this is the assertion that internal organs such as the healthy human lung are sterile environments[9].

The study of the human microbiome has seen an explosion of data connecting communities of microbes or individual species to a variety of metabolic[10,11], neurological[12,13], cardiovascular[14,15], and autoimmune[16,17] diseases, among others. Most

microbiome studies, however, have delineated microbial communities at sites easily accessible to sampling such as the human intestinal tract via feces, the mouth, and the skin. Less accessible internal sites, on the other hand, are largely assumed to be free of microorganisms, as they are protected by layers of epithelial and endothelial tissue. However, a few recent studies have challenged this assumption. For example, human tumors were shown to contain tumor-specific microbial sequences, providing a possible diagnostic approach for cancer detection[18]. Other studies similarly identified the presence of tumor-specific mycobiomes and microbiomes including intracellular bacteria[19–24]. Microbiomes in both tumor-free and tumor-derived breast, esophageal, oropharyngeal, gastrointestinal, and colorectal tissues have also been shown[25–27].

We assembled the first atlas of human tissue and cell type microbiomes by mining the raw sequences from one of the largest single-cell transcriptomic datasets of human tissues called the Tabula Sapiens[28] which encompasses 400,000+ annotated human cells, spanning 100+ cell types and 19 tissues, originating from 11 human organ donors. We identified high-confidence viral, bacterial, and fungal sequences originating from human single-cell transcriptomes, together forming the Tabula Sapiens Microbiome (TSM) dataset. Using a series of experimental and bioinformatic filters including a machine learning model for decontamination and a Large Language Model for habitat classification, we rigorously decontaminated and quality controlled this dataset.

Moreover, we combined our data with 16 external datasets (**SI Figure 1.a-b**), 10 of which were used for creating and benchmarking a pipeline for the identification of microbial sequences. Some examples of these databases include the Human Gastrointestinal Bacteria Culture Collection (HBC)[29], the expanded Human Oral Microbiome Dataset (HOMD)[30], Human Microbiome Project (HMP)[4], and others. The other external databases, including Narunsky-Haziza *et al*.[20] (tumor mycobiomes), Nejman *et al.* (tumor microbiomes)[21], the Unified Human Gastrointestinal Genome[5] (UHGG) collection, Genomes from Earth's Microbiomes (GEM)[7], Pathosystems Resource Integration Center (PATRIC)[31], and others were used for decontamination and analysis. For example, we explored the intersection of species in TSM tissues and those found at tumor sites and at sites accessible to sampling, or what we will refer to as "external-facing microbiomes" (e.g. the gastrointestinal, oral and skin microbiomes), as well as natural environments, to chart out possible microbial flow routes throughout the body. We report the inter-and intra-donor variability of tissue microbiomes and characterize microbial load and diversity across human cell types. Moreover, using an additional cohort of 8 donors, we devised an assay to extract virus-like and bacterial-like particles from human tissues and explored them using imaging and DNA sequencing. We will refer to this dataset as the Extracted Human Tissue Microbiome (EHTM) dataset. We further show that the human tissue and

cellular microbiomes, beyond cell-free or capsid-free nucleic acids, may also include intact organisms.

Results

Computational pipeline for identification of microbial sequences from multiple biomes in single-cell datasets

We created a computational pipeline written in Snakemake[32] to identify viral, bacterial and fungal sequences in single-cell transcriptomic data. Briefly, we use UMI-tools[33] to filter and extract cell barcodes and UMIs from fastqs, and then use STAR[34] to align resulting sequences against a reference library containing the human genome and ERCCs. After the removal of low-complexity sequences from the unmapped reads using a custom script, we use BLASTn[35] to align reads against several custom databases followed by the nt database, which is one of largest publicly available databases. We refer to this pipeline as SIMBA. For a more detailed description of this pipeline see **SI: SIMBA, a computational pipeline for the identification of bacteria, viruses and fungi in single cells,** along with **SI Figure 1.a.** We also benchmarked this pipeline against several truth datasets to show that it is highly precise **(**see **SI: Benchmarking SIMBA's precision and recall** as well as **SI Tables 1-8).** We provide a full explanation for why we chose not to rely on faster aligners or smaller reference databases given their higher false positive rates in samples that have low ratios of non-host to host sequences (See **SI: SIMBA, a computational pipeline for the identification of bacteria, viruses and fungi in single cells,** as well as **SI: Benchmarking Kraken2 precision and recall,** as we all as **SI Tables 9-11** and **SI Figure 2)**. A common theme in our study is that in the tug-of-war between precision and recall, we choose precision as we decided it was more important to us to identify microbial reads precisely and with high confidence than it was to capture more of them.

Decontamination and quality filtering of the Tabula Sapiens Microbiome dataset

In the previous section and its supplementary material, we address a major source of false positives in microbial datasets, which are false positives generated during alignments. Another important source of false positives is physical contamination. We discuss in depth the measures taken during tissue procurement and transport to prevent potential contaminants (see **SI: Measures against contamination during tissue recovery and transport)**. We acquired samples of reagents and instruments that were used to process tissues and sequence single cells. Even when the same reagent was

used across different labs, we obtained each lab's specific sample of that reagent to account for lab-specific contaminants. Following the same protocols as the original experiments, we deeply sequenced more than 200 reagent and instrument controls using five 10X lanes (**SI Table 12**), and eliminated contaminant species (filter 1). We then eliminated putative bacterial (filter 2) and fungal (filter 3) contaminants previously identified by Salter *et al.*[36] and Narunsky-Haziza *et al*[20]. For a detailed description of these three filters and their impact on the dataset, see **SI: Identification of contaminants based on negative controls and external datasets** and **SI Tables 12-13**.

To further account for any potentially missed contaminants, we built 6 types of machine learning models to learn the shared features of the known and putative contaminants acquired from the first three filters. As our fourth filter, we applied the best performing model type, which was the gradient boosting classifier (test AUPR and AUROC 95% confidence intervals were 0.75-0.78 and 0.82-.84, respectively) to identify putative contaminants in the portion of the dataset that was withheld from both training and testing (see **SI: Machine learning models of contamination, SI Tables 14-15** and **SI Figure 1.c-d**). Additionally, we observed a bimodal distribution of alignments and removed species that are represented primarily by the lower-quality alignment peak, which served as the 5th filter (see **SI: Gaussian Mixture Model of alignments,** and **SI Figure 3).** To further verify our findings, we imposed a 6th filter which selects taxa that have been previously identified in the human microbiome by three large studies, namely **H**MP, **U**HGG, or G**E**M datasets, or what we abbreviate as HUE studies (see **SI: Identifying putative habitats of origin for 500+ bacterial genera in the Tabula Sapiens Microbial dataset using the Genomes from Earth's Microbiomes, the Human Microbiome Project, and the Unified Human Gastrointestinal Genome collection** and **SI Figure 4)**. For the remaining taxa that had not appeared in HUE studies (7th filter), we benchmarked (precision of 98% and a recall of 75%) and programmatically employed openAI's Davinci Large Language Model to further select human-associated taxa (see **SI: Benchmarking the Davinci large language model for classification of microbial species based on their habitat, SI Tables 16-18** and **SI Figure 1.e**). Habitat-based filters were placed to select commonly known human-resident or human-associated microbes from the rest.

The output of SIMBA that has been filtered to contain only sequences from the three biomes of interest is referred to as the Tabula Sapiens Microbiome (TSM) dataset F0, to signify that it has not been filtered based on contaminants. The dataset filtered only by the first filter is referred to as TSM F1. The dataset filtered by the first two filters is referred to as TSM F2 and so on, such that TSM F7 is the dataset filtered by all seven filters. The impact of each filter on the total number of microbial hits, species, genera, cell-containing droplets and empty droplets with significant hits is shown in **SI Table 12** and **SI Figure 5**.

153 With the imposition of all filters, we arrive at ~0.4% of the unique hits found in the TSM
154 F0 dataset, ~3% of the species and ~5% of the genera. Like the percentage of unique
155 hits remaining, the percentage of cell-containing and empty droplets is ~0.7% and ~0.4%,
156 respectively. Because the first five filters represent decontamination and quality control
157 filters, we will generally report our findings on TSM F5 and TSM F7, which is the most
158 conservative version of the TSM dataset.

159 **The Tabula Sapiens Microbiome atlas reveals numerous species of microbes**
160 **spanning viruses, fungi and bacteria**

161

162 Binning sequences by donor and tissue type, we summarize their breakdown into high-
163 level taxonomic categories **(Figure 1)**. Numerous species spanning three domains of life
164 are present across 11 donors and 19 tissue types, with bacteria having the highest
165 prevalence of the three domains. We show the fraction of microbial hits in TSM F5 and
166 F7 datasets that have resolved taxonomic identity at each classification level and
167 demonstrate a high percentage, typically >95% (**SI Table 19**). Unlike bacterial
168 sequences, which map largely to commensal species, viral sequences mapped mostly to
169 the Epstein Barr Virus (EBV) - a ubiquitous and persistent human pathogen with very
170 limited transcriptional footprint during its latency compared to its reactivation[37,38]. As we
171 will discuss in more detail, this dichotomy in the transcriptional load of EBV during its
172 latency and reactivation likely gives rise to detectable transcripts in some donors while
173 appearing to be missing from others. Finally, fungal sequences are generally present with
174 lower relative abundances compared to bacteria. This is consistent with previous
175 estimates of fungi at external-facing microbiomes, depicting them significantly
176 outnumbered by bacteria[39–41].

177

178 Bacterial sequences are derived from a range of phyla, most notably Actinobacteria,
179 Firmicutes, and Proteobacteria (**Figure 1**). We find that more than a quarter of all
180 transcripts map bacterial ribosomal RNA (rRNA) (**SI Figure 6**). This relatively large
181 percentage of ribosomal sequences is expected as rRNA is the most abundant form of
182 RNA in bacterial cells, and its abundance is tightly coupled to the bacterial growth rate[42,43],
183 accounting for up to 85% of the RNA pool in rapidly growing bacterial cells in culture[44,45].
184 Furthermore, our finding of bacterial rRNA from diverse bacterial taxa across numerous
185 human tissue types (**SI Figure 7)** is in agreement with a recent study of several tumor
186 types, wherein 16S rRNA was detected using both sequencing and imaging[21].

187

188 The single cell RNA sequencing protocols such as the one used in this study rely on a
189 polyA selection. Hence, at first glance, the discovery of any microbial transcripts is
190 surprising. However, many families of viruses have polyadenylated transcripts[46,47].
191 Additionally, polyadenylation plays a ubiquitous yet understudied role in prokaryotic

transcription[48,49]. Moreover, it is well known that oligo-dT primers often bind with similar efficiencies to A-rich regions as they do to polyadenylated tails, and thus mispriming events inadvertently provide a window into non-polyadenylated transcripts[50,51].

Mapping the possible microbial flow routes from external-facing microbiomes and natural environments to internal tissues and tumors

To explore the human tissue microbiome at a more granular level, we created a Sankey plot (**Figure 2.a**), wherein each one of the microbial hits is represented by a line, the path of which can be traced to obtain the tissue type of origin, taxonomic categorization, as well as additional information gathered from external databases. We provide this as an interactive plot (**SI File 1**) along with the table underlying these flow paths (**SI Table 20**). The HMP dataset was used to identify species that had previously been observed at external-facing microbiomes from the gastrointestinal tract, oral cavity, ear, nose, airways, urogenital tract, and the skin. Approximately 50% of bacterial genera that make up tissue microbiomes appear in external-facing microbiomes (**SI Figure 8**).

With the assumption that microbial flow occurs from external to internal sites, we depict possible flow routes for numerous bacterial genera and show that various external and internal sites are connected through their shared taxa (**Figure 2.a**, **SI Figure 9**). Surprisingly, not all species found at internal sites originate from the gastrointestinal tract. Other external-facing microbiomes appear to contribute many species to internal organs and tissues. To illustrate a few microbial flow paths, we detected sequences from *Treponema denticola,* an oral bacterium commonly associated with periodontal disease, in the heart. This observation is in line with studies that have linked *Treponema denticola* to atherosclerosis through its invasion of aortic tissue[52–54]. Sequences mapping to *Aggregatibacter aphrophilus*, another oral bacterium whose infection can lead to endocarditis, was also detected in the heart (**SI Figure 9**). While various members of the oral microbiome have been associated with cardiovascular diseases[55], we find that the heart is certainly not the only destination for sequences from species normally found in the oral cavity. For example, we found sequences mapping to *Porphyromonas gingivalis* not only in the salivary gland tissue as might be expected, but also in tissues from the thymus, liver, vasculature, fat, bone marrow and others. Sequences mapping to inhabitants of other external-facing microbiomes were similarly found in various tissues (**Figure 2.a**, **SI Figure 9**). It remains to be discovered to what extent species from external-facing microbiomes can colonize these distant sites.

In addition to the HMP dataset, we compared the number of shared genera between TSM datasets and UHGG, which represents a much larger number of gut metagenomic samples than found in HMP (**Figure 2.a, SI Figure 10**) and includes samples collected from various countries, thus providing a global perspective on the shared genera. We

further explored the bacterial taxa shared between TSM and tumors (Nejman *et al.*[21]) of the pancreas, breast, colon, lung, skin, ovaries, bone, and the brain (**Figure 2.a, SI Figures 11-14**). Nearly half of TSM F7 bacterial genera have previously appeared in human tumors (**SI Figure 11**). We created an abundance heatmap of these genera across TSM tissues (**SI Figure 11**). Sequences from species that were previously identified as highly enriched in tumors including *Paracoccus marcusii* and *Roseomonas mucosa* are also present across various TSM F5 tissues, primarily from lymphatic organs (**SI Figure 12**). We do not identify any of the tumor-enriched species in the TSM F7 dataset. The relatively large overlap between TSM and tumor microbiomes suggests that tumor microbiomes may be sourced from adjacent tumor-free tissue microbiomes, even possibly from tissues at distant sites from the tumor (**SI Figure 12-14**). We provide a list of bacterial genera found in tumor microbiomes that are missing from the TSM F5 or F7 datasets (**SI Table 21**). Some of these genera may perhaps prove to be tumor-microbiome specific, however future studies applying the same experimental and bioinformatic protocols to tumor-free and tumor-derived tissues are needed.

We mapped the possible microbial flow routes from natural environments and external-facing microbiomes to tissues and tumors by focusing on sequences from species found across TSM, GEM, HMP, UHGG, and the Nejman *et al.* datasets (**SI File 2, SI Table 22**). Many interesting flow routes appear to exist with varying degrees of complexity. As an example of a flow route, sequences from members of the *Aggregatibacter* genus appear to originate from the oral microbiome and the gastrointestinal tract (HMP, GEM, UHGG). They are detected in salivary gland tissue as well as thymus, blood, liver, heart, lymph nodes and other tissues (TSM F7). They are also found in breast tumors (Nejman *et al.*). We provide these flow routes both as an interactive plot (**SI File 2**) and as a table (**SI Table 22)**.

Additionally, we used the PATRIC database[31] to obtain further information about the pathogenicity potential of bacterial species. We found the following potential bacterial pathogens in the TSM F7 dataset: *Porphyromonas gingivalis, Campylobacter showae, Aggregatibacter actinomycetemcomitans, Capnocytophaga gingivalis, Campylobacter curvus,* and *Treponema denticola*. From this list, the HMP dataset contains all but one pathogen, namely *Campylobacter curvus*. *Campylobacter curvus* and *Porphyromonas gingivalis* appear in human gut samples from the UHGG dataset. Finally, *Capnocytophaga gingivalis* appears in the Nejman et al. dataset.

To explore the inter-and-intra donor tissue microbiomes at finer taxonomic resolution, we computed the shared species within and across individuals. Whether considering the tissues of one donor or the collective tissue microbiomes of many donors, tissue microbiomes appear to have many overlapping species **(Figure 2.b, SI Figure 15)**. However, when accounting for all species, species unique to each sample outnumbered

those that are shared (**Figure 2.c, SI Figures 16-17**). Furthermore, we compared species-level bacterial microbiomes in a pairwise fashion using the Spearman correlation for both TSM F7 and F5 datasets (**SI Figures 18-19**), revealing tissue microbiomes across and within each individual to be uncorrelated at the species level, but increasingly more similar at higher levels of classification. For a more detailed discussion, see **SI: Exploring the inter-and-intra tissue microbiomes.**

Increasing the resolution of tissue microbiomes to delineate cell type microbiomes

Many of the microbial sequences can be traced back to cells that have been annotated by the Tabula Sapiens Consortium. Merging cell type annotation data from Tabula Sapiens objects with cellular barcodes provides an unprecedented view of each tissue's microbiome at the level of cell types and even individual cells. We wondered how different cell types compare in terms of their microbial load. Thus, we quantified single-cell microbial load as $\log_2(h_c/g_c)$, where h_c represents the number of microbial sequences detected in cell *c* and is normalized by the number of host genes detected in that cell, g_c, to account for cell to cell variation in sequencing coverage. It is important to note that this data does not indicate whether these microbes or their sequences have been internalized by these cells; they could be binding to the external cell membrane.

Ranked distributions of single-cell microbial loads (**Figure 3.a**), reveal that cell types with the largest microbial load include enterocytes, T cells, and plasma B, among other cell types, especially those from the immune compartment. The over-representation of immune cell types is expected as these cells, with the ability to survey tissues, are the first to encounter microbial organisms. Enterocytes are also the first line of barrier against the trillions of microbes housed in the human intestinal tract. At first glance, the finding of microbial sequences in pancreatic acinar cells and in the pancreas more generally, may be the most surprising observation, however the pancreas is an organ with a physical connection to the small intestine. This connection has been previously shown to enable the passage of intestinal fungi to the pancreas where they can promote pancreatic adenocarcinoma[24]. Additionally, pancreatic adenocarcinoma tumors have been shown to harbor microbiomes that are predictive of long-term survival[22].

Network of human cell types in association with microbes reveals cell types with greatest microbial diversity

To explore the diversity of cellular microbiomes, we built a bipartite network of cell types stratified by tissue of origin (source nodes) and their associated microbial species (target

nodes) for both the TSM F5 and TSM F7 datasets (**Figure 3.b, SI Files 3**). Cell types in each tissue are weighted by the number of unique microbial species, normalized by the number of annotated cells sequenced. Hence, in this network of host-microbe associations, hubs represent cell types with the greatest microbial diversity. Examples of these hubs include Thymus and bone marrow CD4+ T cells, lymph node B cells and CD8+ T cells. As with microbial load measurements, immune cell types are over-represented in their diversity of microbial associations. Cellular microbiome network depictions such as this open a window into host cell and microbe interactions in their native context which would not be captured in bulk tissue sequencing experiments. An example of an important association is between EBV and splenic plasma cells. We report statistics on droplets with hits, and identify outlier cells based on number of hits per cell (see **SI: Single-droplet statistics, outlier cells and outlier cell types,** and **SI Tables 23-26**). Interestingly, the most prevalent species found in outlier cells is EBV, and most outlier cells are from immune cell types.

Detecting the transcriptional footprints of a persistent viral pathogen and an ancient viral relic in human cells

EBV was the first oncovirus to be discovered and has since been shown to cause Burkitt's, Hodgkin's, NK and T cell lymphomas as well as nasopharyngeal and gastric carcinomas, thus accounting for ~200,000 (or 2% of) cancer deaths annually worldwide[56]. In absence of an approved EBV vaccine, currently most primary infections occur in children and adolescents, such that by adulthood a significant fraction of the population is latently infected[57–59]. Additionally, a recent longitudinal study of 10 million young adults has shown a ~30 fold increase in the risk of multiple sclerosis after EBV infection, placing EBV as one of the leading potential causes of multiple sclerosis[60].

During the latent phase of its lifecycle, EBV suppresses the transcription of most of its genome[38] and replicates infrequently and in synchrony with the host cell while utilizing the host polymerase[61]. In our cohort, we detected EBV sequences in five seropositive donors, and across various tissues including the lung and the bladder. The majority of hits originate from donors 1 and 2 (TSP1 and TSP2) and from lymphoid organs such as the spleen, where many of the susceptible host cell types reside (**Figure 4.a, SI File 4**). Consistent with the known aspects of EBV tropism[62], we found that the majority of sequences originate from cell types belonging to immune and epithelial compartments.

Across distributions of EBV single-cell load in different cell types, plasma cells outrank other cell types (**Figure 4.b**). Applying BLASTx to identify protein coding sequences, we primarily found those expressed during the lytic phase (**Figure 4.c**): membrane glycoprotein (BILF1), DNA synthesis and genome packaging protein (BALF3)[63], and the

viral DNA polymerase (BALF5), which is used to replicate the EBV genome exclusively during the lytic phase[61]. Notably, we observe BZLF1 expression, an important transcriptional switch that initiates the expression of various lytic genes[64]. Although EBV sequences are present across a variety of cell types, only plasma cells, B cells and NK cells are positive for lytic transcripts, consistent with the fact that these cell types are known susceptible host cell types for EBV. Considering that the latent phase of EBV life cycle is characterized by the expression of non-coding RNAs, many of which suppress lytic genes[56], absence of coding lytic transcripts suggests that other cell types are experiencing latent infections. Alternatively, they may have uptaken transcripts passively by virtue of physical proximity to sites of lytic infections, or actively through their involvement in the clearance of lytically infected cells.

In addition to EBV, we detect the presence of human endogenous retroviruses (HERVs). Introduced numerous times during the evolutionary history of primates, HERV genomes, which are mostly defunct, occupy 8% of the human genome[65]. The HERV K (HML-2) family, representing the latest insertions into the human genome, is the only family of HERVs that is transcriptionally active. Differential expression of HERV K genes has been detected across several cancers and is thought to contribute to tumor progression[66,67]. Additionally, HERV K expression and even virus-like particles have been detected during human blastocyst formation[68]. Although this virus was tagged as a putative contaminant by our ML decontamination model, we believe this may represent one instance of the model's false positives. This is because we did not detect HERV K in the ~200 negative controls obtained for the TSM dataset. We also identified it again separately through another set of experiments described in the next section.

Contrary to the claim that HERV K expression is silenced in all but a few special contexts[69], we identified HERV K (HML-2) transcripts across five donors, spanning a diverse range of tissues (e.g. skin, fat, spleen and the salivary glands) and cell types (**SI Table 27**). These sequences map to the three canonical retroviral genes in the HERV K genome, namely pol, gag and env (**SI Figure 20**). HERV K expression in human donors beyond tissues and cell types previously investigated, opens the possibility that this enigmatic ancient relic may be more widely active and physiologically relevant than previously appreciated.

Tissue microbiomes through the lenses of DNA sequencing, fluorescence, and electron microscopy

To further examine our findings through other techniques beyond single-cell transcriptomics, we developed an assay that extracts virus-like and bacterial-like particles

(VLPs and BLPs) from human tissue (see **Methods: The Extracted Human Tissue Microbiome dataset)**. We refer to the resulting dataset as the Extracted Human Tissue Microbiome (EHTM). We used DNA sequencing, fluorescence and electron microscopy of VLPs and BLPs extracted from 4 tissue types (pancreas, blood, lymph node, and lung) and 8 donors (**Figure 5.a**). In this assay, we gently dissociate tissues, eliminate cell- or capsid-free nucleic acids, and subsequently size select for VLPs and BLPs. We used negative controls for all experimental steps to eliminate contaminants from bulk DNA sequencing of these extracted particles. Using nucleic acid staining followed by fluorescence microscopy of these particles from the lung and lymph nodes (**SI Figure 21**), we observed high concentrations of VLPs and BLPs (~10^7 BLPs and ~10^8 VLPs per cm^3 of tissue). Electron microscopy of VLPs further showed familiar virus morphologies such as a hexagonal capsid (similar to many bacteriophages) and rod-shaped capsids (reminiscent of the tobacco mosaic virus or the rudivirus) in the pancreas (**Figure 5.b**). It also revealed several novel morphologies, for example one with interior nodules and fibrous protrusions residing in a lymph node. Moreover, DNA sequencing of these extracted particles further captured numerous sequences mapping to viruses, bacteria, and even some fungi as some have similar sizes to bacteria (**Figure 5.c**). These results support and are consistent with the single cell transcriptomic data, thus providing independent evidence for several of our conclusions.

Interestingly, EBV and HERV K were both identified in the EHTM cohort. EBV was found in all 8 donors, which is a higher prevalence than obtained via RNA sequencing. Considering that single-cell RNA sequencing preferentially captures transcriptionally active organisms, one would expect to see higher EBV donor positivity rate using DNA sequencing of VLPs. The combination of these two methodologies could perhaps be used to decipher active versus inactive organisms to further make a distinction between residents and passengers of the human tissue microbiome.

Moreover, we identified the genera that overlap between all six datasets: TSM, HMP, Nejman *et al.*, UHGG, GEM, and the EHTM datasets (**Figure 5.d-e**). For example, we found sequences mapping to *Rothia mucilaginosa* in the pancreas and several other organs using single-cell transcriptomics (TSM dataset). This species, a member of the airway microbiome (HMP dataset), appears in pancreatic, lung and breast tumors (Nejman *et al.*). Consistent with its traces in these three datasets, we identify this species through DNA sequencing of the extracted BLPs in the pancreas, lung, blood, and lymph nodes. Given these additional experiments, it is perhaps fair to assume that sequences found in single-cell transcriptomic data are not all cell-or capsid-free. Some perhaps originate from intact organisms that escape cellular barriers to reach internal tissues and tumors.

Discussion

The transcriptional footprints of microbial life in human organs and cells raise several questions. For example, how could microbes escape cellular barriers established by epithelial and endothelial cells? Are there any long-term residents of human tissues in a commensal relationship with our own cells? And can these microbial signatures be used as diagnostic markers for organ health? One likely route of microbial migration is from the gut to other organs, as leaky gut epithelia together with the gut-liver axis have been proposed as a route of dissemination for various microbial metabolites from the gut into the systemic circulation[70,71]. The same route is likely to harbor microbial genomes, transcripts, and perhaps whole cells and capsids. In fact, viral migration across epithelial layers has been demonstrated *in vitro*[72]. However, as we have shown there are likely other possible flow paths from other external-facing microbiomes such as the oral cavity and the urogenital tract to various internal organs.

Overall, there is growing evidence for the existence of microbial interactions with human cells at sites in the body that are typically inaccessible to sampling. While microbial sequences have already been shown as diagnostic markers for cancer detection, our understanding of their associations with human cells is largely lacking. It is possible that causal associations exist, and that the list of oncogenic microbes is much larger than previously appreciated. Our finding of significant overlaps between tumor-free tissue microbiomes and tumor microbiomes suggests that tumor microbiomes are at least partially sourced from normal tissue microbiomes. As such, mechanism-level understanding of microbe-host interactions in human tissues could further shed light on the highly variable nature of individual responses to cancer immunotherapies[73,74] and provide novel and targeted avenues for microbiome-based immune modulation, as well as lay foundational insights into the interplay between microbes, tumor cells and the host immune cells. Moreover, given that infectious agents account for ~15% of all cancers[75], and that many pathogens can manipulate the host cell cycle[76,77] and predispose host cells to cancer[78], it is highly plausible that we have only scratched the surface of causal links between microbes and various pathologies.

With the availability of high-throughput single cell sequencing technologies today, we stand at a unique time in the history of microbiology, where the study of microbe-host interactions offers an exciting new frontier. These interactions can now be studied at the level of individual cells[79–81] not just *in vitro,* but as we have shown, in the very real context of organs - in the presence of the immune system, neighboring cells, nutrient fluxes and many other important factors that shape microbial life cycles.

Conclusion

In this study we provide the first atlas of the human tissue microbiome with cell type resolution, for which we have developed new experimental and computational pipelines such as a machine learning-based decontamination model. We discovered sequences mapping to numerous species from three domains of life. We map out the possible flow routes of microbes from external-facing microbiomes to internal tissues and tumors, and show that tumor microbiomes share many common taxa with normal tissue microbiomes. We further constructed a network of associations between human cell types and microbes, shedding light on the types of organisms that cells from different tissues encounter either by way of immune clearance or physical proximity to microbial niches and sites of infections. This type of analysis can reveal the interactions between various cell types and microbial organisms. In cases of intra-cellular infectious events such as EBV, host and pathogen transcriptomic landscapes may reveal novel pathways that underlie cellular susceptibility and resistance, which would have great clinical application.

Materials and Methods

The Tabula Sapiens dataset

The Tabula Sapiens raw fastqs containing single-cell RNA sequencing data from Smart-seq2 and 10X droplet-based experimental pipelines were acquired from the Tabula Sapiens consortium[28] (https://github.com/czbiohub/tabula-sapiens). This included raw fastqs for 12 donors 1,2,4,6,7,8,9,10,11,12,14, and 16 as well as objects which contained cell type annotations for ~0.5 million cells (donor 16 cell type annotations were not included). All analysis was performed on the 10X data, which represents the vast majority of this dataset. Donor 4 tissues (mammary, myometrium, uterus) were eliminated in the TSM F7 version of the dataset due to not meeting the criteria imposed. Additionally, because we could not acquire negative control samples for tongue tissue, we do not report on this tissue. Thus we have a total of 11 donors and 19 tissues in the TSM F7 dataset.

The Extracted Human Tissue Microbiome dataset

Tissue Digestion and DNA extraction. Tissues were acquired from Donor Network West (delivered on ice) and cut into 1 cm blocks using UV and ethanol sterilized scalpels and petri dishes. Tissues were incubated for 90 minutes with collagenase IV (1 mg/mL, Worthington) at 37°C and further disrupted by pipetting. Disrupted tissue samples were then incubated for 30 minutes at 37°C with 19U/mL DNase I and 1mg/mL RNase A

(ThermoFisher) - added to eliminate as much of the cell- or capsid-free DNA and RNA that is released during tissue digestion. The RNAase and DNAase enzymes were deactivated using RNAsecure at 1X and EDTA at 5mM for 10 minutes at 65℃. Each sample was then filtered through a sterile 40μm cell strainer, to eliminate the cellular debris. The filtrate was passed through a 5μm pore size syringe filter to enrich particles in the size range of most microbes and to eliminate host cells. To separate out as many virus-like particles from this mixture of filtrate, we imposed another filter, this time using a 0.8μm pore size syringe filter. The filter was inverted and objects larger than 0.8μm were collected. Although this was a protocol developed in-house, we were able to get key insight from several sources: Qiagen TissueLyser Handbook, Worthington Tissue Dissociation Guide and viral metagenomic studies[82]. DNA extraction was then performed using QIAmp DNA mini kit (Qiagen) according to kit instructions. Moreover, we used multiple negative controls for each step of the experimental workflow, including tissue digestion, DNA extraction, and library preparation.

Sequencing and data analysis. We used SIMBA on this dataset, excluding steps used for UMI extraction. We used the negative control samples to create a blacklist of contaminants, which were subsequently removed. Despite significant methodological differences between the EHTM dataset, and the TSM single-cell transcriptomic dataset, we found members from the Actinomyces, Neisseria, Rothia, Corynebacterium, Nesterenkonia, Streptococcus, Veillonella genera shared between the two datasets. However, it is important to note that the level of overlap between these two datasets and any others depends on parameters such as sampling depth and method of detection.

TEM. We plasma treated EM grids (300 mesh Carbon/Formvar coated Copper grids) using Leica EM ACE600 to allow each sample to bind to the grid. We applied 5μL of 1:1000 diluted sample onto each EM grid and allowed the sample to bind for 3 minutes. The grid was then exposed to 1% uranyl acetate for one minute, and subsequently dried using a filter paper. Samples were imaged using JEOL JEM-1400.

Fluorescence imaging. Following tissue digestion and microbial extraction, filterates were stained with SYBR™ Gold Nucleic Acid Gel Stain (ThermoFisher) at 10X for 10 minutes at room temperature and imaged using Leica CTR6000. Bright dots were counted manually across different sections across a hemocytometer grid and average counts were projected to estimate VLP and BLP concentrations per cubic centimeter of tissue.

Acknowledgements

We thank Rob Phillips for insightful comments on the manuscript. We also thank Leila Sidow, Robert Jones, Roja Kolluru, Ed Marti, Elizabeth Jerrison, Mark Kowarsky, Alina Isakova, Stephanie Tzouanas Schmidt, Yuan Xue, Mira Moufarrej, Michael Swift, Ivana Cvijovic and all the other members of the Quake lab, along with the Tabula Sapiens and the Boundaries of Life consortia for their help and suggestions towards experimental and computational pipelines. Additionally, we thank the following Tabula Sapiens consortium members for their help towards tissue digestion controls: Mallory Ann Laboulange, William Kong, Siva Vijayakumar, Hua Dong, Rebeca Arroyo, Hayley Raquer, Michael Swift, Zhen Qi, Will Goodyer, Gabriel Loeb, Simon Bucher, Helen Zue Zhang, Soochi Kim, Yan Hang, Juan Irwin, Emily Trimm and Irene Fan. We are grateful to Donor Network West personnel including Ahmad Salehi and Ravi Ponnusamy, as well as the Cell Sciences Imaging Facility at Stanford University. We are especially indebted to donors and their families for their incredible contribution to science. This work was supported by the Chan Zuckerberg Biohub, the Gordon and Betty Moore Foundation and the John Templeton Foundation.

Funding

This work was supported by the Chan Zuckerberg Biohub, the Gordon and Betty Moore Foundation and the John Templeton Foundation.

Author contributions

Conceptualization: GM, SRQ
Methodology: GM, SC, SRQ
Investigation: GM, SRQ
Data Curation: GM
Formal Analysis: GM
Visualization: GM
Software: GM
Funding acquisition: GM, Tabula Sapiens Consortium, SRQ
Resources: GM, Tabula Sapiens Consortium, SRQ
Project administration: GM, Tabula Sapiens Consortium, SRQ
Writing – original draft: GM
Writing – review & editing: GM, SC, SRQ

Competing interests

Authors declare that they have no competing interests.

Data and materials availability

All data and code is available through our GitHub repository: https://github.com/gitamahm/human_tissue_microbiome_atlas. This repository includes SIMBA, which is written in Snakemake[32], Post-SIMBA data analysis and visualization organized into separate Jupyter Notebooks (written in python v3.6.10). The Jupyter notebooks are listed below.

- p01_databaseCreationSC_microbeDB_fungalDB.ipynb
- p02_creating_truth_datasets_for_testing_simba.ipynb
- p03_testing_truth_datasets.ipynb
- p04_experimental_negative_controls.ipynb
- p05_post_SIMBA_processing_alldonors_and_EHTM_gh.ipynb
- p06_cell_ranger_counts_gh.ipynb
- p07_machine_learning_modeling_contamination_and_other_filters.ipynb
- p08_habitat_assignment_using_GEM_HMP_UHGG.ipynb
- p09_davinci_language_model_habitat_of_origin_gh.ipynb
- p10_impact_of_filters.ipynb
- p11_single_cell_microbiome_stats.ipynb
- p12_tabula_sapiens_multibiome_analysis.ipynb
- p13_ts_intersection_with_external_datasets.ipynb

Figure

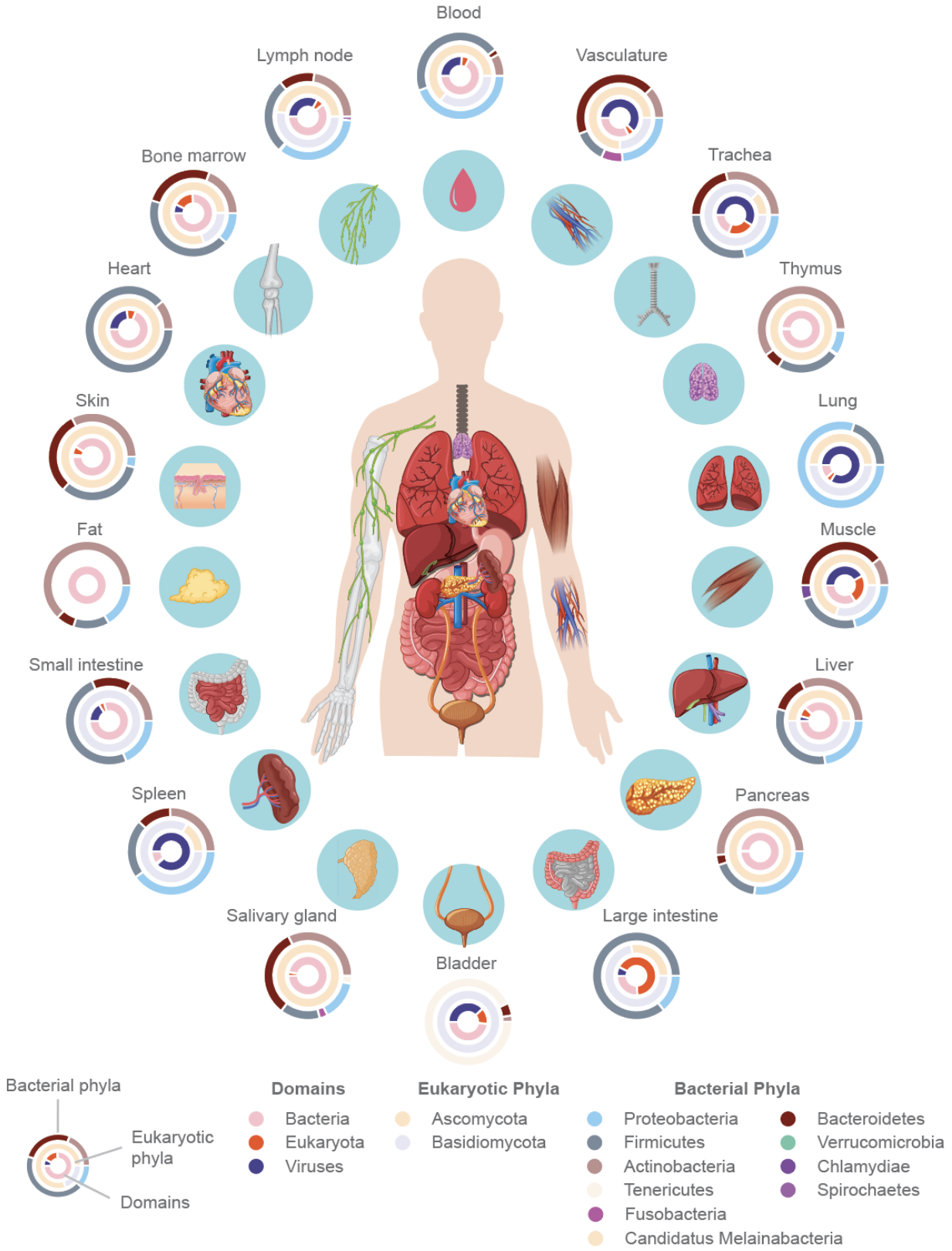

Figure 1. Tabula Sapiens Microbiome (TSM) atlas derived from the Tabula Sapiens single-cell transcriptomic dataset consisting of 19 tissue types from 11 donors (identified

597 by TSP#), 100+ cell types and 400,000+ annotated cells. Tissue microbiomes are
598 stratified based on taxonomy: domains (inner ring) followed by eukaryotic phyla, and
599 bacterial phyla, respectively. Sequences are grouped based on donor (one donor is
600 shown per tissue). Most tissues shown are from TSP2, except for Thymus, Liver, Salivary
601 gland which are from TSP14, Pancreas from TSP9, Heart from TSP12, and Skin and Fat
602 from TSP10. Tissues shown have at least 10 hits and are from the TSM F7 dataset.
603

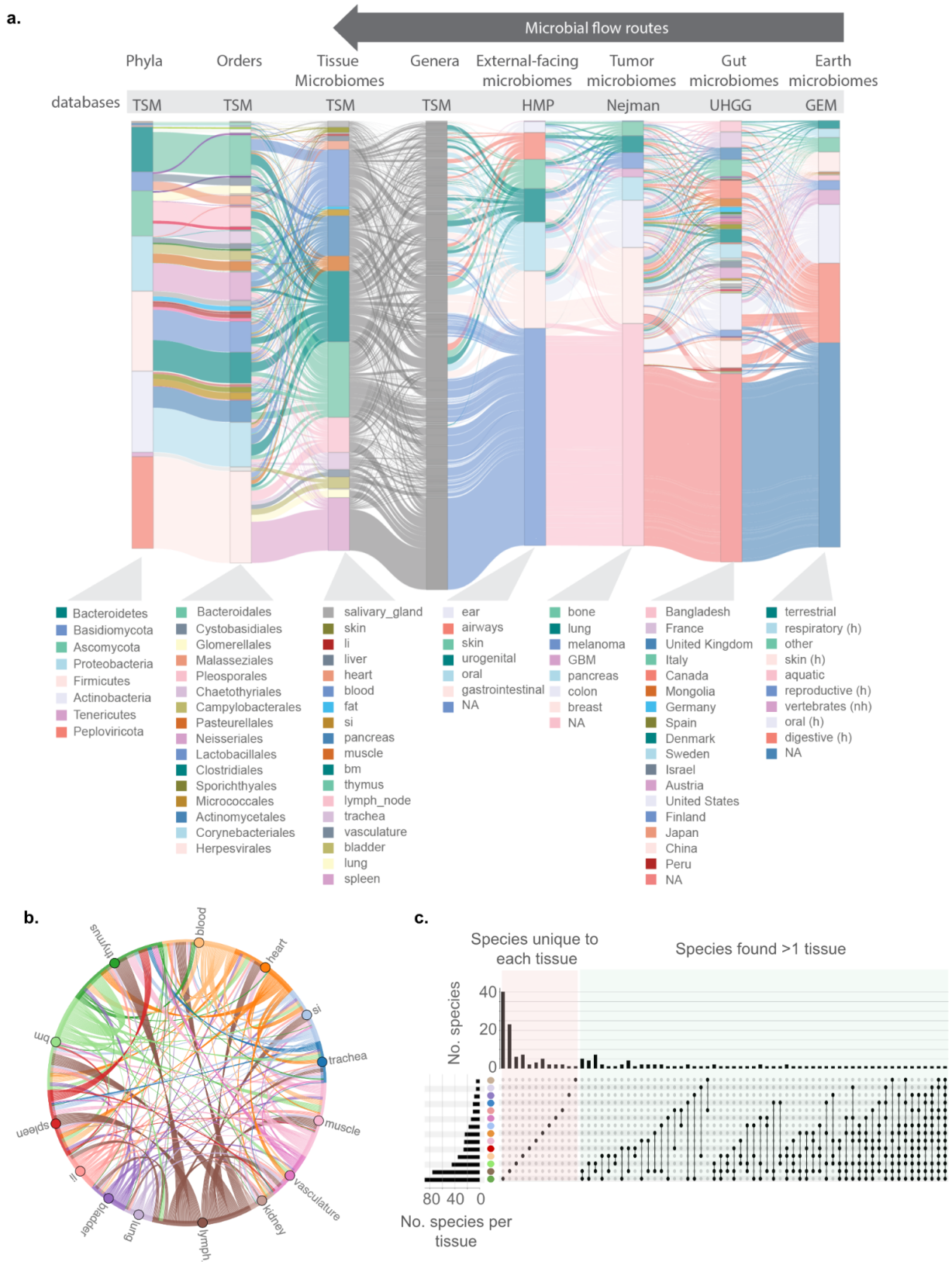
a.
Microbial flow routes
Phyla
Orders
Tissue Microbiomes
Genera
External-facing microbiomes
Tumor microbiomes
Gut microbiomes
Earth microbiomes
databases
TSM
TSM
TSM
TSM
HMP
Nejman
UHGG
GEM
Bacteroidetes
Basidiomycota
Ascomycota
Proteobacteria
Firmicutes
Actinobacteria
Tenericutes
Peploviricota
Bacteroidales
Cystobasidiales
Glomerellales
Malasseziales
Pleosporales
Chaetothyriales
Campylobacterales
Pasteurellales
Neisseriales
Lactobacillales
Clostridiales
Sporichthyales
Micrococcales
Actinomycetales
Corynebacteriales
Herpesvirales
salivary_gland
skin
li
liver
heart
blood
fat
si
pancreas
muscle
bm
thymus
lymph_node
trachea
vasculature
bladder
lung
spleen
ear
airways
skin
urogenital
oral
gastrointestinal
NA
bone
lung
melanoma
GBM
pancreas
colon
breast
NA
Bangladesh
France
United Kingdom
Italy
Canada
Mongolia
Germany
Spain
Denmark
Sweden
Israel
Austria
United States
Finland
Japan
China
Peru
NA
terrestrial
respiratory (h)
other
skin (h)
aquatic
reproductive (h)
vertebrates (nh)
oral (h)
digestive (h)
NA
b.
blood
heart
si
trachea
muscle
vasculature
kidney
lymph
lung
bladder
li
spleen
bm
thymus
c.
Species unique to each tissue
Species found >1 tissue
No. species
40
20
0
80 40 0
No. species per tissue

604

605 **Figure 2.** Microbial flow within the body from external and internal environments (TSM
606 F7 dataset). a) Sankey plot revealing the taxonomic classification and tissue of origin for
607 each sequence (each line in the plot represents an individual sequence) along with
608 additional data from the Human Microbiome Project (HMP) database, tumor microbiome
609 dataset by Nejman *et al.*, the Unified Human Gastrointestinal Genome (UHGG) collection
610 and the Genomes from Earth's Microbiomes (GEM). Sequences belonging to species that
611 are not found in these additional databases, including all viral and fungal species, are
612 labeled as "NA". Under the GEM column, "h" denotes human and "nh" denotes non-
613 human. Only some of the largest groups in each column are denoted in the legend. The
614 rest can be found as part of the interactive plots provided in the **SI File 1**. b) Circos plot
615 of shared species within TSP2 (donor 2). Each link represents a unique species. Species
616 that are not shared between tissues are not shown. c) UpSet plot for TSP2 demonstrating
617 the number of shared species between tissues, as well as the number of species unique
618 to each tissue. Unique sets of species are shown as filled circles. The intersection of two
619 or more sets are shown via connected filled circles. Bars denote the size of each set or
620 the intersection of sets.Tissues are color-coded according to panel b. bm: bone marrow,
621 li: large intestine, si: small intestine.

622

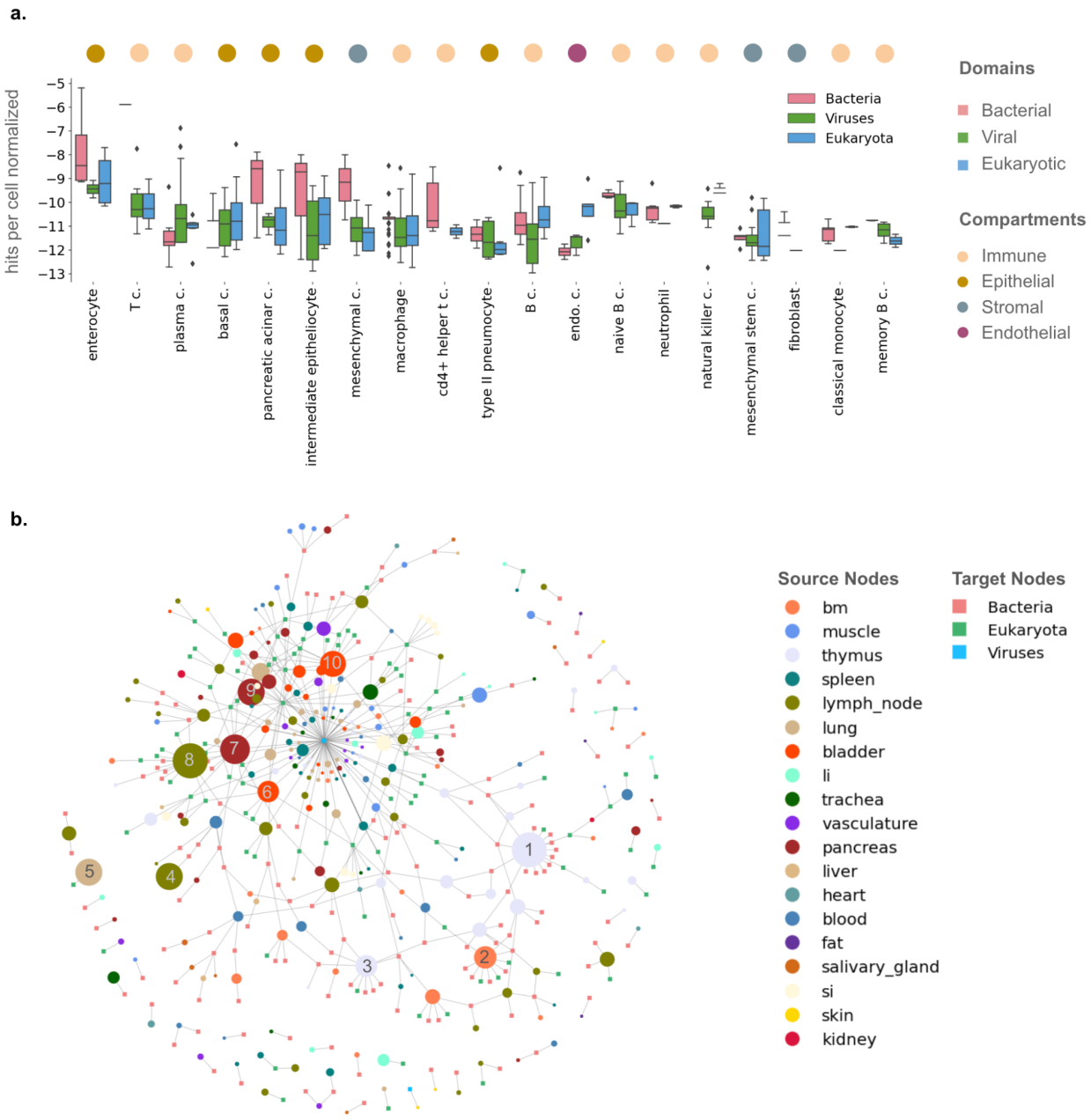

Figure 3. Cellular microbiomes across all donors. a) Distributions of hits per cell against three domains of life, grouped by cell type from TSM F5. Cell types are ordered based on the maximum value found in any of the three distributions. Y-axis corresponds to $\log_2(h_c/g_c)$, where h_c is the number of hits per cell, normalized by the number of g_c, number of detected genes per cell. Only cells with detected hits are included in the analysis and only cell types with at least 10 cells. b) Network of human cell types (grouped by tissue of origin) in association with microbes. Cell types are source nodes (circular), and

632 microbial species are the target nodes (square). Source nodes are weighted by $S_i/\log_2 C_i$,
633 where S_i represents the number of unique species associated with source node *i*, and is
634 normalized by the total number of cells, C, sequenced for source node *i*. The
635 normalization ensures that cell types with greater representation in the dataset do not
636 artificially appear to have more diverse microbial associations. Moreover, edges in this
637 network are weighted by $N_{j,i}$, the counts of sequences mapping to microbial species *j*
638 associated with source node *i.* For visual clarity, only larger source nodes are labeled: 1)
639 Thymus CD4+ T cell, 2) bone marrow CD4+ T cell, 3) thymus fibroblast, 4) lymph node
640 effector memory T cell, 5) lung regulatory T cell, 6) bladder intermediate epitheliocyte, 7)
641 pancreatic acinar cell, 8) lymph node B cell, 9) pancreas fast muscle cell, 10) bladder
642 macrophage. For all other nodes, please see the accompanying interactive plot (SI File
643 3). bm: bone marrow, li: large intestine, si: small intestine.

644
645
646

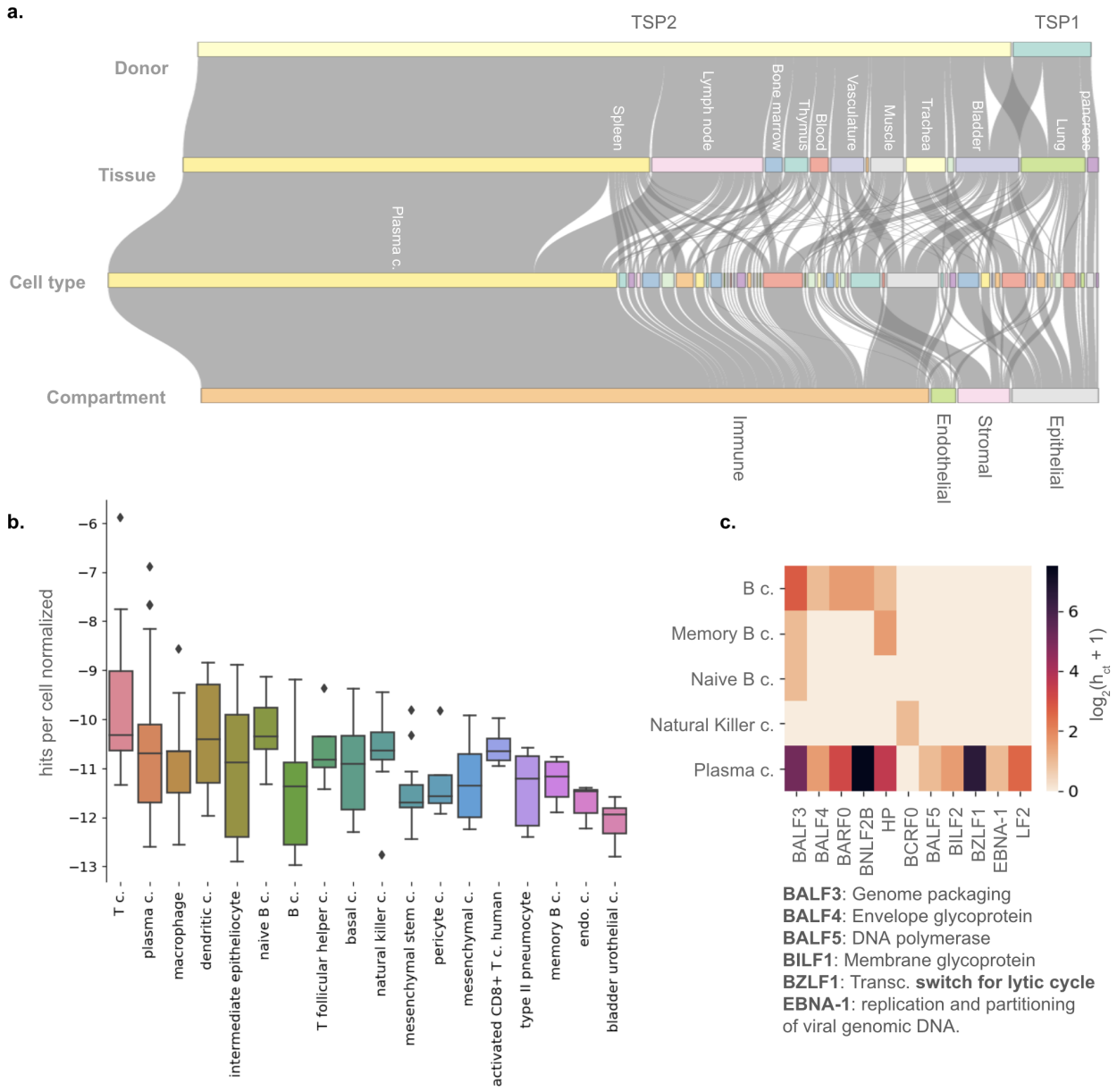

Figure 4. Detection of EBV across tissues and cell types (TSM F7). a) Sankey plot of EBV sequences, demonstrating their donor, tissue, cell type, and compartment of origin. For visual clarity, only hits from annotated cells are included (TSP1 and TSP2 hits remain) and only large groups have been labeled for tissue and cell type rows. Please see the accompanying interactive plot (SI File 4). b) EBV hit per cell distributions grouped by cell type from any tissue that is EBV hit positive. Y axis denotes $\log_2(h_c/g_c)$, where h_c is the number of hits per cell, normalized by the number of g_c, number of detected genes per cell. Only cell types with at least 5 cells are shown. c) heatmap of protein-coding sequences identified in TSP2 mapping to EBV, grouped by cell type. The scale bar

658 denotes $\log_2(h_{ct} + 1)$, where h_{ct} represents the number of hits per cell type. The functional
659 role of some of the EBV protein coding sequences are denoted. Note, “HP” corresponds
660 to “hypothetical protein”.

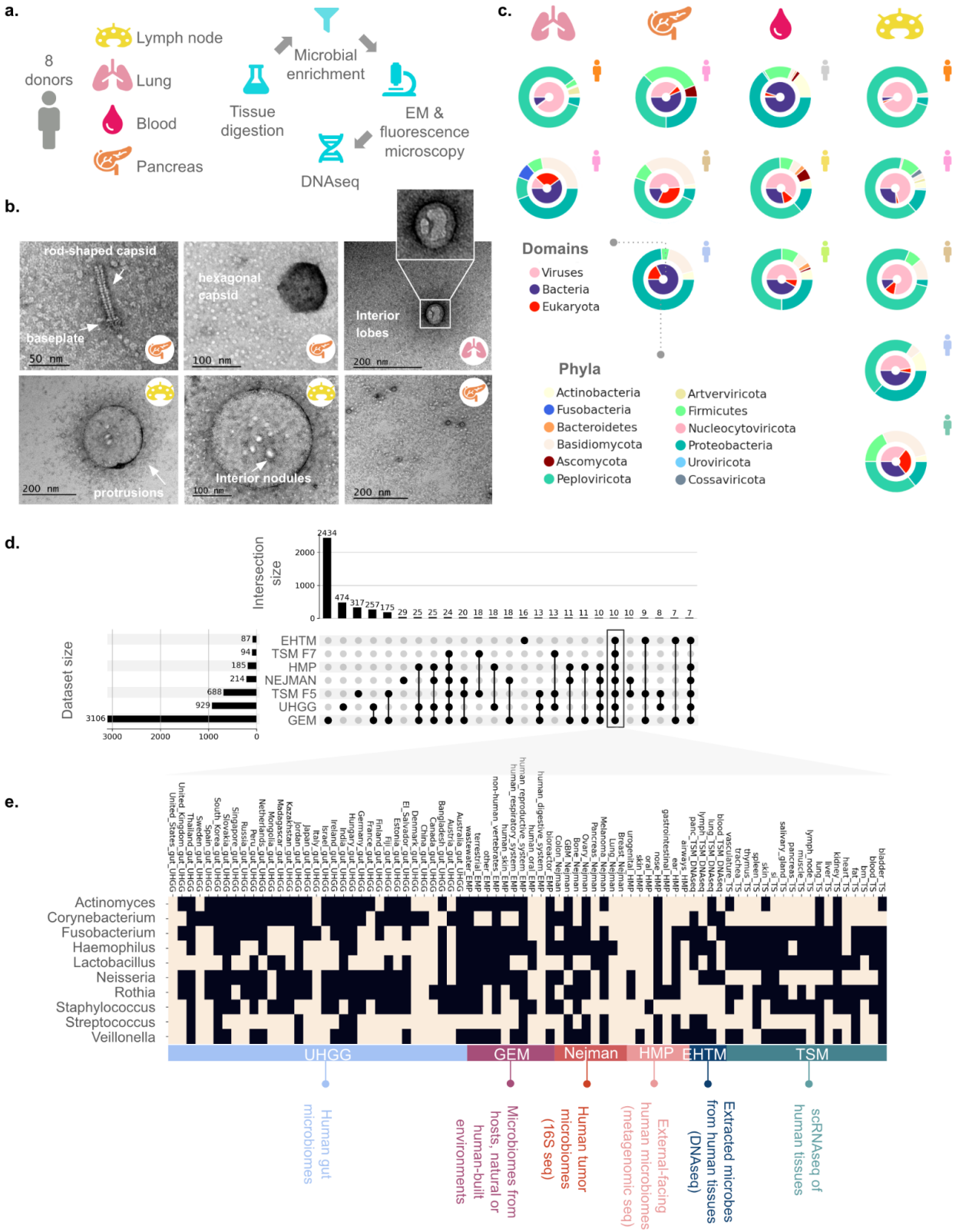
a.
8 donors
Lymph node
Lung
Blood
Pancreas
Tissue digestion
Microbial enrichment
EM & fluorescence microscopy
DNAseq
b.
rod-shaped capsid
baseplate
50 nm
hexagonal capsid
100 nm
Interior lobes
200 nm
200 nm
protrusions
Interior nodules
100 nm
200 nm
c.
Domains
Viruses
Bacteria
Eukaryota
Phyla
Actinobacteria
Fusobacteria
Bacteroidetes
Basidiomycota
Ascomycota
Peploviricota
Artverviricota
Firmicutes
Nucleocytoviricota
Proteobacteria
Uroviricota
Cossaviricota
d.
Intersection size
Dataset size
EHTM
TSM F7
HMP
NEJMAN
TSM F5
UHGG
GEM
e.
Actinomyces
Corynebacterium
Fusobacterium
Haemophilus
Lactobacillus
Neisseria
Rothia
Staphylococcus
Streptococcus
Veillonella
UHGG
GEM
Nejman
HMP
EHTM
TSM
Human gut microbiomes
Microbiomes from hosts, natural or human-built environments
Human tumor microbiomes (16S seq)
External-facing human microbiomes (metagenomic seq)
Extracted microbes from human tissues (DNAseq)
scRNAseq of human tissues

Figure 5. Tissue microbiomes from 8 donors using DNA sequencing, fluorescence and EM imaging from the Extracted Human Tissue Microbiome dataset along with a comparison to several other datasets. **a)** study design and experimental workflow. **b)** EM images of viral fractions retrieved from the pancreas, lung and lymph nodes showing both known and novel virus-like morphologies. **c)** hits per tissue and donor stratified based on taxonomy: domains (inner ring) and phyla. **d**) Exploring the intersection of bacterial genera across various datasets using an UpSet plot: Tabula Sapiens Microbiome (TSM) F5 and F7, Extracted Human Tissue Microbiome (EHTM), Human Microbiome Project (HMP), Nejman *et al.* tumor microbiome, Unified Human Gastrointestinal Genomes (UHGG) collection, and Genomes from Earth's Microbiomes (GEM). Only sets with a minimum size of 7 are shown for visual clarity. **e**) The genera that are at the intersection of all these datasets are shown. Presence (light boxes) and absence (dark boxes) of each genus is shown. bm: bone marrow, li: large intestine, si: small intestine, panc: pancreas, GBM: glioblastoma multiforme.

SI Text

SIMBA, a computational pipeline for the identification of bacteria, viruses and fungi in single cells

With the rapidly rising number of single-cell transcriptomic datasets, there is a growing interest in detecting microbial transcripts within these datasets. Although there are many existing tools for microbial profiling in standard metagenomic datasets, tools that take single-cell transcriptomic data as input are currently more limited[83]. There are however a growing number of pipelines being developed for this purpose, including those developed by Robinson et al. (CSI-Microbes)[84], Ghaddar et al. (SAHMI)[23], and Llorens-Rico et al.[85]. CSI-Microbes supports three different existing tools for detection of microbial sequences, namely GATK PathSeq[86], CAMMiQ[87] and SRPRISM[88]. GATK PathSeq relies on BWA-MEM alignments, replacing its original use of BLAST[89] in favor of faster alignment speed. Llorens-Rico's pipeline uses Kallisto pseudo-alignments against a reference database of ~12K microbial reference genomes. SAHMI implements kmer-based aligners against a microbial and human reference dataset and implements additional filters to detect false positives.

In our pipeline, called **Si**ngle-cell **M**ultibiome **B**LAST **A**nalysis (SIMBA), we first use UMI-tools[33] to filter and extract cell barcodes and UMIs from raw fastqs using the *extract* and

whitelist commands. We used STAR[34] (v2.7) to align resulting sequences against a reference library containing the human genome (GRCh38.p13) and ERCCs. We then took unmapped sequences for further processing. We wrote *poly.py* to eliminate low-complexity sequences with high fractions of consecutive bases, often representing primer dimers and other sequences with long stretches of polyA. We used BLASTn[35] (v2.10) to align against several custom databases followed by the nt database, which is one of largest publicly available databases, consisting of ~70 Million sequences (11/02/2020) pooled from GenBank, EMBL, DDBJ, PDB, and RefSeq databases. Taxonomic lineages for each top hit against the nt database were added using TaxonKit[90]. Top hits were filtered based on their taxonomic assignment to include only viral, bacterial and fungal species.

The premise behind creating a pipeline that relies on BLAST given its high computational cost, is based on our early observations that some of the faster tools for microbial profiling can result in an unacceptably high false positive rate. As an example of a kmer-based profiling method, which are among the most popular and widely used methods for microbial profiling, we explore instances of false positives from Kraken2 against the nt database using several truth datasets. We demonstrate why in the context of our dataset, where the vast majority of sequences are human-derived, such tools lack the necessary precision (see **SI: Benchmarking Kraken2 precision and recall**). Robinson et al. similarly employ GATK PathSeq rather than faster kmer-based profiling methods[84,87]. We further show that while Kraken2's recall is high when the input sequences are sampled from the Bacterial Refseq dataset, it is highly variable and can be much lower when the input sequences are sampled from other datasets. This is one example illustrating why alignments using BLAST against large, comprehensive reference databases such as nt are still widely considered the gold standard in precision against which new tools are often benchmarked[91–94]. Because the study of microbiomes in low-biomass settings presents a high burden of proof with many potential sources of false positives, in our approach we favor precision over computational time and recall. In these settings, we and others argue that the problem of bioinformatic false positives is critical[89,92,95,96] and on par with the problem of experimental false positives, or contamination.

However, aligning large datasets against large databases using BLASTn is computationally infeasible even with access to large compute clusters. To lower this computational cost, we created a lean human-microbiome centric database for bacteria and fungi which we call microbDB (see **SI: Creating custom databases to limit the computational burden of BLASTn against the nt database**). We use microbeDB as a first-pass filter to select sequences with the highest likelihood of being bacterial or fungal in origin. Additionally, through subsampling, we created leaner versions of the publicly available bacterial and fungal RefSeq databases[97] to use as second-pass filters. Viral

739 sequences were aligned against the Viral RefSeq database[97] (release 98) which included
740 9,000+ viral genomes. Surviving sequences that produced significant alignments or "hits"
741 (E-value < 10-5) against these intermediate databases were then aligned against the nt
742 database. This particular E-value threshold is commonly used[98–101]. For each sequence
743 the top significant hit (lowest E-value) was selected for downstream analysis. We wrote
744 *dedup.py* to create input fasta files with sequences that produced a top hit in this step,
745 and use the resulting file to BLASTn against the nt database. By taking this type of
746 screening strategy, we lower the computational burden of alignments by ~100 fold.
747 Without the initial screening, we would require ~3 x 10^8 CPU hours, equivalent to ~$9
748 million using Amazon's compute instances (estimate made in 2020).
749
750 The resulting top hits that emerged from the viral, bacterial and fungal workflows against
751 nt were combined into one dataset consisting of ~19 million sequences for further
752 processing and quality control. Despite first filtering human reads using the STAR
753 alignment step, out of ~19 million sequences that generated significant hits against nt,
754 only 12% mapped to the viral, bacterial, and fungal biomes of interest, while half of them
755 mapped back to the human genome. This indicates the importance of implementing
756 multiple checkpoints to eliminate non-microbial reads, and cautions against relying solely
757 on smaller databases without validation against a comprehensive database such as nt.
758 This is especially relevant to human tissue samples where the ratio of non-microbial to
759 microbial sequences is high[86,89,95].
760
761 We applied our pipeline not only to the raw data underlying Tabula Sapiens annotated
762 single cell dataset but all the raw data, including those from empty droplets, which we
763 refer to as the Tabula Sapiens Microbiome F00 (TSM F00) dataset. The rationale for
764 including unannotated or empty droplets is that we suspect that microbial reads from
765 extracellular environments could appear in those droplets, and more generally, different
766 species may have different patterns of association with these two categories of droplets.
767 Later we incorporate this information for each species as a parameter in our machine
768 learning models for decontamination. Using TSM F00 as input, we analyzed reads from
769 150+ Million droplets, ~1.3 Million of which had more than 200 human genes and that we
770 treat as potentially cell-containing. By matching the droplet barcodes (along with sample
771 name) to those found in the Tabula Sapiens objects, we were able to acquire the cell type
772 annotations for a portion of the cell-containing droplets. For all other droplets, we provide
773 tissue and donor information. Please see **Data and Materials Availability** for the Jupyter
774 notebook where details of cell-containing and empty droplet counts using cell ranger can
775 be found.
776
777 The output of SIMBA once filtered to contain only bacterial, fungal or viral hits was 2.4
778 Million significant hits. There were ~724K significant unique hits (counted based on

Unique Molecular Identifiers or UMIs) arising from ~0.5 Million droplets - 79K cell-containing droplets (~6% of TSM F00 cell-containing droplets) and ~380K empty droplets (~0.3% of TSM F00 empty droplets). This dataset is what we will refer to as the TSM F0 dataset.

Creating custom databases to limit the computational burden of BLASTn against the nt database

RefSeq databases[97] for bacterial and fungal genomes are available through NCBI, however they are typically large databases that would create significant computational bottlenecks. We created several custom databases to serve as lean human-microbiome centric databases for the initial iteration of BLASTn search for bacterial and fungal sequences. This was not done for viruses as they have much smaller genomes relative to bacteria and fungi and thus the viral RefSeq could be used directly.

MicrobeDB was constructed by combining two other custom databases, bacteriaDB and mycoDB. BacteriaDB was designed by taking the intersection of the HumGut database[102], a comprehensive database of ~30,000 prokaryotic genomes mined from ~5,700 healthy human metagenomes, and the bacterial RefSeq database (downloaded on 01/2021). The HumGut dataset was obtained from https://arken.nmbu.no/~larssn/humgut/. We therefore identified the unique set of species in HumGut and eliminated entries with unidentified species-level taxonomy. Similarly, we identified the unique set of bacterial RefSeq entries, and took the intersection of these two sets to arrive at several hundred bacterial species. We used a similar strategy to bias the initial search for fungi towards species previously identified in human mycobiome studies. We took five representative species from each genus found in both the fungal RefSeq (downloaded on 01/2021) and a recent survey of the healthy human mycobiome[103] to create mycoDB. While microbeDB was used for the first search iteration, larger databases were used for the second iteration. These larger databases, slimBacterial_RefSeq and slimFungal_RefSeq are the reduced versions of the bacterial and fungal RefSeq databases which we subsampled to include representative species and strains. Please see **Data and Materials Availability** for the Jupyter notebook where details of how intermediate databases were constructed is described.

Benchmarking SIMBA's precision and recall

We evaluated SIMBA's precision and recall against several truth datasets. For all truth datasets, we randomly selected sequences that were 100 bases long to match the length of sequences in the TS dataset. We will refer to each sequence from truth datasets as

816 “input seq” and its corresponding output hit from SIMBA as “output seq”. If an input seq
817 goes undetected by way of not producing any corresponding output seq, we count that
818 as a false negative. We use taxonomic IDs on input and output seqs to measure precision
819 and recall at each level of taxonomic classification. For example, if an output seq does
820 not match an input seq in taxonomic ID or species name, we consider that as a false
821 positive at the species level of classification.
822
823 First, we created a dataset of 2400 sequences derived from human chromosomes
824 (GCF_000001405.39_GRCh38 assembly) including X and Y, with 100 randomly selected
825 sequences from each chromosome. We then employed SIMBA’s bacterial and fungal
826 branch of the pipeline without using STAR to eliminate human-derived sequences as we
827 knew most of these input seqs would already be eliminated at this step. Even without this
828 step, the pipeline did not produce any false positives. Only one input seq produced a hit
829 when aligned against microbeDB and that sequence was eliminated in the subsequent
830 alignment step against the next larger intermediate database, thus no false positives were
831 detected.
832
833 We also used this truth dataset against the viral branch of the pipeline, again forgoing the
834 STAR alignment step. Out of 2400 sequences, 65 produced hits against the viral Refseq
835 database, and were subsequently aligned against the nt database. At this stage, all these
836 sequences were correctly identified as human in origin, including one human retroviral
837 sequence. Thus, SIMBA produced no false positives when encountering human-derived
838 sequences, which is an important aspect of this pipeline considering the high ratio of
839 human to non-human sequences in the TS dataset and in human tissues more broadly.
840
841 Next we tested SIMBA’s performance when encountering viral sequences. To create a
842 truth dataset, we randomly selected 100 viral genomes and selected 10 random
843 sequences from each genome using the viral RefSeq database. This resulted in
844 sequences from 62 genera of viruses, thus representing a diverse viral truth dataset. We
845 found that all input seqs produced an output seq. Interestingly we noticed that some
846 mismatches that were encountered between the taxonomic IDs of input and output seqs
847 were the result of finding a prophage output seq when the input seq originated from a
848 phage. Because the prophage is embedded in a bacterial genome, the resulting output
849 seq had the taxonomic ID of the host bacterium. We excluded these special cases from
850 calculations of precision and recall. At the species level, we see the following precision
851 and recall, respectively: 0.8, 1 **(SI Table 1)**. False positives detected at the species level
852 correspond to sequences from highly similar viral species that typically share the same
853 host **(SI Table 2)**. This is expected as short sequences (e.g. ~100 bp) can be shared
854 identically or with very high similarity among related species. Indeed, we found that all
855 false positives had 100% sequence similarity across the entire length of the input seq **(SI**

Table 3). Hence, genus level classification provides a more meaningful depiction of precision as it is less prone to this type of ambiguity in the mapping of short reads. Indeed, the precision jumps to almost 1 when examined at the genus level.

Moreover, the high recall associated with our viral search is expected given that we did not use intermediate, subsampled databases to lower the computational cost for the viral search since it does not pose a computational bottleneck. The lower computational cost of searching for viruses is a result of viruses having 1) some of the smallest genomes across all domains of life, and 2) fewer representatives than bacteria in many databases, including the nt database.

Next, we characterized false positives as well as other parameters in the face of bacterial input seqs. Given that environmental bacteria can be a source of contamination in kits and reagents, we aimed to bias SIMBA to finding those bacteria that are more likely to reside in the human microbiome to 1) mask potential contaminants and 2) limit the initial search space to reduce the pipeline's computational time. To introduce this bias, we created microbeDB which serves as a first pass filter on the input data. This database is composed of bacteria and fungi commonly found in the human gut microbiome, based on the assumption that the gut likely contributes the most to human tissues due to its greater microbial biomass compared to any other site in the human body. Therefore, to evaluate the pipeline's performance, our first truth dataset contained bacteria cultured from the human gut microbiome.

We obtained taxonomic IDs from the Human Gastrointestinal Bacteria Culture Collection (HBC) - to select representative genomes from 50 random bacterial species cultured from the human gastrointestinal tract, for which we downloaded a representative genome from NCBI. We obtained the Human Gastrointestinal Bacteria Culture Collection (HBC) dataset from https://www.ebi.ac.uk/ena/browser/view/PRJEB23845?show=reads (filereport_read_run_PRJEB23845_tsv.txt). We then selected 100 random contigs, for a total of 5000 sequences. Using this truth dataset, we report the corresponding precision and recall **(SI Table 4)**. At the species level, we arrive at the following precision and recall, respectively: 0.69, 0.22. As with the viral truth dataset, when we analyzed the false positives, we found that the vast majority represent sequences from highly related bacterial species **(SI Table 5)** with nearly identical or 100% identical output seqs to input seqs. We again see a jump in precision to 0.93 going from the species level of classification to the genus level. We have a recall of 0.28 at the genus level, and thus we likely underestimate the true number of bacterial species using this pipeline. However, we wanted to limit instances of false positives even at the expense of false negatives. In future iterations of this pipeline, increasing the size and diversity of microbeDB would likely enhance the pipeline's recall.

To test how well SIMBA identifies members of another microbiome, we created a truth dataset based on the expanded Human Oral Microbiome Database (HOMD), consisting of 50 randomly selected genomes and 100 randomly selected segments from each. The expanded Human Oral Microbiome Dataset (HOMD) was obtained from https://www.homd.org/download#genome, specifically from HOMD_taxon_table2022-09-15_1663245201.txt and HOMD_genome_table2022-09-15_1663245202.txt files. Unexpectedly we found similar values for precision and recall across different classification categories **(SI Table 6)**. This stands in contrast to the metrics we obtained when we used a truth dataset that was not focused on bacteria from the human microbiome.

We randomly selected 50 bacterial genomes from the bacterial Refseq database, and randomly selected 100 sequences from each genome for a total of 5000 sequences. Comparing the performance results of this truth dataset at the genus level to the gut or oral bacteria truth datasets, we see that while the precision remains high, recall has dropped down to only 0.05 **(SI Table 7)**. Thus, the pipeline preferentially recalls bacteria from the human microbiome compared to any randomly selected bacterial sequence. It can mask potential contaminant bacterial sequences. Even those input seqs that produce output seqs have a high chance of being correctly identified due to the pipeline's high precision afforded by the last BLASTn step against the nt database.

We created a fungal truth dataset by taking ~5000 sequences randomly sampled from a study of the gut mycobiome[104]. At the genus level, we found similar values of recall and precision to those we found for the bacterial truth datasets created from HOMD and HBC (**SI Table 8**). Please see **Data and Materials Availability** for the Jupyter notebook where our integration of datasets for benchmarking SIMBA is described in detail.

Benchmarking Kraken2 precision and recall

We tested the precision and recall of a popular tool in the field of microbial metagenomics, Kraken2, both against the microbial truth datasets that we created to test SIMBA as well as a sample of the Tabula Sapiens dataset. We chose Kraken2[105] as it is one of the fastest and most accurate metagenomic taxonomic profiling tools available, and in general Kmer-based approaches to fast taxonomic profiling represents a good fraction of the tools that are available[91].

This was done primarily to see whether Kraken2's speed performance would justify its use for our dataset. We assembled the nt database to use Kraken2 against. We found that, in agreement with a previous benchmarking study[91] of Kraken2 and related tools, Kraken2 has very high precision and recall against the bacterial RefSeq truth dataset **(SI**

936 **Table 9)**. However, its recall is quite lower for the other bacterial truth two datasets,
937 starting from 0.53 at the genus level against the truth dataset created from HBC **(SI Table**
938 **9)**.
939
940 Upon removing human-derived sequences using STAR for a bladder sample from the
941 Tabula Sapiens dataset, we used Kraken2 against the nt dataset. Kraken2 created
942 outputs marked classified and unclassified. More than 60% of reads remained
943 unclassified at the species level, and nearly half of the reads still remained unclassified
944 at the domain level **(SI Figure 2a)**. Using the provided taxonomic IDs, we obtained
945 taxonomic lineage information for reads that were classified.
946
947 Among the classified reads, ~285K were identified as eukaryotic, ~2.7M as bacterial and
948 ~1.1M as viral **(SI Figure 2b)**. To test the precision and recall of these classification calls,
949 we subsampled each domain (except Archaea) and randomly selected 100 sequences
950 from those reads that had acquired full classification up to the species level. We then
951 used BLASTn against the nt database to measure the extent of the agreement between
952 Kraken2 and BLASTn taxonomic classifications. Surprisingly, we found very little
953 agreement and a high rate of false positives associated with Kraken2 classifications. For
954 bacteria and viruses, the mean precisions at the genus level are 0.06 and 0.04,
955 respectively **(SI Table 10)**.
956
957 Taking a closer look at instances of false positives for reads that Kraken2 classifies as
958 various species of bacteria, we see that many are classified as human (and other primate
959 species) **(SI Table 11)**. Human reads that are not sufficiently eliminated by STAR present
960 a major challenge for Kraken2. This issue of high false positive rate when analyzing
961 clinical samples has been discussed in the past[89,91]. Given a large enough number of
962 human reads, as is the case with Tabula Sapiens datasets, many sequences will be
963 misclassified as microbial or viral using this tool. On the contrary, because our pipeline
964 relies on BLASTn against nt, it has significantly better precision than kmer-based
965 approaches. Hence, we could not justify the faster speeds associated with some of the
966 existing metagenomic classification tools over their lack of extreme precision for this
967 specific application.
968

969 **Measures against contamination during tissue recovery and transport**

970 As detailed by the Tabula Sapiens consortirum[28], the tissues were procured at various
971 hospitals through collaboration with Donor Network West (DNW, CA) - a not-for-profit
972 organization that is a federally mandated organ procurement organization. Tissues were
973 procured consistently across all donors across different operating rooms (OR).
974 Contaminants from air, hair, skin, and instruments were carefully mitigated using strict

aseptic techniques as outlined by the American Association of Tissue Banks (AATB) some of which is briefly discussed in the following paragraphs.

In each OR, multiple sterile fields are created. A sterile field is created for each time a pair of sterile gloves or gowns is opened. An additional sterile field is set using sterile surgical drapes around a surgical site. Several sterile fields are created on tables where sterile surgical instruments are placed. Another sterile field is created on a table where storage and shipping supplies are placed.

To mitigate the risk of contamination from air, the OR rooms used to recover organs contain elaborate air filtration systems, and OR personnel are required to wear sterile PPE such as a face mask at all times. They also wear hair bonnets prior to putting on surgical scrubs and maintain them at all times. The OR personnel scrub their hands and arms before a procedure; using sterile surgical attire as barriers between their skin and recovery environment, they then prepare the donor for tissue recovery.

The donor is prepped for tissue recovery using rigorous aseptic protocols as outlined by AATB (cite). First, clothing is removed, and hair is removed from any recovery areas using surgical scrub soap to prevent contamination from the donor's skin. These areas are then wiped with 70% Isopropyl Alcohol to disinfect the skin while also removing any loose hair or debris not removed by the surgical soap. FDA-tested and approved surgical soaps are used. Donor draping is performed using aseptic standards of practice to isolate, form a barrier and create a sterile field. Recovered organs are protected by a triple sterile barrier and stored in enough cold, sterile preservation solution (UW solution) to sufficiently cover the organ or vessel. To capture any contamination possibly introduced through the UW solution, we performed sequencing of this solution.

It is important to note that given our study relies on post-mortem samples, thus there is a possibility of tissue barrier breakdown that would impact microbiomes. To partly address this concern, we set up a private courier service to keep the time between organ procurement and initial tissue preparation to less than one hour. This is a relatively short period considering that heart and lung procured for transplantation are viable for 4-6 hours, liver for 8-12 hours, and kidneys for 24-36 hours. As tissues were recovered in the same manner as those used for transplantation, and were rapidly prepared for single cell sequencing, the possibility of gross tissue breakdown is low. Additionally, histological staining of tissues showed viability along with certain markers used to identify rapidly dividing cells (e.g. transient amplifying cells of the intestinal epithelium)[28]. Using single-cell transcriptomes, we could differentiate between hundreds of cell types, identify differentiation trajectories, and tease apart different phases of the cell cycle[28]. Together these findings point to cellular and tissue viability at large.

1015 **Identification of contaminants based on negative controls and external datasets**
1016 **(Filters 1-3)**

1017 The introduction of contaminants was mitigated during tissue procurement in the OR
1018 setting by creating sterile fields and various other strict measures as these tissues were
1019 collected in the same manner as those recovered for organ transplantation. These tissues
1020 were placed in UW solution and then within sterile bags on ice and quickly shipped to
1021 different tissue expert labs to preserve tissue and cellular viability. Within different labs,
1022 organs were further dissected into smaller tissue pieces and digested to create single-
1023 cell suspensions in preparation for single-cell sequencing. A detailed description of tissue
1024 procurement and transport is provided in **SI: Measures against contamination during**
1025 **tissue recovery and transport.**
1026
1027 There are multiple potential sources of contaminants, including contamination introduced
1028 during tissue procurement, tissue transport, tissue digestion and sequencing. However,
1029 we suspect that different sources of contamination do not have equal contribution to the
1030 total list of contaminants in each sample. We posit that for dense tissue types,
1031 contaminants from instruments, reagents, or air are exposed primarily to the surface of
1032 each tissue sample, and thus surface area to volume ratio, SA:V, is an important physical
1033 constraint on each contamination source. We will illustrate the importance of SA:V using
1034 simple back-of-the envelope estimates, assuming samples are cubes for simplicity. For a
1035 cube, SA:V is (6 x s^2)/(s^3) or 6/s, where s is the length of a side. Let us assume the
1036 organ recovered in the OR is 10 cm on each side, and that it is further dissected into 1
1037 cm cubes in a lab and digested into 10 um cubes (or cells). In this process, the SA/V ratio
1038 starts at 0.6 cm^-1 in the OR setting. Then in the lab setting, it goes up to 6 cm^-1 at the
1039 dissection step and then to 6000 cm^-1 during the tissue digestion and single-cell
1040 suspension step. Because of the increase in SA:V, we estimate that contaminants are
1041 orders of magnitude more likely to come into contact at the tissue digestion and
1042 sequencing steps than they are at tissue procurement, transport or dissection steps.
1043
1044 All labs performed tissue digestion and sequencing using aseptic techniques, however
1045 because these samples were largely intended for studying the human transcriptome, no
1046 blank instrument or reagent controls were generated at the time of the original
1047 experiments. In absence of these controls, we partnered with the labs that had processed
1048 these tissues and obtained reagents and consumables from the following tissue experts
1049 for the Tabula Sapiens project: bladder, blood, bone marrow, fat, heart, intestines, kidney,
1050 liver, lung, lymph node, muscle, pancreas, salivary gland, skin, spleen, thymus, trachea,
1051 uterus, and vasculature. The reagents and consumables are listed by tissue in **SI Table**
1052 **12**. The tissue dissociation protocols were performed exactly as detailed by the Tabula
1053 Sapiens consortium[28] in small scale (~250 µl final eluate) but in the absence of tissue.

These protocols included incubation steps, centrifugation, sample filtration using cell strainers, enrichment using MACS columns, among other steps. Even when the same reagent was used across different labs, we obtained each lab's specific batch of that reagent to account for lab-specific contaminants.

Equal volumes of supernatants obtained at the end of tissue dissociation protocols were pooled and mRNA seq libraries were generated using the Chromium Next GEM Single Cell 3' v3.1 chemistry (10X Genomics, Pleasanton, CA). Each pool was loaded onto a Chromium G Chip channel for a total of 5 channels. Libraries were prepared using manufacturers recommendations. All PCR reactions were performed using the Biorad C1000 Touch Thermal cycler with 96-Deep Well Reaction Module. As per 10X Genomics protocol recommendation, amplified cDNA and libraries were evaluated on a 2100 Bioanalyzer system (Agilent Technologies, Santa Clara, CA). Libraries were sequenced on the NextSeq 500 (Illumina, San Diego, CA) to obtain a total of 86 million reads.

With ~200 negative control samples, we arrived at a list of contaminant species. When we excluded all species found in negative control samples, the number of unique hits was reduced to ~63K, or roughly 9% of the TSM F0 unique hits. Interestingly, the number of species dropped from ~8200 to only ~7100 and the number of genera went down from ~2500 to ~2400. Filter 1 reduced the numbers of cell-containing and empty droplets to ~13K (~17% of TSM F0 cell-containing droplets) and ~44K (~12% of TSM F0 empty droplets), respectively.

We then imposed a second filter based on genera commonly found in negative controls from previous studies[36], which we will refer to as the Salter genera. The removal of these genera reduced the number of unique hits, species and genera to ~52K, ~6200, and ~2300, respectively. It reduced the numbers of cell-containing and empty droplets to ~12K and ~35K.

Next we measured $R_g = \frac{c_g}{TS_g}$ where TS_g represents the number of species from genus *g* found in the TSM dataset, and represents the number of species from that genus in the negative control dataset. This simple parameter can provide insight into how confidently species from a given genus can be flagged as true signal or contaminant. For example, if a considerable fraction of species in a genus found in the TSM dataset are also identified in the control dataset (high R_g), our confidence in other species from that genus would be lower than in the reverse scenario. This is because as we showed through benchmarking of both BLASTn and Kraken2 against several truth datasets, species-level taxonomic assignments based on short reads (~100 bases) are less precise than genus-level taxonomic assignments. It is also possible to experimentally undersample contaminants and miss certain species. However, blanket removal of genera may also result in a

significant loss of true signal. Moreover, comparing the distributions of R_g for Salter genera versus all others in the TS dataset, we observe significantly larger values (one-sided Mann-Whitney U test, $P < 10^{-5}$), providing support that this parameter can be used to help distinguish between genera that are known contaminants versus true signal. Thus, rather than defining an arbitrary cutoff for R_g, we incorporated it in several machine learning models of contamination (described in the next section) and allowed these models to learn this parameter along with others. Indeed, the inclusion of R_g boosted the area under the precision recall curve (AUPR) as well as the area under the receiver operator curve (AUROC) for the machine learning models discussed in the next section.

We imposed a third filter to eliminate putative fungal species based on a recent study of fungi in human tissue samples[20]. This filter reduced the number of species to ~6100. Other numbers remained nearly the same (rounded numbers do not reflect a change, see exact numbers in **SI table 13**).

Machine learning models of contamination (Filter 4)

Despite having collected many negative control samples representing reagents and instruments used by the Tabula Sapiens consortium, we built 6 different types of machine learning (ML) models to learn the shared features of the known and putative contaminants in the TSM dataset to identify potentially missed contaminants. We used the best performing model to identify putative contaminants in the part of the dataset that is withheld from training and testing. As input to each model was a table where the rows were species and the features were: 1) number of tissues and 2) number of donors positive for that species, 3) abundance of that species, 4) median percent identity and 5) median length of alignments corresponding to that species, 6) R_g (described in the previous section), 7) domain-level taxonomic assignment, and 8) median number of genes per droplet in which the species was identified. The last parameter is included to incorporate information about whether the sequence corresponding to a given species is coming from an empty droplet or from a cell-containing droplet. The premise behind including the last parameter is that we suspected contaminants and true signals may have different patterns of association with those two classes of droplets. Counts of empty droplets were performed using Cell Ranger (v6.0.1) in addition to a custom script for downstream analysis (see **Data and Materials availability**).

If a species was flagged as a known or putative contaminant by any of the first three filters (see previous section), it was considered as a contaminant (labeled 1). This dataset was split into parts A (25% of total) and B (75%). Part A dataset was split into training

(80%) and test (20%) subsets (**SI Figure 1.c**). We built k-nearest neighbor, multi-layer perceptron, gradient boosting, random forest, logistic regression, and support vector RBF (radial basis function) models. Because the total dataset (part A + B) contains a small fraction of contaminating species, it represents an imbalanced dataset where the detection of the minority positive class, or contaminant species, is of interest. Thus, to balance the training dataset (and only the training dataset), we employed SMOTE (Synthetic Minority Oversampling Technique)[106] to generate synthetic minority class instances from existing ones. Next, we tested the models on the unseen test dataset and repeated this process 10 times using different train/test splits to generate 95% confidence intervals for test performance. We report the performance of the model on test data. The test AUPR and AUROC performance for the models are provided in **SI Figure 1.d**, ordered by the median value. The 95% confidence intervals for AUPR and AUROC values are provided in **SI Table 14** and **SI Table 15**. Further details on model creation and hyperparameters is provided in p07_machine_learning_modeling_contamination_and_other_filters.ipynb (see **Data and Materials availability**).

Although we provide AUROC test scores, we rely primarily on AUPR as the performance metric of interest since AUROC may be artificially high when the dataset consists of a minority positive class[107], though in our case the dataset is only moderately imbalanced. The null AUPR, which corresponds to the prevalence of the positive class, is ~0.3 and denoted by the dashed line (**SI Figure 1**). The gradient boosting classifier (GBC) had the highest median AUPR test scores (95% confidence interval: 0.75-0.78) and highest median AUROC (95% confidence interval: 0.82-.84).

We then fit the GBC model trained and tested in Part A to Part B. We eliminate the known and putative contaminants in part B (based on filters 1-3) as well as the putative contaminants identified by the GBC model (filter 4). While some of the species will be falsely labeled as contaminants, we take a conservative approach and eliminate them from further analysis. The application of the GBC decontamination model reduced the number of unique hits, species and genera down to ~41K, ~4700, and ~2200. It lowered the numbers of cell-containing and empty droplets with hits to ~10K and ~28K.

Gaussian Mixture Model of alignments (Filter 5)

BLASTn outputs with E-values < 10^{-5} against the nt database are conventionally considered significant[98,99]. In addition to E-value, BLASTn outputs two parameters that characterize the quality of each alignment, namely percent identity and the alignment length. By multiplying these two parameters and dividing by 100, we arrive at the total

number of bases with a perfect match, which we refer to as n_match. Although all significant hits had E-values < 10^{-5}, the distribution of n_match was a bimodal distribution (**SI Figure 3**). We use a Gaussian Mixture Model (GMM) to separate these two distributions. Because a species can have hits from both distributions, we systematically eliminated species if they were represented by more hits from the second distribution (μ_2 = 91 bases) than the first (μ_1 = 62 bases). We posit the first distribution represents lower-quality alignments that may be biologically interesting, as in the case of sequences from uncharacterized microbes with only a distant relative in the current nt database. They may also be technical artifacts. We take a conservative approach and favor precision over recall and impose this filter. A similar combination of filters has been used by Joint Genome Institute's microbial genome annotation pipeline (E-value ≤1e-5, ≥ 90 percent identity, alignment ≥ 80 %)[102] and by the Kraken team when benchmarking their tool against BLAST (E-value ≤10−5 and percent identity ≥90%)[99]. With the application of the GMM on the alignments, we arrived at ~13K unique hits, ~2300 species, and ~1100 genera from ~1K cell-containing droplets, and ~11K empty droplets.

Identifying putative habitats of origin for 500+ bacterial genera in the Tabula Sapiens Microbial dataset using the Genomes from Earth's Microbiomes, the Human Microbiome Project, and the Unified Human Gastrointestinal Genome collection (Filter 6)

In addition to experimental (Filter 1) and bioinformatic decontamination (Filters 2-4) and alignment QC (Filter 5) steps, we wanted to capture information about the likely habitats of origin for TSM F5 taxa. We posit that some fraction of these species resides in the human microbiome's external facing sites and have been observed in prior human microbiome studies, while the rest may be species that are transiently introduced via inhalation and consumption, among other possible means of transport, or may represent less frequently observed taxa in the human microbiome. To identify and separate members of these two groups, we leveraged the Genomes from Earth's Microbiomes[7] (GEM) dataset to gain insight into the likely habitats from which bacterial hits in the TSM F5 dataset originate. The GEM dataset is derived from 10,000+ metagenomes sampled from various habitats across the earth including terrestrial, aquatic, human and animal hosts, engineered environments, among others. This extensive dataset includes more than 12000 species-level operational taxonomic units.

We obtained the metadata for the GEM dataset from https://portal.nersc.gov/GEM/genomes/ (genome_metadata.tsv). While most bacterial genera were either strictly host-associated or free-living, some contained species that belonged to both habitat categories. Thus, to identify the dominant habitat of for each

genus, we labeled species based on three categories: 1) “Human-associated” species include organisms found in the human microbiome; 2) “other_hosts” are species isolated from non-human vertebrates, invertebrates, fungi, and plants; 3) “free-living” are those species isolated from human-built or natural environments. With a table where each row represented a genus, and each column represented the fraction of its species belonging to one of these three categories based on the GEM dataset, we performed K-nearest neighbor clustering (number of clusters=3) and assigned each genus to a cluster (**SI Figure 4)**. We created a filter here called GEM_1 which is set to 0 (0=keep) for genera found in the human-associated cluster, and set to 1 (1=remove) if found in the other two clusters. GEM_1 is set to NA (NA=not applicable) if a genus is not found in the GEM dataset. We also created another filter called GEM_2 that functions in the same way as GEM_1 but for species. The combination of the two filters (GEM_1_2) allows for GEM_2 to override GEM_1. In other words, unless there is habitat information for a given TSM species, we assume the filter applied on to its genus.

In addition to the GEM dataset, we obtained habitat data for bacterial species from the Unified Human Gastrointestinal Genome (UHGG) collection[5] and the Human Microbiome Project (HMP). The UHGG dataset is a large-scale and recent dataset of gut prokaryotes, comprising ~200K non-redundant genomes from more than 4000 gut prokaryotes. These genomes are collected from humans living across 31 countries and 6 continents. This comprehensive catalog includes genomes from the Gastrointestinal Bacteria Culture Collection[29], the Culturable Genome Reference[108], as well as cultured human gut genomes from NCBI, PATRIC[31] and IMG[109] datasets, as well as metagenome-assembled genomes from Pasolli et al.[110], and Nyfach et al.[7] studies. We gathered the Unified Human Gastrointestinal Genome (UHGG) collection dataset from http://ftp.ebi.ac.uk/pub/databases/metagenomics/mgnify_genomes/human-gut/v2.0.1/ (genomes-all_metadata.tsv). We created a filter called UHGG_species, which is set to 0 (0=keep) if a TSM species has been identified in the UHGG dataset. It is otherwise set to NA.

The Human Microbiome Project (HMP) dataset acquired from https://www.hmpdacc.org/hmp/catalog/grid.php?dataset=genomic consisted of ~3000 entries primarily from bacterial strains from various isolation sites. We chose species found in external-facing microbiomes (oral cavity, gastrointestinal tract, urogenital tract, airways, and the skin). When comparing the TSM dataset to these two datasets, entries with unknown taxonomic assignments were excluded. We created a filter called HMP_species, which is set to 0 (0=keep) if a TSM species has been identified in the HMP dataset. It is otherwise set to NA.

Filter 6 combines filters based on **H**MP, **U**HGG and G**E**M datasets, or what we refer to as the HUE datasets. Explicitly, the HUE filter (filter 6) is set to 1 (1=Remove) if any of the GEM_1_2, UHGG_species or HMP_species filters is equal to 1. The HUE filter will be set to 0 (0= Keep) if any of the three filters is equal to 0, effectively overriding the previous condition. Hence, if in one dataset a given species is found to be human-associated, and in another it has been found as not human-associated, we consider the species to be human-associated. The HUE filter is set to NA if all three filters it comprises are set to NA.

Based on the HUE filter,159 species were determined to be human-associated and the rest originated from other hosts or environments, or were not found in these datasets. To obtain putative habits of origin for those species in the NA category, we used OpenAI's Davinci large language model described in the next section. Removing bacterial species and genera based on their habitat of origin in the HUE datasets further reduced the number of unique hits, species, and genera down to ~10K, ~1700, and ~900, respectively, originating from 1K cell-containing droplets and 8K empty droplets. Please see **Data and Materials Availability** for the Jupyter notebook where further details for incorporating the GEM, UHGG, and HMP datasets into TSM dataset can be found.

Benchmarking and employing Davinci large language model for identification of putative habitats for 1500+ microbial species (Filter 7)

The HUE datasets provide putative habitat information for many taxa, however they do not include all taxa found in the TSM dataset. Specifically, there were 1500+ species for which filter 6 (the HUE filter) does not provide any information. To systematically retrieve information on where these species have previously been isolated from, we employed openAI's Davinci Large Language Model (text-davinici-003 accessed Jan 2023). We simply asked the following question for each species: "provide a short summary of where species_i has been isolated from", where species_i corresponds to the species of interest. To make queries programmatically, we employed openAI's API and set max_tokens=200. We used the following default parameters: temperature=0.5, top_p=1, frequency_penalty, presence_penalty=0.

To better understand the model's level of self-consistency, we randomly chose 10 species and posed the same prompt three times. A table of model outputs for all three runs is provided in **SI table 16** and shows that the model presents a certain level of variability across multiple outputs from which we can identify high-confidence segments based on consensus across all three outputs. For example, here are the three outputs for *Acidaminococcus intestini*: Output 1: "Acidaminococcus intestini has been isolated from the gut of humans and pigs, as well as from soil samples and wastewater". Output 2:

"Acidaminococcus intestini has been isolated from the intestinal tracts of humans, pigs, chickens, and horses. It has also been found in soil, water, and sewage". Output 3: "Acidaminococcus intestini has been isolated from the intestinal tracts of humans, pigs, and chickens. It has also been detected in the feces of horses and cows, as well as in the environment".

Next to test the validity of the model's outputs, we randomly selected 100 species from the GEM dataset, providing us a subset of habitats that a given species has been previously isolated from. By running three independent queries per species and combining the model's outputs, we were able to estimate the model's precision and recall. First, we created two categories, based on whether a given species was previously isolated from the human microbiome or not (i.e. species isolated from natural environments, human-built environments, or non-human hosts). Then we grouped Davinci's responses based on the same two categories. Using GEM as the truth dataset, we found that the model was able to identify 59 out of 63 species previously found in the human microbiome. Out of 37 species not found in the human microbiome, the model correctly identified 25. The model outperformed the truth dataset in some cases. For example, among the model's false positives, we noticed four species that had been found previously in the human body by other studies (*Serratia plymuthica*[111], *Leifsonia sp.*[112], *Rickettsia japonica*[113], and *Lysobacter oculi*[114]). Correcting for these four species, we arrive at a precision of 89% and a recall of 94%. We provide a table of these 100 test species along with GEM habitat categories and model outputs (**SI table 17)**. To increase the precision further, we only accepted species that had been identified as having been found in humans by all three Davinci outputs. Again, *Serratia plymuthica* and *Lysobacter oculi* were both found in humans by all three Davinci outputs and thus were counted as true positives. We arrived at a precision of 98% and a recall of 75% (see **SI Figure 1.e** for the confusion table). Details of programmatic query submission along with benchmarking can be found in a Jupyter notebook listed under **Data and Materials Availability**.

It is important to state some of the limitations of the current Davinci model. First, we found the model's self-consistency depends on the prompt. Generally, the simpler and more open-ended prompts provided better, less biased outputs. Additionally, while the model performs well at classifying species into these two broad categories, we observed that it performs poorly if the task is identifying detailed habitat information. We noticed it can generate false results interspersed with true results which are difficult to distinguish. This is currently a common drawback of generative models in all areas of natural language processing, referred to as model "hallucination". Thus, although we provide the model's combined outputs under "davinci_combined" column for each species, we suggest readers perform independent search for obtaining more detailed habitat information.

Having benchmarked the Davinci model against this prompt, we then applied the model to the dataset of 1500+ species. To ensure high-confidence classifications, we set this filter to 0 (0=keep) if for a given species, all three Davinci outputs independently state that the species has been found previously in the human body. The filter is otherwise set to 1 (1=remove). We found that ~100 species met this criterion. The full dataset with Davinci model outputs is provided as (**SI Table 18**). Imposing this filter, we arrived at ~3K unique hits, ~300 species, and ~200 genera from the three biomes of interest. These hits originated from ~500 cell-containing (~300 of which have cell type annotation) and ~2K empty droplets.

Impact of filters on the Tabula Sapiens Microbiome dataset

The TSM dataset consisting of significant hits (E-values <10^-5) from viruses, bacteria and fungi is referred to as TSM F0. The TSM dataset that has gone through the first filter will be referred to as the TSM F1, and so on, such that TSM F7 is the version of the dataset that has passed through all seven filters. In addition to droplets with TSM F0 hits, we kept track of droplets (cell-containing or empty) that did not produce any significant hits. The combination of this group of cells and the TSM F0 group of cells is referred to as the TSM F00.

F00: The total number of cell-containing and empty droplets analyzed were ~1.3M and ~156M, respectively.

TSM F0: There were ~724K significant unique hits (counted based on Unique Molecular Identifiers or UMIs) from three biomes spanning bacteria, fungi and viruses with E-values < 10^-5. These hits originated from ~79K cell-containing droplets (~6% of F00 cell-containing droplets) and ~380K empty droplets (~0.2% of F00 empty droplets).

TSM F1: When we excluded all species found in negative control samples, the number of unique hits was reduced to ~63K, or roughly 10% of the F0 hits. Interestingly, the number of species dropped from ~8200 to only ~7100 and the number of genera went down from ~2500 to ~2400. Filter 1 reduced the numbers of cell-containing and empty droplets to ~13K (~16% of F0 cell-containing droplets) and ~44K (~12% of F0 empty droplets), respectively.

TSM F2: The removal of Salter et al. bacterial genera, reduced the number of unique hits, species, and genera to ~52K, ~6200, and ~2300, respectively. It reduced the numbers of cell-containing and empty droplets to ~12K and ~35K.

TSM F3: The removal of putative fungal contaminants previously identified by Narunsky-Haziza *et al.*, reduced the number of species to ~6100. Other numbers remained nearly the same.

TSM F4: The application of the GBC decontamination model, reduced the number of unique hits, species, and genera down to ~41K, ~4700, and ~2200. It lowered the numbers of cell-containing and empty droplets with hits to ~10K and ~28K.

TSM F5: With the application of the gaussian mixture model on the alignments, we arrived at ~13K unique hits, ~2300 species, and ~1100 genera from ~1K cell-containing droplets, and ~11K empty droplets.

TSM F6: Removing bacterial species and genera based on their habitat of origin in the HUE datasets further reduced the number of unique hits, species, and genera down to ~10K, ~1700, and ~900, respectively, originating from 1K cell-containing droplets and 8K empty droplets.

TSM F7: Lastly, removing bacterial, viral and fungal species that were not previously isolated from the human microbiome based on three independent outputs of OpenAI's Davinci model, we arrived at ~3K unique hits, ~300 species, and ~200 genera from the three biomes of interest. These hits originated from ~500 cell-containing (~300 of which have cell type annotation) and ~2K empty droplets.

The exact numbers and fractions of remaining unique hits, species, genera, cell-containing and empty droplets after each filter relative to TSM F0 dataset is shown in **SI Table 13** and **SI Figure 5**. With the imposition of all filters, we arrive at ~0.4% of the unique hits found in the TSM F0 dataset, ~3% of the species and ~5% of the genera. Similar to the percentage of unique hits remaining, the percentage of cell-containing and empty droplets is ~0.7% and ~0.4%, respectively. If we consider the percentage of *total* cell-containing and empty droplets (i.e. compare TSM F7 dataset to the TSM F00 dataset), we see that ~0.04% of cell-containing droplets and ~0.001% of empty droplets remain. Based on these numbers, we can conclude cell-containing droplets are ~40x more likely to harbor microbial reads than empty droplets.

Considering that the starting number of sequences in the TSM dataset was ~70 billion (including human reads) and the final number of unique microbial hits passing through all filters was a few thousand, we conclude that finding high-confidence microbial sequences in human cellular transcriptomes is a search roughly for one in 25 million sequences. Considering the less stringent criteria imposed on the TSM F5 dataset, it is a search for one in 2.5 million sequences. These numbers are a function of various parameters and

filters affecting the recall of our search. Thus, they could be a few orders of magnitude improved with experimental assays designed specifically for capturing microbial transcripts as well as other computational improvements.

Exploring the inter-and-intra donor tissue microbiomes

To explore the inter-and-intra donor tissue microbiomes, we measure the species unique fractions. For example, for donor 2, when we sum the number of species that only appear in one tissue and divide by the total number of species identified in that donor, we arrive at the unique species fraction equal to 0.53. The average intra-donor unique fraction is 0.64 and the average inter-donor unique fraction, calculated for one tissue across multiple donors, is 0.76 (**SI Figure 17**). The personal nature of human tissue microbiomes, at least in part, likely reflects the highly individual-specific microbiomes that exist at external-facing microbiomes[115–117]. As we also demonstrate through the overlap between species from different isolation sites in the HMP database, external-facing microbiomes have limited overlap at the species level **(SI Figure 22)**. Moreover, as we reduce the taxonomic resolution from species to orders and phyla, the correlations between and within individuals increase considerably (**SI Figures 18-19**), suggesting that high-level tissue microbiome compositions are largely conserved.

Single-droplet statistics, outlier cells and outlier cell types

In the population of hit-positive TSM F7 cells, cells with one unique hit dominate the distribution. The median number of uhits/cell is 1, the mean is ~1.5 and the standard deviation is 8. See **SI Table 23** for statistics on cell-containing and empty droplets from TSM F7 dataset. We define outlier cells by those with uhits/cell > 1.5xIQR, where IQR is the interquartile range for the uhits/cell distribution. The outlier cells are shown in **SI Table 24**. The most prevalent species in outlier cells was EBV. It appeared in outlier cells almost exclusively from donor 2 (TSP2), with the exception of one cell from the Salivary gland of TSP7. TSP2 outlier cells positive for EBV hits consisted of bladder B cells, Lymph node Plasma cells and B cells, among others. In addition to EBV in TSP2, we found a bladder macrophage containing hits from *Ureaplasma urealyticum*[118], which is a commensal organism of the urogenital tract and associated with premature birth and adverse pregnancy outcomes. We found hits to *Aggregatibacter aphrophilus*[119], an oral bacteria associated with periodontal disease and endocarditis, in an adventitial cell of the salivary gland in TSP7.

Six out of eight cell types associated with outlier cells were immune cells, namely Plasma cell, B cell, Natural Killer cell, Macrophage, Memory B cell, and CD34+ CD38- Multipotent

T cell. Interestingly, 72% of outlier cells had viral hits (exclusively EBV) compared to only 7% of empty droplets (**SI Table 25**). Nearly one quarter of outlier cells had bacterial hits compared to ~83% of outlier empty droplets. Fungal hits appeared in only a small fraction of outlier cells and droplets. These numbers support the hypothesis that bacterial and fungal hits mostly come from extracellular spaces and are co-localized with cells or passively uptaken, whereas in cases of intracellular pathogens such as EBV, one might expect a higher number of positive cells and a higher number of unique hits per cell. We found five cells that harbored unique hits from more than one species, primarily bacteria from different orders and phyla in a single cell.

We grouped cells with TSM F7 hits by their cell type, and through dividing the number of F7 hit-positive cells by the total number of cells, we measured the fraction of hit-positive cells for each cell type. To have sufficient numbers for statistical analysis, we chose only cell types with a minimum of 10 cells that were sequenced and annotated. The mean and standard deviation of the fraction of cells in each cell type positive for F7 hits were ~0.0006 and ~0.0015%, respectively. We identified outlier cell types as those that have a higher fraction of F7 positive cells than 1.5xIQR. There were 195 cell types that were included in the analysis, from which 36 were identified as outlier cell types (**SI table 26**). Among the outliers, ~60% of cell types belonged to the immune compartment. Some examples of non-immune outlier cell types are lung alveolar epithelial cells, lung ciliated cells, intestinal transient amplifying cells, vascular and lymph endothelial cells.

SI Figures

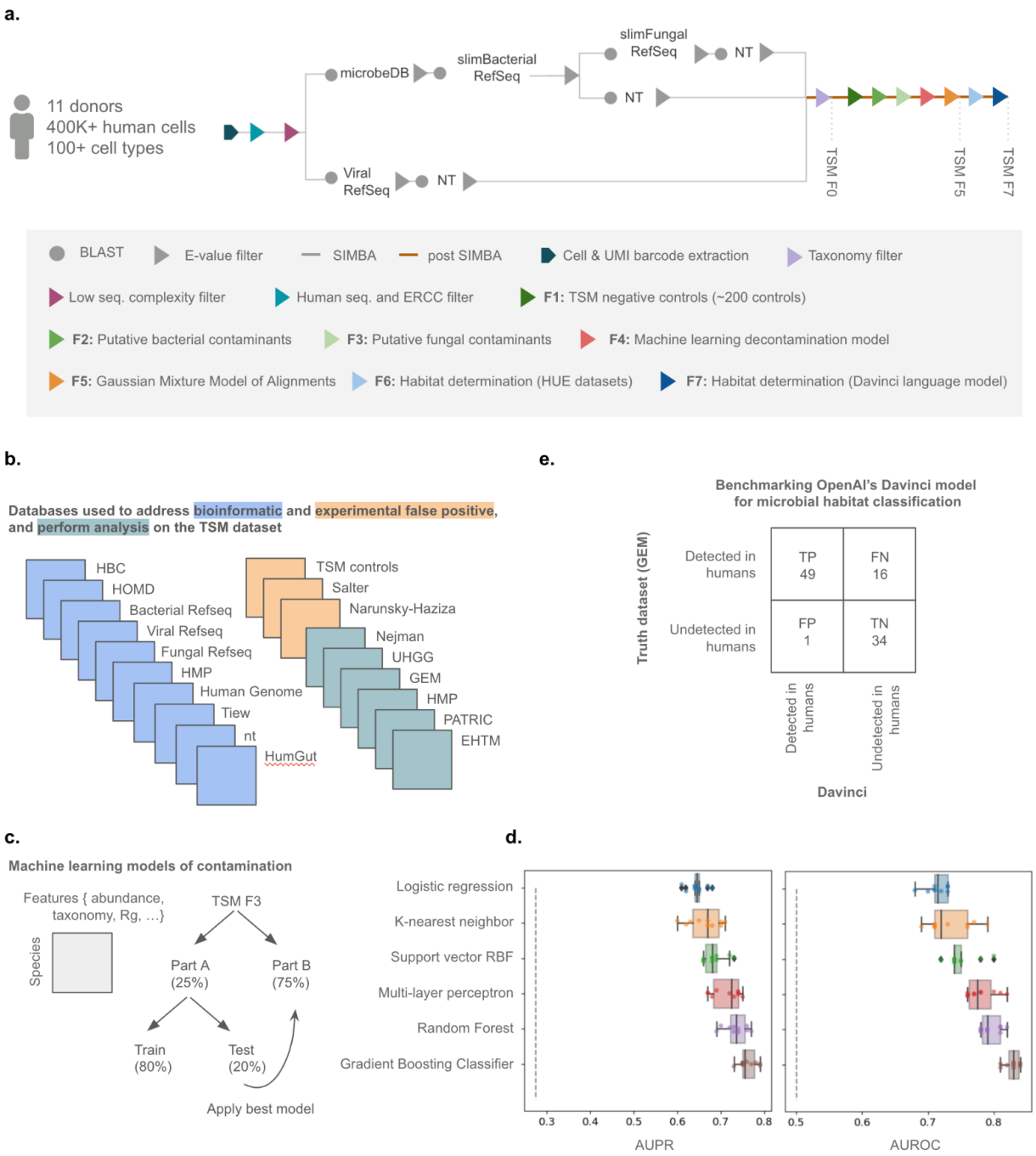

SI Figure 1. Computational pipeline and post-processing steps developed for the identification of high-confidence bacterial, viral and fungal sequences in human single-cell data. **a)** The computational steps comprising SIMBA and post SIMBA filtration of the Tabula Sapiens Microbiome (TSM) dataset. **b)** Databases used to mitigate and benchmark bioinformatic false positives (blue) and experimental false positives (orange), as well as those used for microbial flow and other analyses (green). HBC: Human

Gastrointestinal Bacteria Culture Collection, HOMD: Human Oral Microbiome Dataset, Tiew *et al.* (gut mycobiome), HMP: Human Microbiome Project, nt, Bacterial, Fungal and Viral Refseq datasets (all publically available from NCBI), TSM controls (~200 instrument and reagent negative controls), Salter *et al.* (bacterial genera previously found in prior sequencing studies), Narunsky-Haziza *et al.* (fungal contaminants seen in human tumor samples), Nejman *et al.* (bacterial taxa previously seen in human tumor samples), UHGG (Unified Human Gastrointestinal Genome collection), GEM (Genomes from Earth's Microbiomes), PATRIC (the Pathosystems Resource Integration Center), and EHTM (Extracted Human Tissue Microbiome). **c)** The process by which we used known and putative contaminants to identify additional putative contaminants in the TSM dataset using 6 different types of machine learning models. **d)** Performance metrics of each machine learning model type on withheld test data. For each model type, 10 different models using different train/test splits were created and AUPR and AUROC scores were measured. Dashed lines correspond to null model performance (0.5 for AUROC and the prevalence of the positive class for AUPR). **e)** Confusion matrix for benchmarking the Davinci large language model for microbial habitat classification against the GEM dataset using 100 randomly selected species (Precision = 98%, Recall = 75%). Species are categorized into two groups: 1) found in the human body 2) found anywhere else but the human body. TP: True Positive, FP: False Positive, FN: False Negative, TN: True Negative.

a.

	category	classified fraction
0	superkingdom	0.54
1	phylum	0.52
2	class	0.50
3	order	0.48
4	family	0.44
5	genus	0.38
6	species	0.38

b.

Eukaryota	284988
Bacteria	2669
Viruses	1078
Archaea	94

3 batches of 100 input seqs from each domain

BLASTn | nt

SI Figure 2. Kraken2 (against nt) classification assignments for a Tabula Sapiens Microbiome sample (Bladder, TSP2). **a)** Fraction of classified input sequences by Kraken2 at different taxonomic levels. **b)** Number of classified sequences that were assigned to each domain.

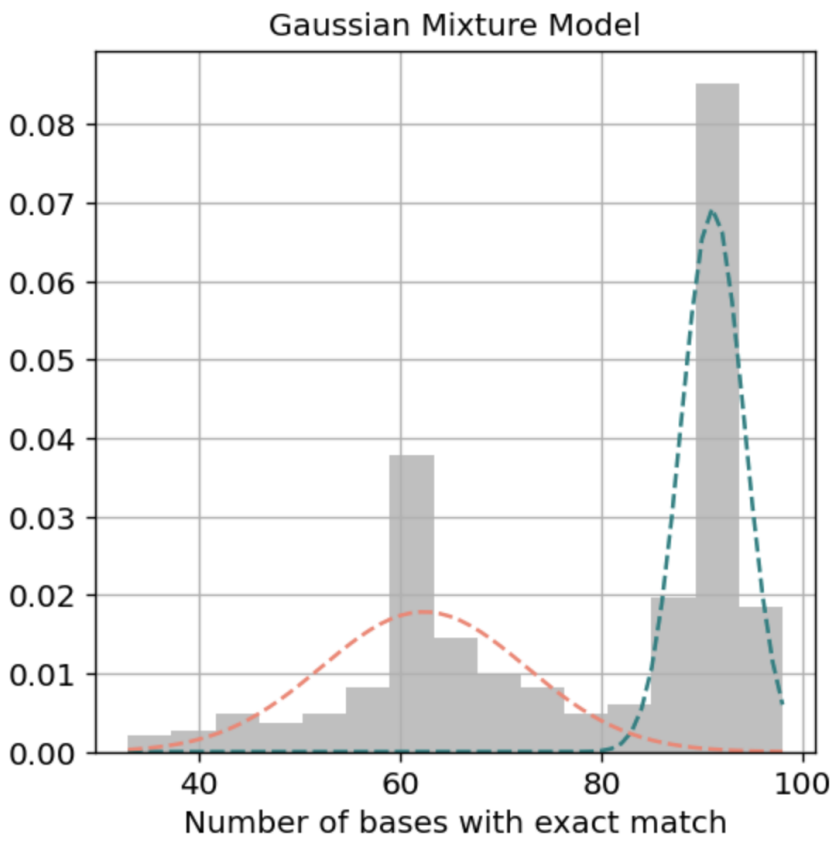

SI Figure 3. Number of bases with exact match to a reference sequence in the nt database (n_match). The Gaussian Mixture model is superimposed on the distribution of n_match (mean or μ_1= 62 bases for first distribution, and μ_2= 91 bases for the second distribution shown in green).

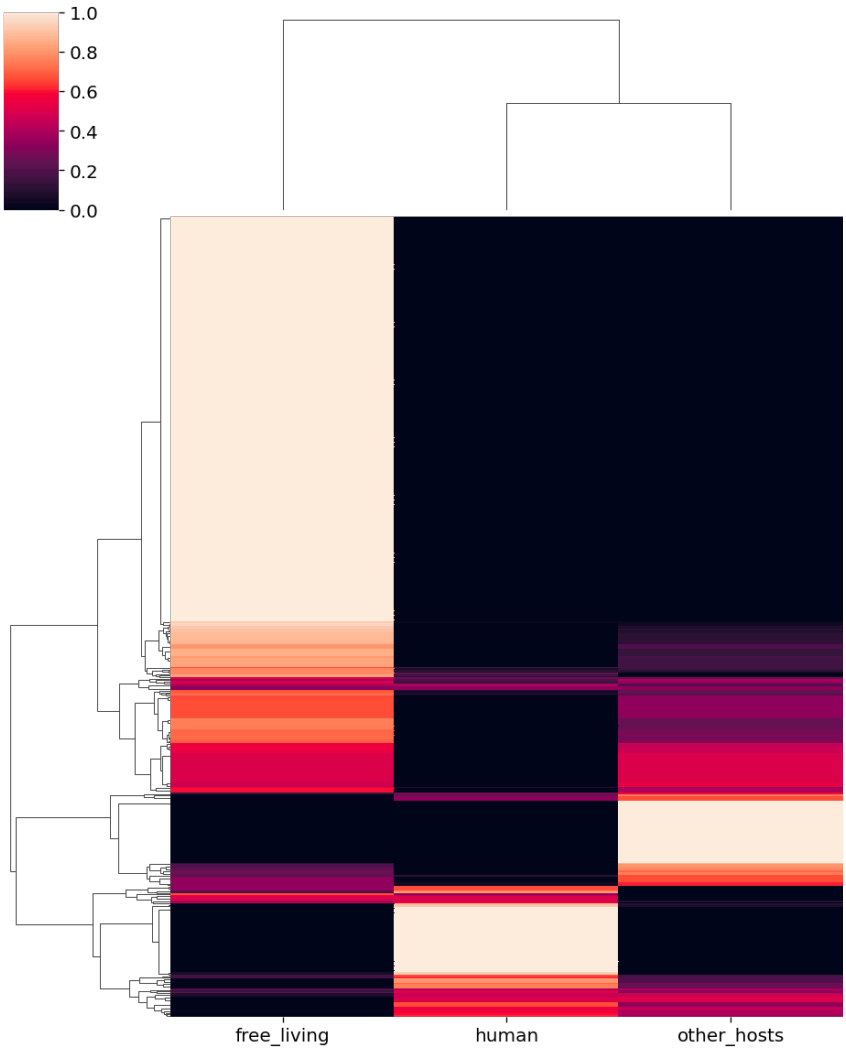

SI Figure 4. Clustering of bacterial genera based on the fraction of their species belonging to three course-grained labels: free-living (e.g. aquatic, terrestrial), human-dwelling (e.g. gi tract, skin), and other hosts (e.g. plants, insects). Each row represents a bacterial genus from the TSM dataset that also appears in the GEM dataset.

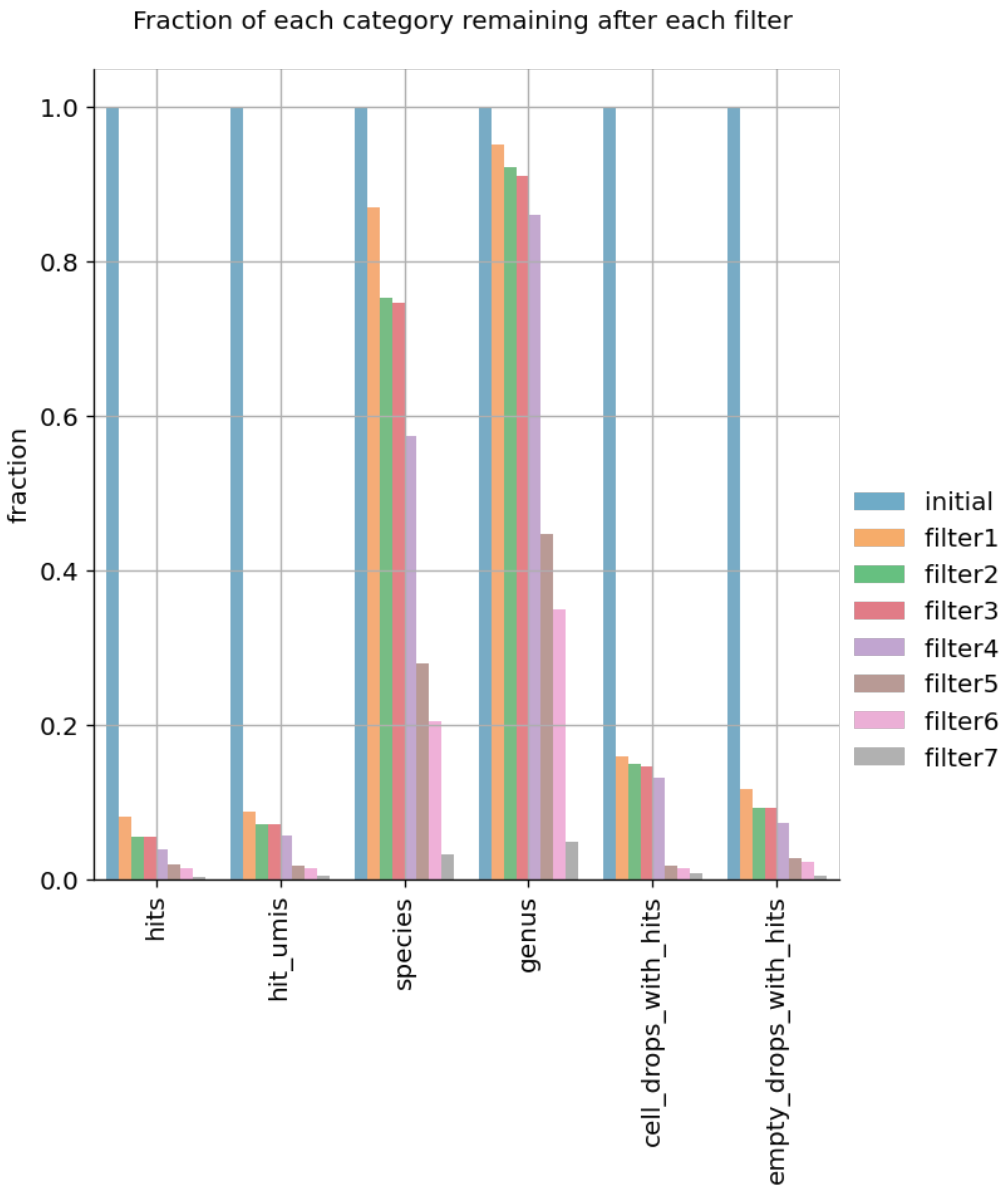

SI Figure 5. Fraction of total microbial hits, unique hits (based on UMIs), species, genera, cell-containing droplets with hits, and empty droplets with hits remaining after each filter is applied. Filter 1: ~200 negative instrument and reagent controls, Filter 2: removal of Salter *et al.* genera, Filter 3: removal of putative fungal contaminants identified by Narunsky-Haziza *et al.*, Filter 4: applying the Gradient-boosting machine learning model for decontamination, Filter 5: applying a Gaussian Mixture Model to select species with higher quality alignments, Filter 6: putative habitat determination using HUE datasets and selecting those taxa more likely to be residents of the human microbiome, and Filter 7: putative habitat determination using the Davinci Large Language Model and selecting additional taxa that are likely residents of the human microbiome.

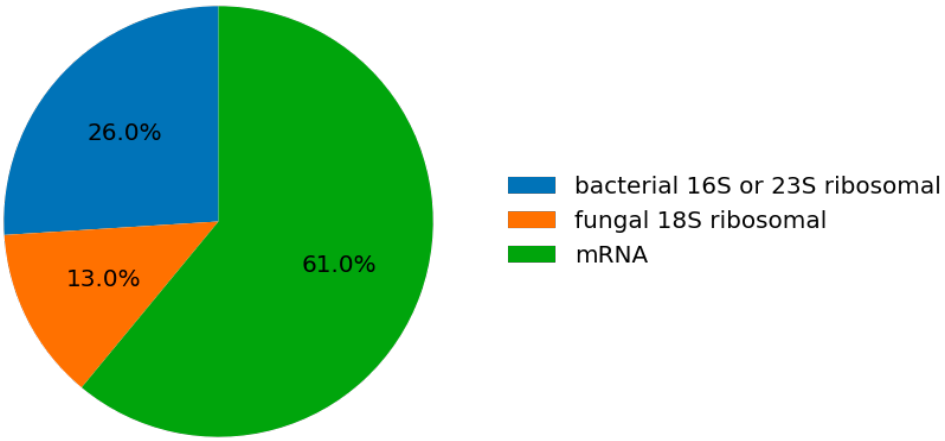

SI Figure 6. Percentage of different types of microbial RNA discovered in the TSM F7 dataset.

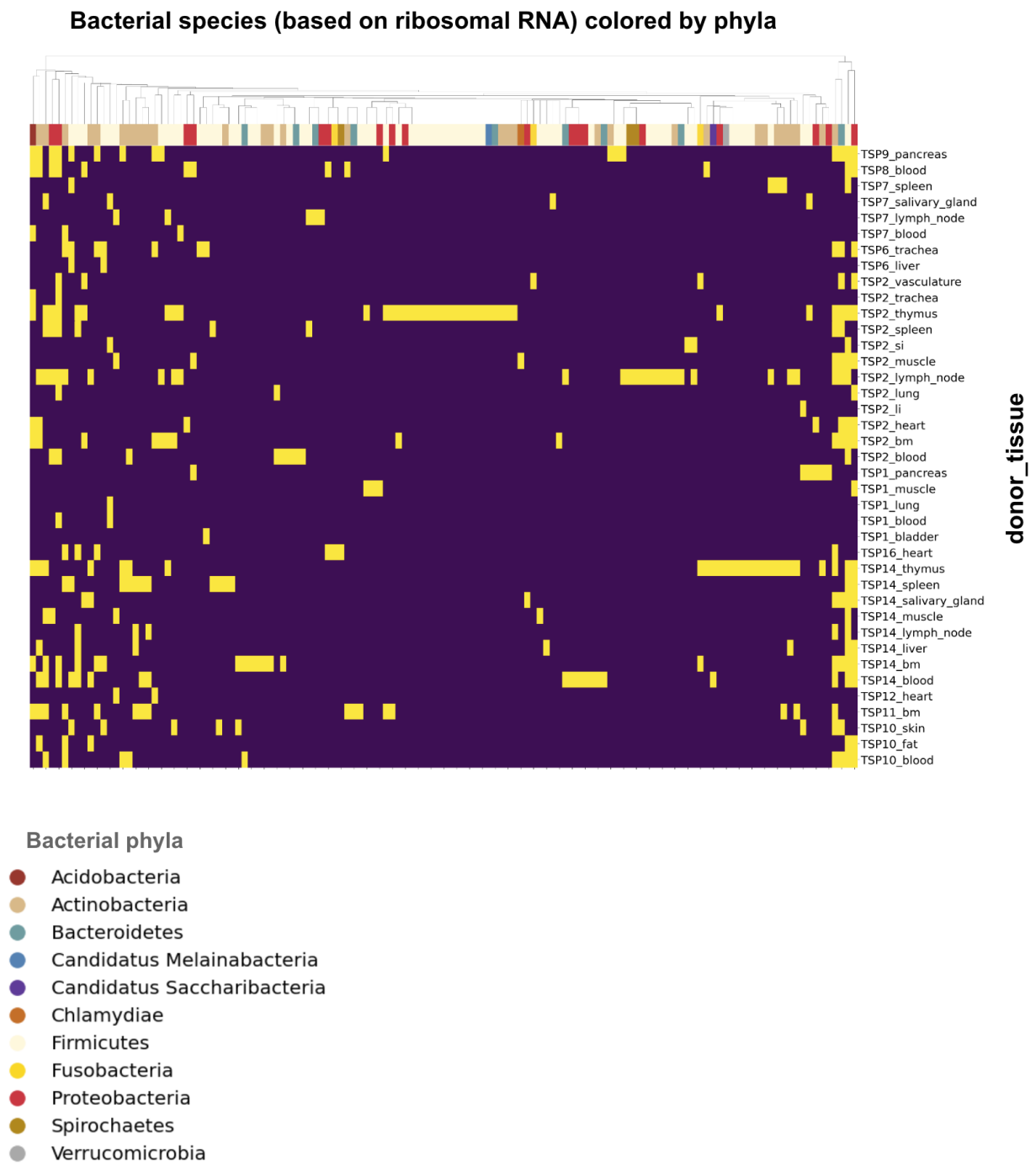

SI Figure 7. Ribosomal RNA from different bacterial phyla across various tissue types. Clustered heatmap of ribosomal hits (presence/yellow and absence/blue is shown) found in each donor's tissue sample. Bacterial species are color-coded based on their phylum-level classification. bm: bone marrow, li: large intestine, si: small intestine.

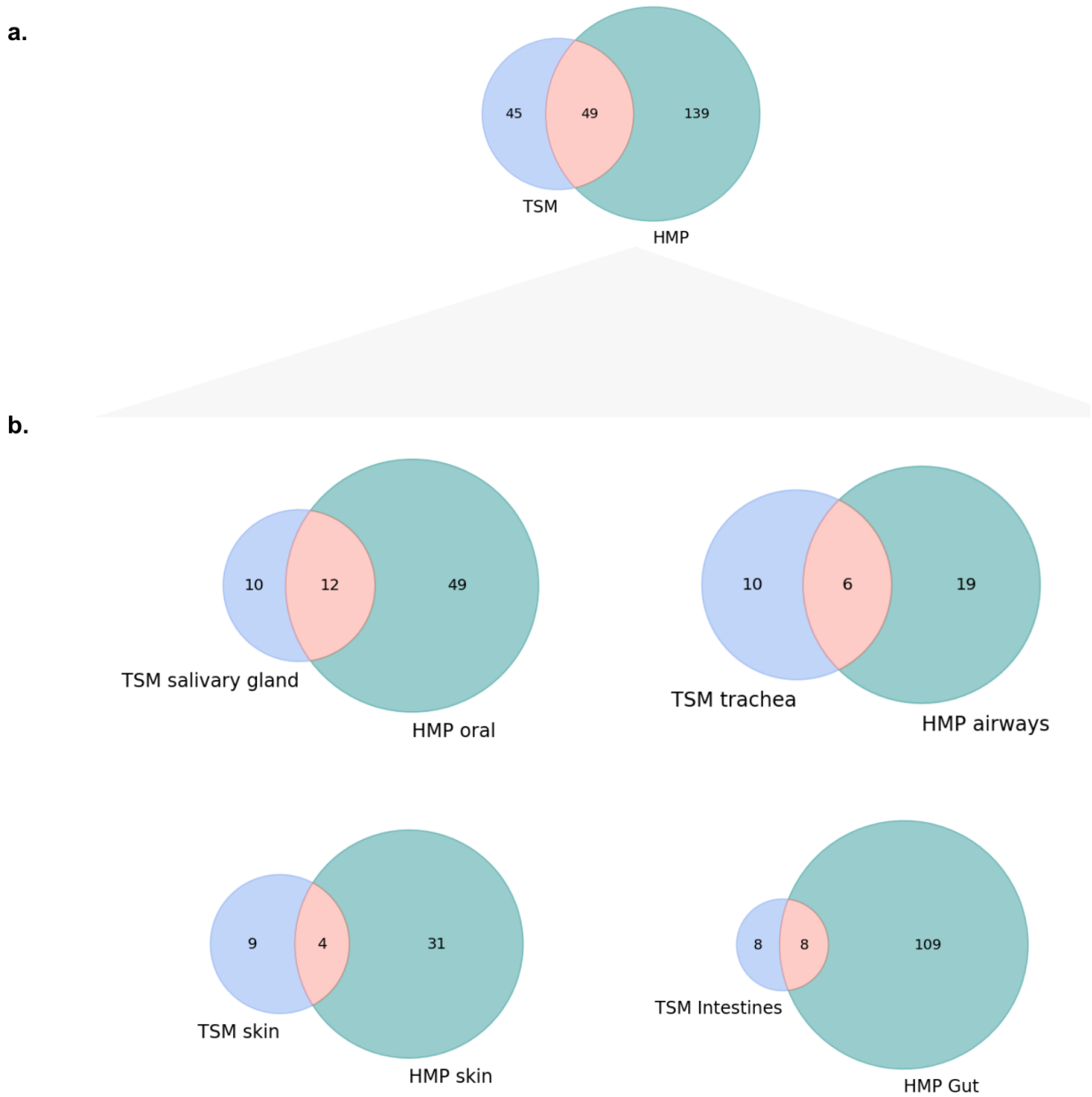

SI Figure 8. Comparisons between the Tabula Sapiens Microbiome (TSM F7) dataset and the Human Microbiome Project (HMP). a) Number of bacterial genera shared between TSM F7 and HMP, b) broken down by HMP isolation sites and their closest tissue counterpart in the TSM dataset. We exclude any members of either dataset that do not have a taxonomic assignment at the genus level in this comparison. TSM intestines refers to both the small and the large intestine samples.

Tissue microbiomes
(TSM F7)
External-facing
microbiomes (HMP)
Bacterial species
Actinomyces graevenitzii
Aggregatibacter actinomycetemcomitans
Aggregatibacter aphrophilus
Aggregatibacter sp.
Alistipes shahii
Bacteroides uniformis
Blautia sp.
Campylobacter showae
Campylobacter upsaliensis
Campylobacter ureolyticus
Capnocytophaga gingivalis
Capnocytophaga sp.
Cardiobacterium valvarum
Coprococcus catus
Coprococcus comes
Corynebacterium accolens
Corynebacterium ammoniagenes
Corynebacterium lipophiloflavum
Corynebacterium sp.
Desulfitobacterium hafniense
Dialister pneumosintes
Erysipelothrix rhusiopathiae
Filifactor alocis
Flavonifractor plautii
Globicatella sp.
Granulicatella adiacens
Kytococcus sp.
Lachnoanaerobaculum sp.
Lactobacillus vaginalis
Neisseria sp.
Oribacterium sp.
Paraprevotella xylaniphila
Parvimonas micra
Pasteurella dagmatis
Peptoniphilus sp.
Porphyromonas asaccharolytica
Porphyromonas gingivalis
Porphyromonas sp.
Prevotella denticola
Rothia sp.
Segniliparus rugosus
Selenomonas artemidis
Selenomonas infelix
Selenomonas sputigena
Slackia exigua
Streptococcus constellatus
Streptococcus vestibularis
Treponema denticola
Treponema vincentii
Veillonella atypica
Veillonella sp.
blood
bm
fat
heart
kidney
liver
lung
lymph_node
muscle
pancreas
salivary_gland
si
skin
spleen
thymus
trachea
vasculature
airways
ear
gastrointestinal_tract
oral
skin_hmp
urogenital_tract

1549

SI Figure 9. Bacterial species found in both the TSM F7 dataset and the Human Microbiome project (HMP). Presence is denoted by the light colored boxes. Boxed in red are species that were referred to in the main text. bm: bone marrow, li: large intestine, si: small intestine.

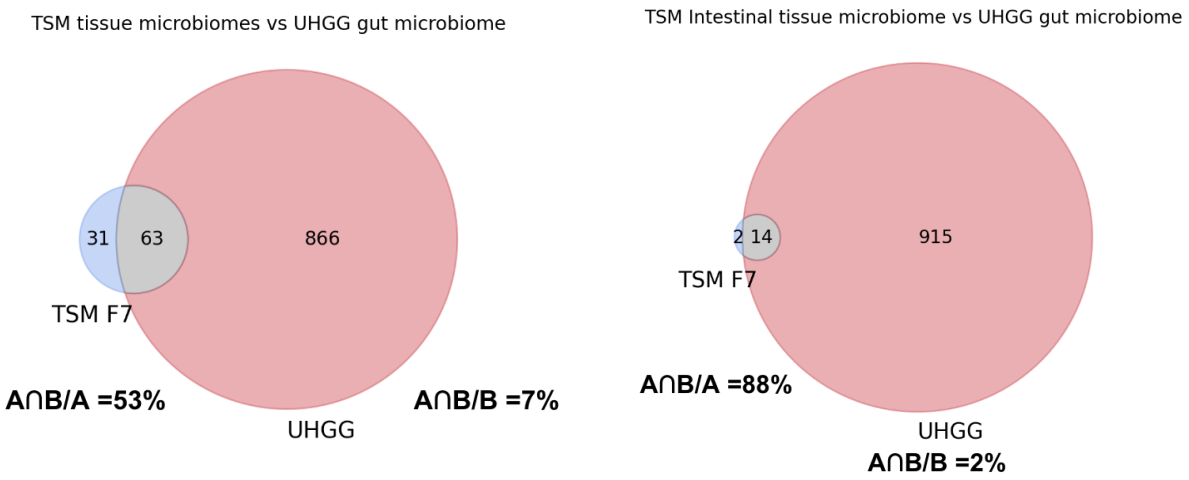

SI Figure 10. Comparisons between the Tabula Sapiens Microbiome (TSM f7) and the Unified Human Gastrointestinal Genome (UHGG) collection datasets. left) Number of bacterial genera shared between TSM F7 tissue microbiomes and UHGG. right) Number of bacterial genera shared between TSM F7 intestinal tissue microbiomes (both large and small intestines) and UHGG. We treat TSM datasets as set A and UHGG as set B.

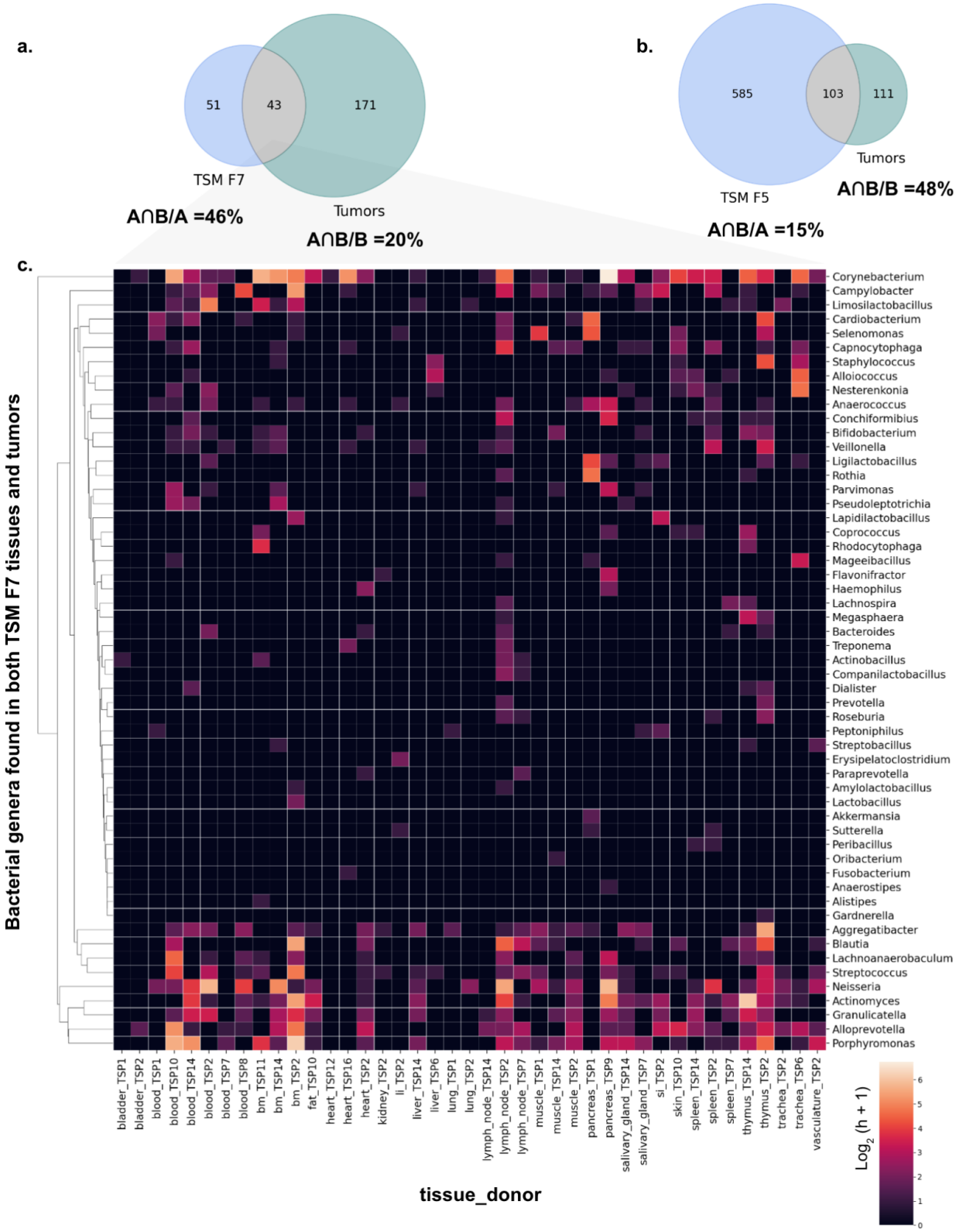

SI Figure 11. Exploring the intersection of bacterial genera found in the Tabula Sapiens Microbiome (TSM) a) F7 or b) F5 datasets and tumor microbiomes from Nejman *et al.*

(only species and orders appearing in tumors that passed all of this study's contamination filters were selected for analysis, refer to this study's Table S4). The percentage of shared genera compared to total number of genera in each dataset are shown (set A corresponds to TSM datasets, and set B corresponds to the Nejman *et al.* dataset). c) abundance of bacterial genera shared between the TSM F7 stratified by tissue and donor of origin and Nejman *et al.* datasets. Abundance of genera is based on Log_2(hits +1). Entries with unknown genera are excluded from comparisons shown in the venn diagrams. bm: bone marrow, li: large intestine, si: small intestine.

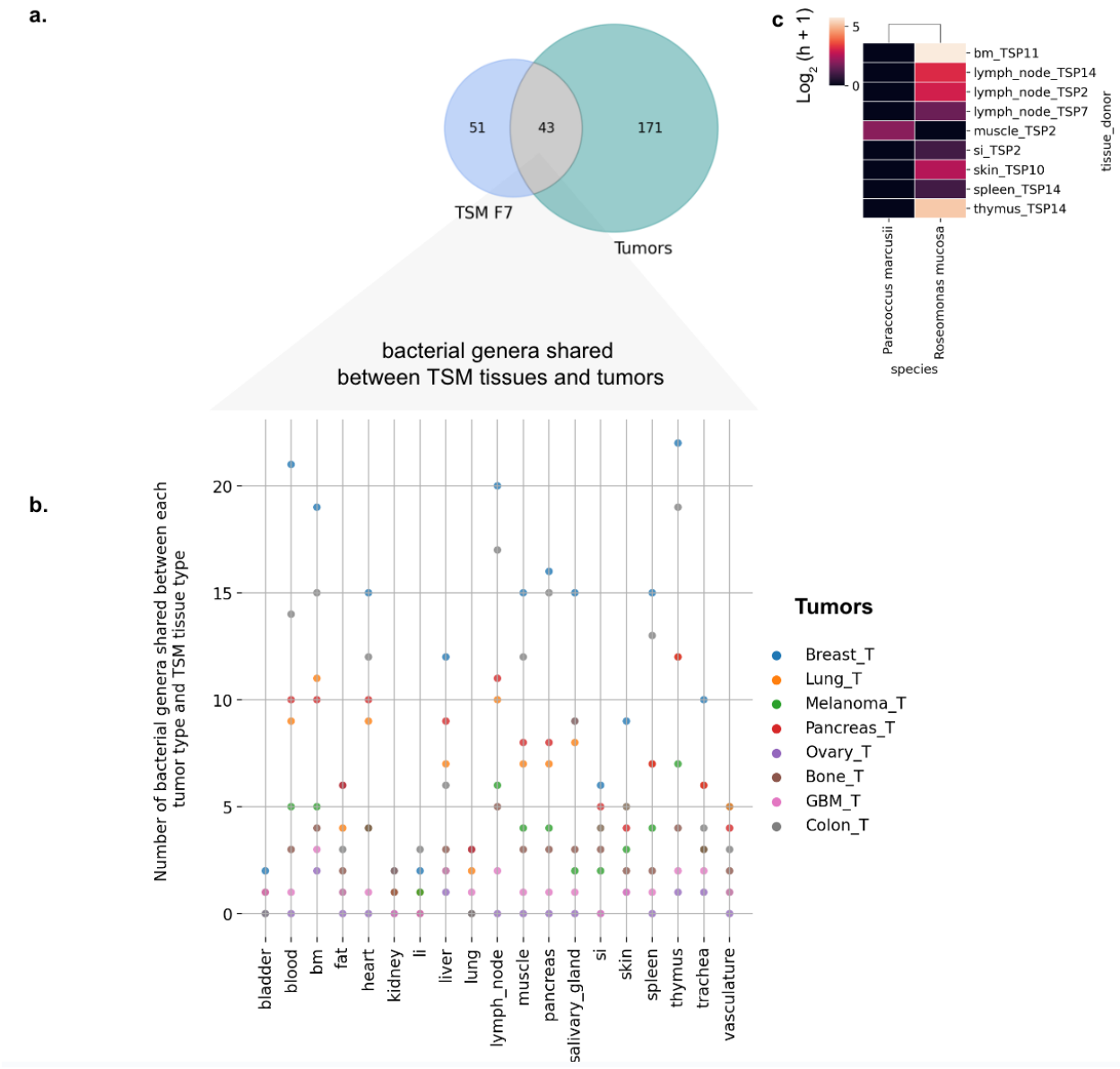

1575 **SI Figure 12.** Comparison of bacterial genera in healthy tissues from TSM F7 and tumors
1576 from Nejman *et al.* (Only genera appearing in tumors that passed all of this study's
1577 contamination filters were selected for analysis from Nejman *et al*. Table S4, and from
1578 their Figure 4D for tumor enriched species). a) venn-diagram representing the number of
1579 shared genera between the two datasets. b) Number of bacterial genera shared between
1580 each tumor type and each TSM F7 tissue type is shown. bm: bone marrow, li: large
1581 intestine, si: small intestine, GBM: glioblastoma multiforme. c) abundance of species that
1582 were highly enriched in tumors and also appeared in the TSM F5 dataset. Abundance of
1583 species is based on Log_2 hits +1.

1584

Log2 (h + 1)
7
6
5
4
3
2
1
0
Tissues (TSM)
Tumors
(Nejman et al.)
bladder
blood
bm
fat
heart
kidney
li
liver
lung
lymph_node
muscle
pancreas
salivary_gland
si
skin
spleen
thymus
trachea
vasculature
Breast_T
Lung_T
Melanoma_T
Pancreas_T
Ovary_T
Bone_T
GBM_T
Colon_T
Brachybacterium
Capnocytophaga
Cellulomonas
Myroides
Selenomonas
Anaerococcus
Conchiformibius
Cardiobacterium
Lachnoanaerobaculum
Staphylococcus
Rubellimicrobium
Mycobacterium
Williamsia
Pseudoalteromonas
Alloiococcus
Salinicoccus
Cloacibacterium
Nesterenkonia
Shewanella
Bifidobacterium
Enterococcus
Veillonella
Bacteroides
Clostridium
Coprococcus
Lachnospira
Roseburia
Desulfovibrio
Megasphaera
Parabacteroides
Alistipes
Dialister
Lactobacillus
Prevotella
Agromyces
Hydrogenophilus
Agrobacterium
Halomonas
Rothia
Klebsiella
Noviherbaspirillum
Treponema
Achromobacter
Haemophilus
Barnesiella
Oscillibacter
Sutterella
Flavonifractor
Oribacterium
Akkermansia
Anaerostipes
Actinobacillus
Fusobacterium
Peptoniphilus
Xanthobacter
Gordonia
Rickettsia
Adhaeribacter
Citrobacter
Geobacillus
Aeromonas
Lactococcus
Solibacillus
Rhodobacter
Jeotgalicoccus
Gardnerella
Rheinheimera
Lysobacter
Rubrivivax
Leuconostoc
Pantoea
Parvimonas
Actinoplanes
Skermanella
Azospirillum
Sphingobacterium
Alishewanella
Belnapia
Rhodocytophaga
Propionibacterium
Hymenobacter
Ornithinimicrobium
Friedmanniella
Blastococcus
Luteimonas
Gluconacetobacter
Altererythrobacter
Modestobacter
Nocardioides
Blautia
Streptococcus
Neisseria
Porphyromonas
Streptomyces
Aggregatibacter
Bacillus
Acinetobacter
Actinomyces
Campylobacter
Granulicatella
Serratia
Corynebacterium
Pseudomonas
genera

SI Figure 13. Abundance of bacterial genera previously found in tumor samples (Nejman *et. al*, 2020) and in the Tabula Sapiens Microbiome (TSM) F5 dataset stratified by tissue of origin. Abundance is based on $\log_2$(hits +1). Samples with "_T" appended correspond to tumors. bm: bone marrow, li: large intestine, si: small intestine, GBM: glioblastoma multiforme.

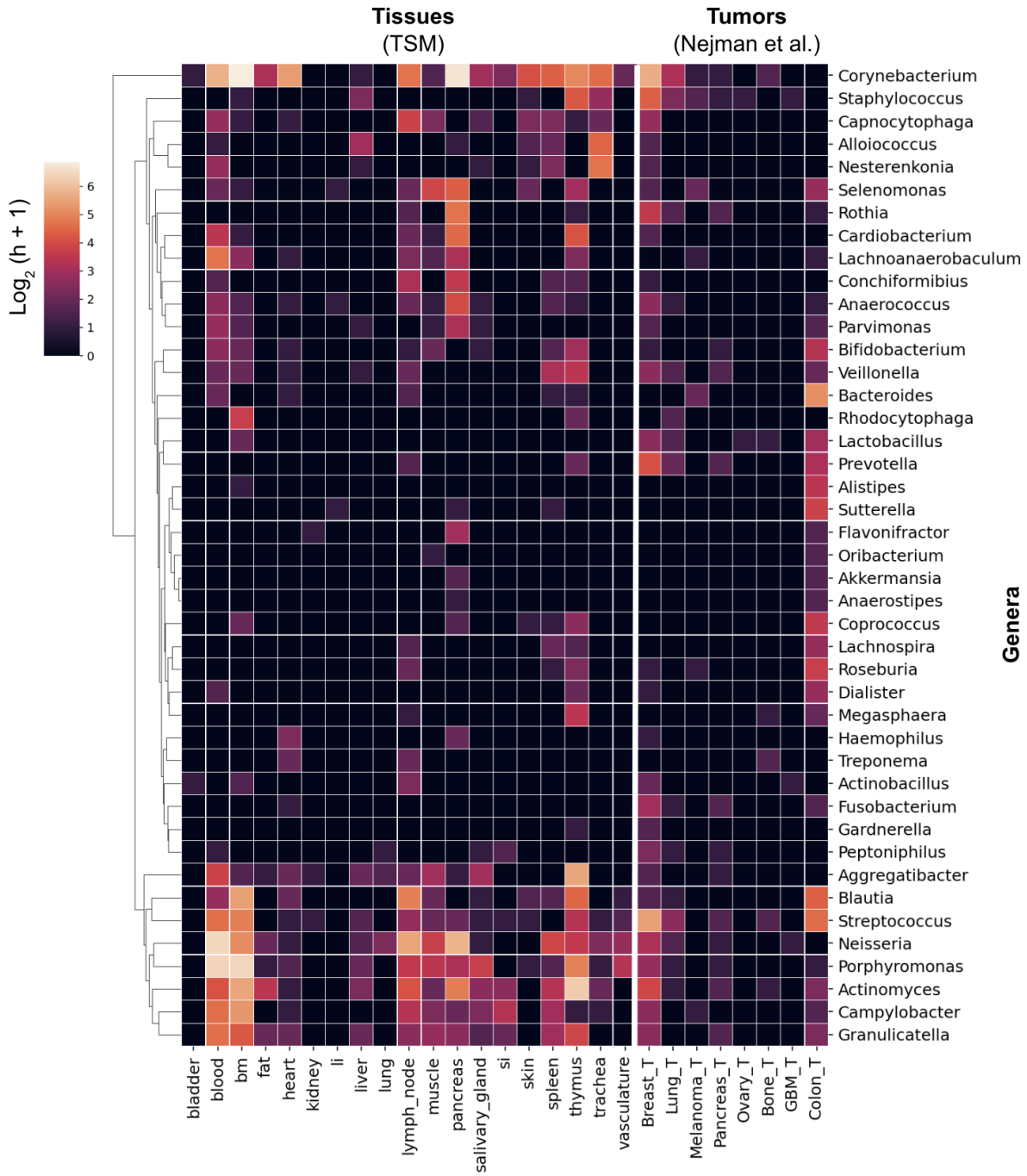

1593 **SI Figure 14.** Abundance of bacterial genera previously found in tumor samples (Nejman
1594 *et. al*, 2020) and in the Tabula Sapiens Microbiome (TSM) F7 dataset stratified by tissue
1595 of origin. Abundance is based on $\log_2$ (hits +1). Samples with "_T" appended correspond
1596 to tumors. bm: bone marrow, li: large intestine, si: small intestine, GBM: glioblastoma
1597 multiforme.

1598

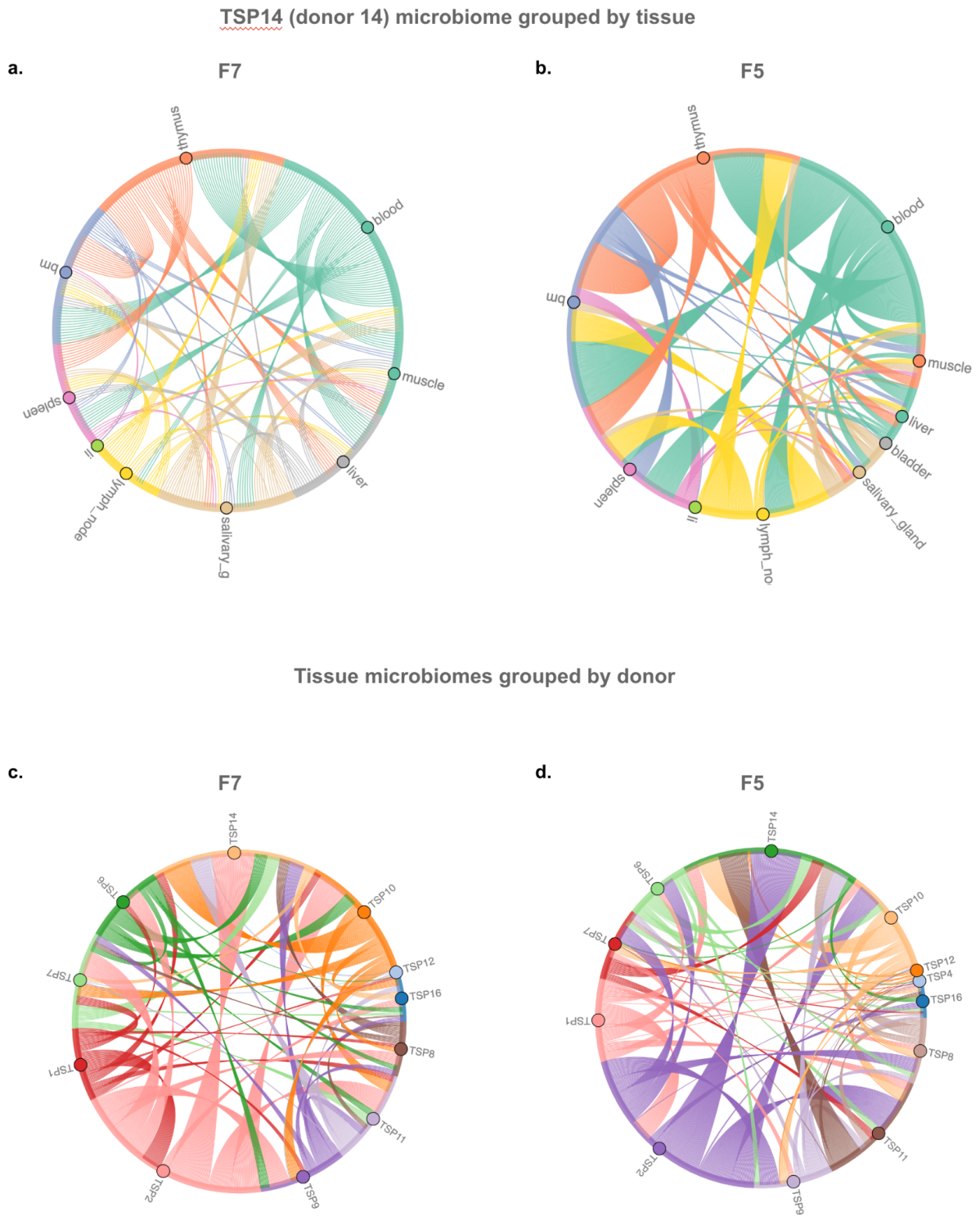

SI Figure 15. Circos plots of shared species within (a,b) and between donors (c,d). Each link represents a unique species. Species that are not shared are not shown. Left panels correspond to TSM F7 and the right panels correspond to TSM F5 datasets.

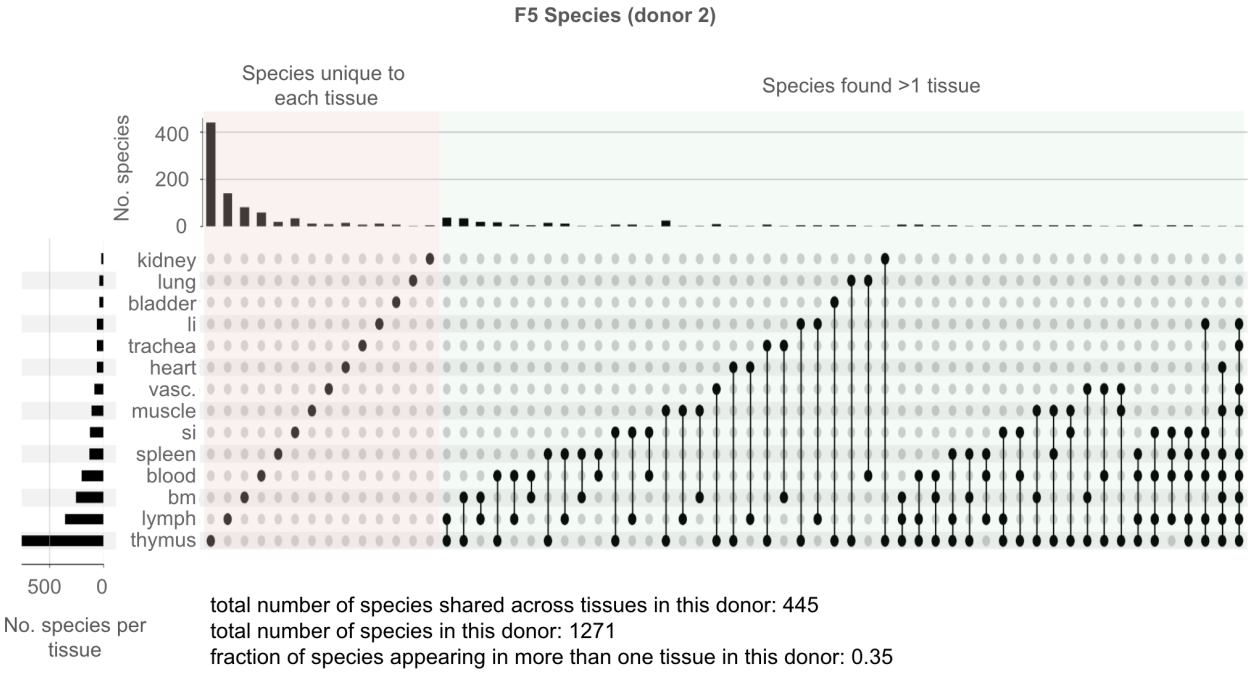

SI Figure 16. UpSet plots for TSP2 (donor 2) TSM F5 species demonstrating the number of shared taxa between tissues, as well as the number of taxa unique to each tissue. Unique sets of species are shown as filled circles. The intersection of two or more sets are shown via connected circles. Bars denote the size of each set or the intersection of sets. For visual clarity, the minimum subset size has been set to 2. bm: bone marrow, li: large intestine, si: small intestine, vasc: vasculature.

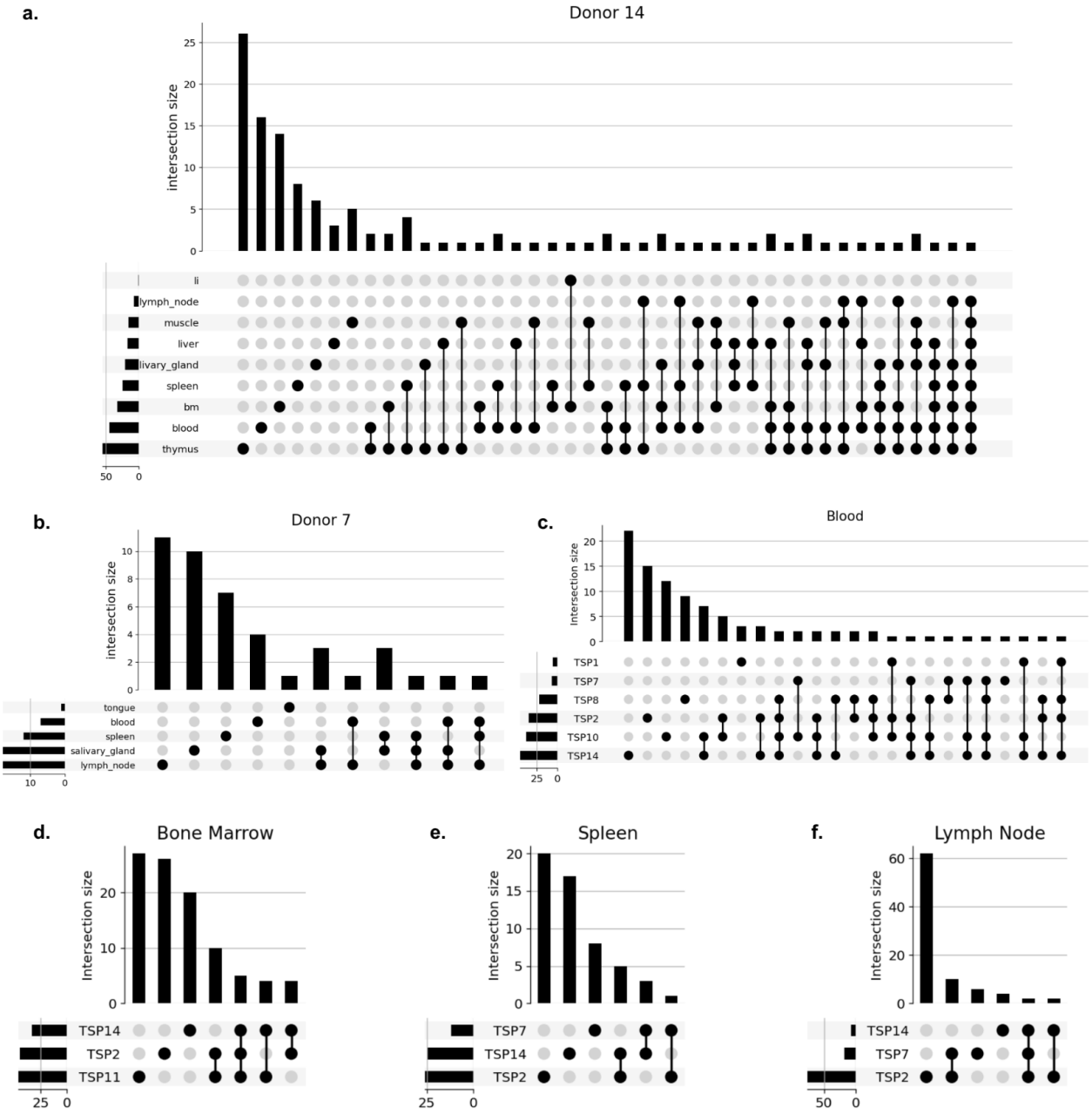

g.

	TSP2	TSP14	TSP7	blood	bone_marrow	spleen	lymph_node
total	176	123	43	98	96	54	86
shared_species	82	45	10	36	23	9	14
unique_fraction	0.53	0.63	0.77	0.63	0.76	0.83	0.84

SI Figure 17. UpSet plots depicting the number of species shared and unique to each sample. Panels a and b depict intra-donor comparisons of tissues, while c-f depict inter-donor comparisons of the same tissue. Unique sets of species are shown as filled circles. The intersection of two or more sets are shown via connected circles. Bars denote the size of each set or the intersection of sets. Panel g summarizes the number and fraction of species that appear in more than one sample within each panel a-f.

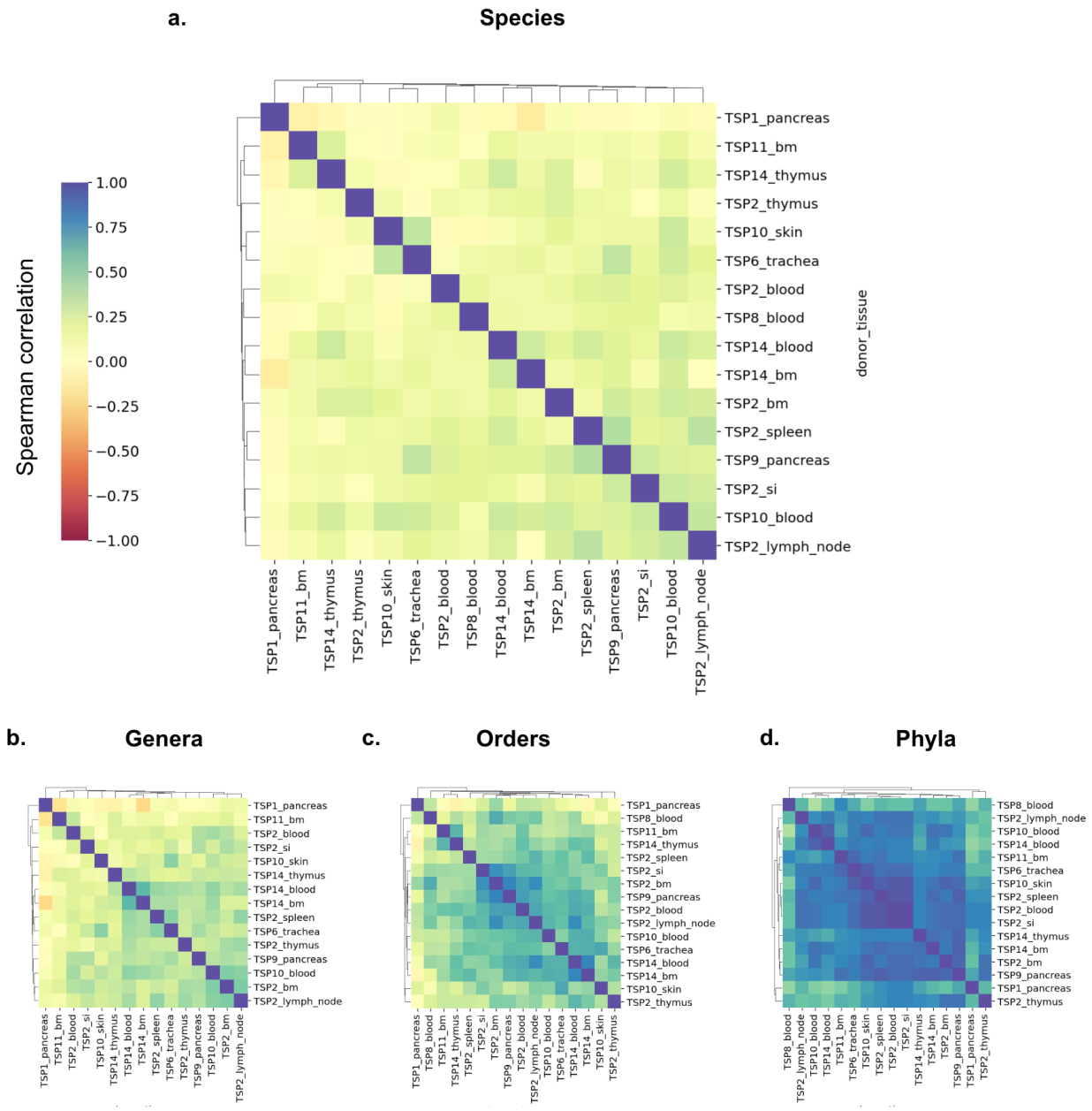

SI Figure 18. Tissue microbiomes across tissues and donors for TSM F7 bacterial dataset at the a) species, b) genera, c) orders and d) phyla-level classification. Pairwise Spearman correlation cluster maps across samples grouped by donor and tissue are shown. Only samples with more than 50 hits are shown.

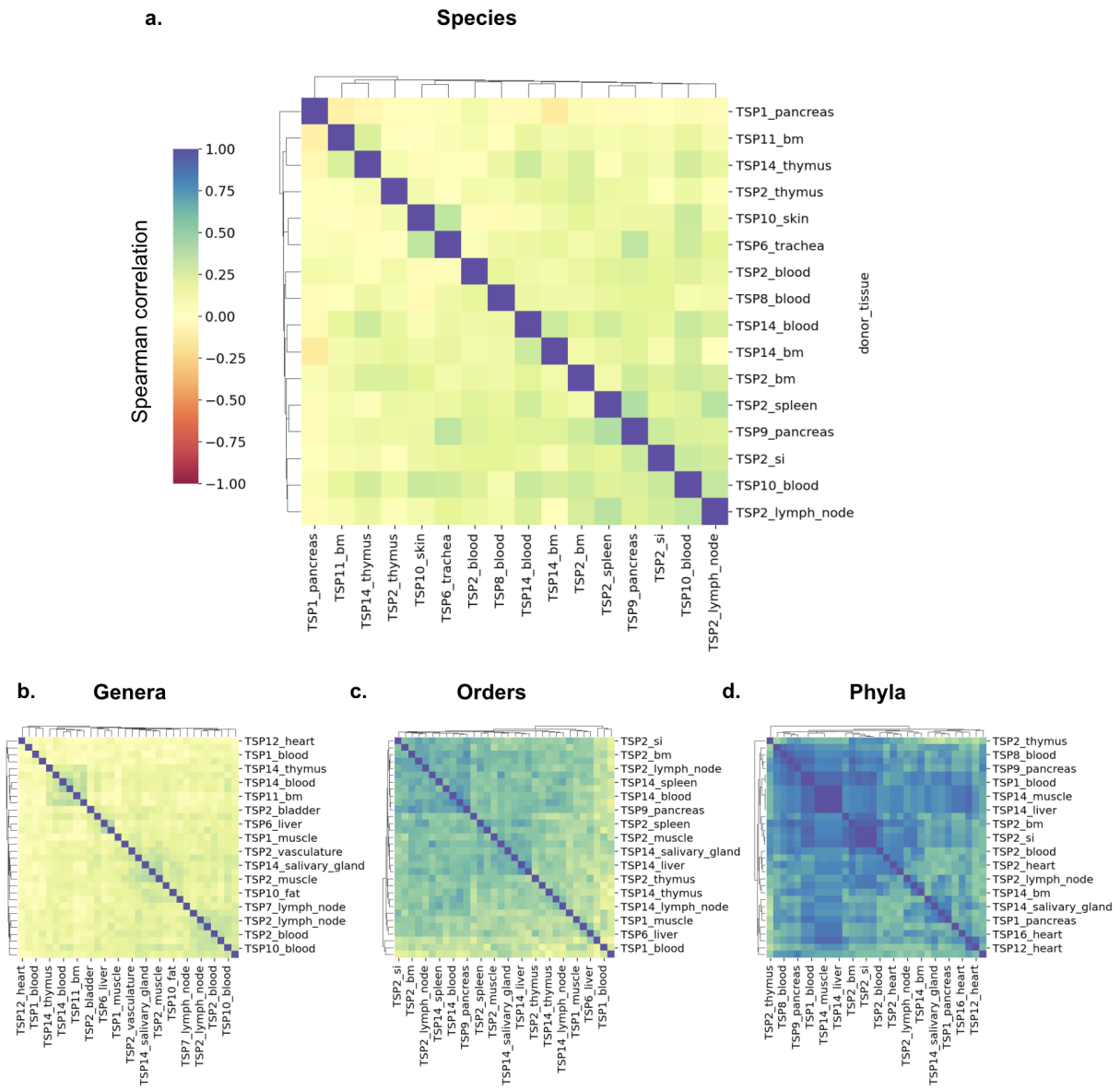

SI Figure 19. Tissue microbiomes across donor_tissue samples for TSM F5 bacterial dataset at the a) species, b) genera, c) orders and d) phyla-level classification. Pairwise Spearman correlation cluster maps across samples grouped by donor and tissue are shown. Only samples with more than 50 hits are shown.

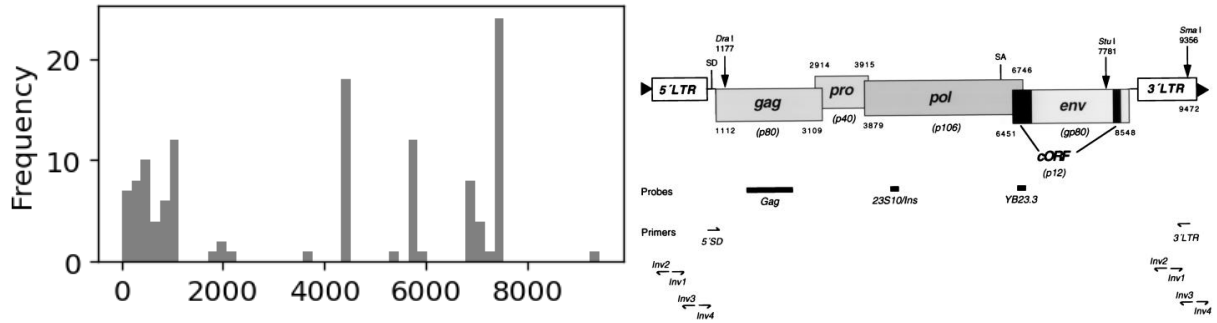

https://pubmed.ncbi.nlm.nih.gov/10516026/

SI Figure 20. The genomic position of identified HERV K hits (left) with respect to the annotated HERV K genome (right) (Tönjes, 1999).

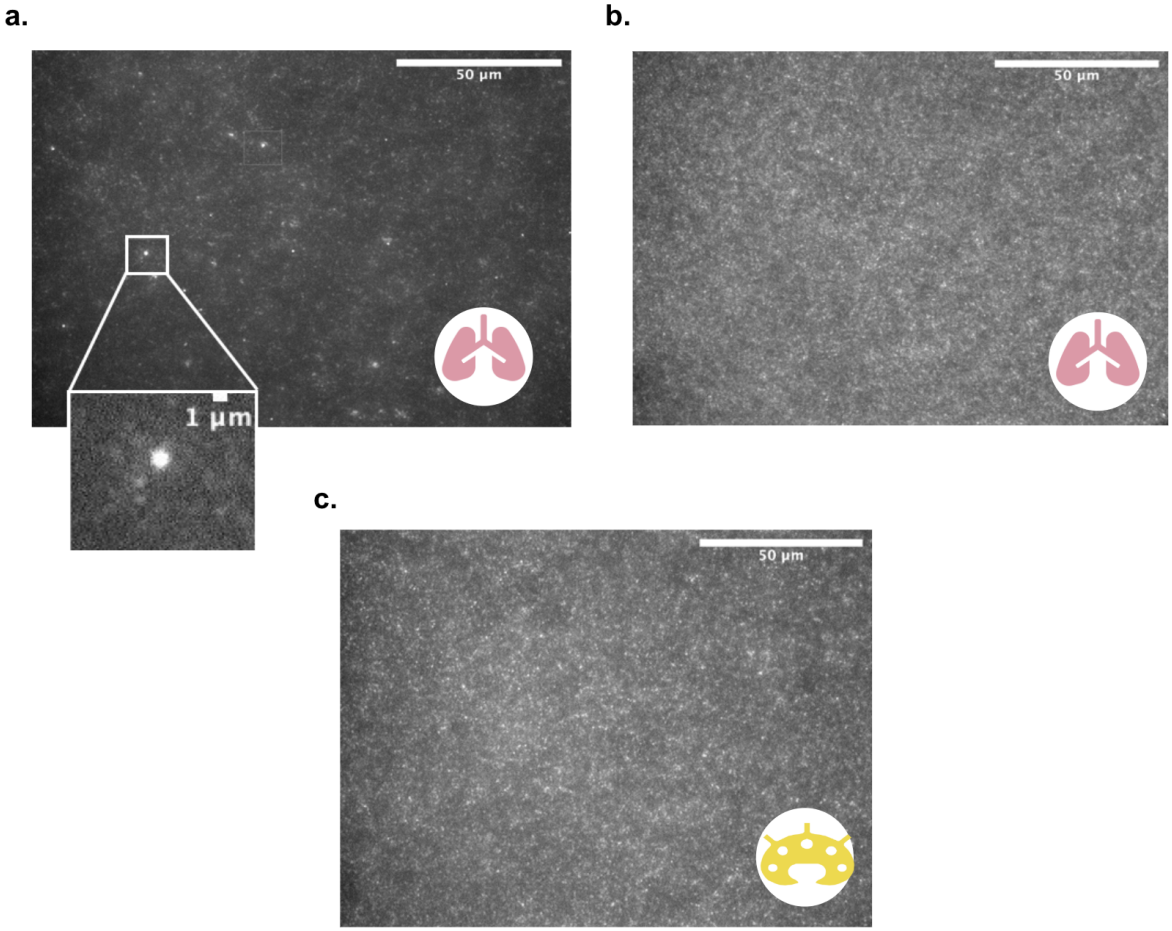

SI Figure 21. Fluorescence staining of donor-derived bacterial-like particles (BLPs) from the lung (a) and Virus-like particles (VLPs) from a lung and a lymph node sample (b,c).

These images were used to estimate VLP and BLP concentrations in a cubic centimeter of tissue (~10^8 VLPs/cm^3 and ~10^7 BLPs/cm^3).

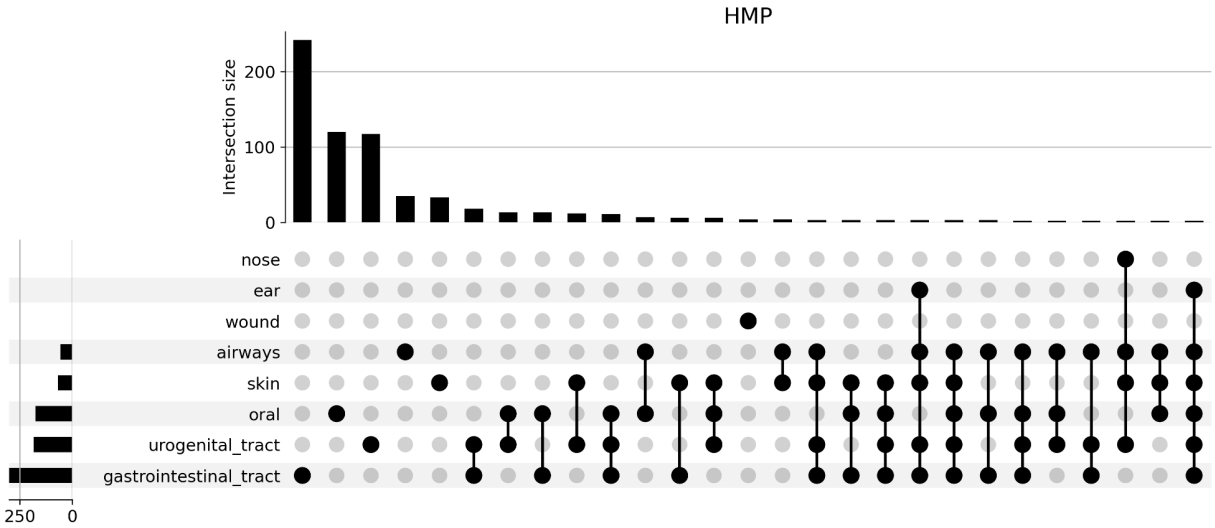

SI Figure 22. UpSet plot showing the taxa shared across different external-facing microbiomes in the Human Microbiome Project (HMP) dataset. Unique sets of taxa are shown as filled circles. The intersection of two or more sets are shown via connected circles. Bars denote the size of each set or the intersection of sets.

SI Tables

SI Table 1. Precision and recall associated with SIMBA using a random selection of 100 viral genomes and 10 sequences per genome as a truth dataset.

	domain	phylum	class	order	family	genus	species
precision	1.0	1.0	1.0	1.0	1.0	0.999	0.809
recall	1.0	1.0	1.0	1.0	1.0	1.000	1.000

SI Table 2. Examples of false positives associated with the viral truth dataset at the species level. “Species_truth” and “species_test” columns correspond to species found in the truth and test datasets, respectively.

	species_truth	species_test
0	Acinetobacter virus AbP2	Acinetobacter phage Bphi-R1888
1	Acinetobacter virus D2	Acinetobacter phage vB_AbaP_APK44
2	Acinetobacter virus D2	Acinetobacter phage vB_AbaP_D2M
3	Acinetobacter virus D2	Acinetobacter phage vB_AbaP_PMK34
4	Arthrobacter virus Piccoletto	Arthrobacter virus Beans
5	Campylobacter virus CP220	Campylobacter phage CP20
6	Campylobacter virus CP220	Campylobacter virus CP21
7	Campylobacter virus CP220	Campylobacter virus IBB35
8	Canna yellow mottle associated virus	Canna yellow mottle virus
9	Escherichia virus VR7	Escherichia virus VR25
10	Escherichia virus VR7	Escherichia virus VR26
11	Leuconostoc virus Lmd1	Leuconostoc virus LN6B
12	Mycobacterium phage ArcherNM	Mycobacterium phage Changeling
13	Mycobacterium phage Phaedrus	Mycobacterium phage Akoma
14	Mycobacterium phage Phaedrus	Mycobacterium phage Compostia
15	Mycobacterium phage Tiffany	Mycobacterium phage Dieselweasel
16	Mycobacterium phage Tiffany	Mycobacterium phage P28Green
17	Mycobacterium phage Tiffany	Mycobacterium phage SoilDragon
18	Mycobacterium phage Tiffany	Mycobacterium virus Bxz2
19	Mycobacterium virus Skinnyp	Mycobacterium phage ShrimpFriedEgg
20	Mycobacterium virus TA17a	Mycobacterium phage Holeinone

SI Table 3. Examples of false positives associated with the viral truth dataset and the corresponding percent identity ("pident_test" column) and the length ("length_test" column) of the alignment between the input seq and output seq. "Species_truth" and "species_test" columns correspond to species found in the truth and test datasets, respectively.

species_truth	species_test	pident_test	length_test
Pseudomonas phage C11	Pseudomonas phage vB_PaeM_SCUT-S2	100.0	100.0
Pseudomonas phage C11	Pseudomonas phage PaZq-1	100.0	100.0
Pseudomonas phage C11	Pseudomonas phage PaGz-1	100.0	100.0
Pseudomonas phage C11	Pseudomonas phage K5	100.0	100.0
Acinetobacter virus AbP2	Acinetobacter phage Bphi-R1888	100.0	100.0
Pseudomonas phage DL54	Pseudomonas phage phiPA01_EW	100.0	100.0
Pseudomonas phage DL54	Pseudomonas virus Pa222	100.0	100.0
Pseudomonas phage DL54	Pseudomonas phage otherone	100.0	100.0
Mycobacterium phage Phaedrus	Mycobacterium phage Akoma	100.0	100.0
Mycobacterium phage Phaedrus	Mycobacterium phage Compostia	100.0	100.0
Mycobacterium virus Skinnyp	Mycobacterium phage ShrimpFriedEgg	100.0	100.0
Salmonella phage SEN5	Salmonella virus SEN4	100.0	100.0
Pseudomonas virus LMA2	Pseudomonas phage PHW2	100.0	100.0
Pseudomonas virus LMA2	Pseudomonas phage willy	100.0	100.0
Pseudomonas virus LMA2	Pseudomonas phage PaGU11	100.0	100.0

SI Table 4. Precision and recall scores using a truth dataset containing 5000 sequences from 50 gut bacterial species (randomly selected sequences and species).

	domain	phylum	class	order	family	genus	species
precision	1.000	0.999	0.997	0.996	0.973	0.947	0.699
recall	0.291	0.291	0.290	0.290	0.285	0.280	0.223

SI Table 5. Species from the truth dataset and their corresponding false label at the level of species classification. First five false positives are shown. “Species_truth” and “species_test” columns correspond to species found in the truth and test datasets, respectively.

species_truth	species_test
Bifidobacterium faecale	Bifidobacterium adolescentis
Enterococcus lactis	Enterococcus faecium
Lacticaseibacillus casei	Lacticaseibacillus zeae
Bacteroides faecis	Bacteroides thetaiotaomicron
Butyricimonas virosa	Butyricimonas faecalis

SI Table 6. Precision and recall scores using a truth dataset containing 5000 sequences from 50 oral bacterial species from the expanded Human Oral Microbiome Database (randomly selected sequences and species).

	domain	phylum	class	order	family	genus	species
precision	1.000	1.000	0.996	0.990	0.987	0.974	0.854
recall	0.209	0.209	0.208	0.207	0.207	0.205	0.184

SI Table 7. Precision and recall scores using a truth dataset containing 5000 sequences from the bacterial RefSeq database (based on 50 randomly selected species and 100 sequences from each).

	superkingdom	phylum	class	order	family	genus	species
precision	1.000	1.000	1.000	0.996	0.992	0.985	0.897
recall	0.052	0.052	0.052	0.052	0.052	0.051	0.047

SI Table 8. Precision and recall scores using a truth dataset containing sequences from a fungal dataset[104] (based on ~5000 sequences).

	domain	phylum	class	order	family	genus	species
precision	1.000	0.990	0.988	0.985	0.961	0.948	0.793
recall	0.207	0.205	0.205	0.204	0.200	0.198	0.171

SI Table 9. Kraken2 precision and recall scores using 3 truth datasets each containing 5000 sequences (50 randomly selected species and 100 sequences from each) from the bacterial RefSeq database, Human Gastrointestinal Bacteria Culture Collection (HBC) and the expanded Human Oral Microbiome Database (HOMD).

Bacterial Refseq

	domain	phylum	class	order	family	genus	species
precision	0.997	0.997	0.997	0.997	0.997	0.997	0.991
recall	0.984	0.983	0.981	0.980	0.979	0.977	0.863

HBC
Gut bacteria

	domain	phylum	class	order	family	genus	species
precision	0.952	0.948	0.944	0.945	0.927	0.929	0.664
recall	0.619	0.606	0.603	0.603	0.586	0.534	0.417

HOMD
Oral bacteria

	domain	phylum	class	order	family	genus	species
precision	0.991	0.990	0.988	0.979	0.973	0.971	0.912
recall	0.767	0.758	0.754	0.752	0.703	0.745	0.635

SI Table 10. Testing the precision of Kraken2 (against nt) classification assignments for a Tabula Sapiens Microbiome sample (Bladder, donor 2). Mean precision and standard deviation for three batches of input sequences selected from the classified reads (100 randomly selected sequences per batch from each domain, excluding Archaea).

Mean Precision +/- SD

	domain	phylum	class	order	family	genus	species
Eukaryotic	0.77 ± 0.04	0.72 ± 0.07	0.61 ± 0.06	0.6 ± 0.06	0.57 ± 0.06	0.54 ± 0.07	0.54 ± 0.07
Bacterial	0.06 ± 0.01	0.06 ± 0.01	0.06 ± 0.01	0.06 ± 0.01	0.06 ± 0.01	0.06 ± 0.01	0.05 ± 0.01
Viral	0.03 ± 0.01	0.03 ± 0.01	0.03 ± 0.02	0.03 ± 0.02	0.03 ± 0.02	0.04 ± 0.03	0.03 ± 0.02

1699 **SI Table 11.** Examples of the type of reads that are misclassified as bacterial by
1700 Kraken2 (against nt) and their classification based on BLASTn (against nt).

kraken2_species	species	kraken2_order	order	kraken2_superkingdom	superkingdom
Pasteurella multocida	Pan paniscus	Pasteurellales	Primates	Bacteria	Eukaryota
Paenibacillus kribbensis	Pan paniscus	Bacillales	Primates	Bacteria	Eukaryota
Kitasatospora sp. MMS16-BH015	Homo sapiens	Streptomycetales	Primates	Bacteria	Eukaryota
Coprothermobacter proteolyticus	Pan paniscus	Coprothermobacterales	Primates	Bacteria	Eukaryota
Desulfovibrio marinus	Homo sapiens	Desulfovibrionales	Primates	Bacteria	Eukaryota
Streptomyces autolyticus	Pan troglodytes	Streptomycetales	Primates	Bacteria	Eukaryota
[Clostridium] cellulosi	Homo sapiens	Clostridiales	Primates	Bacteria	Eukaryota
Citrobacter werkmanii	Homo sapiens	Enterobacterales	Primates	Bacteria	Eukaryota
Deinococcus ficus	Homo sapiens	Deinococcales	Primates	Bacteria	Eukaryota
Methylobacterium durans	Gorilla gorilla	Rhizobiales	Primates	Bacteria	Eukaryota
Pseudomonas putida	Homo sapiens	Pseudomonadales	Primates	Bacteria	Eukaryota
Ectothiorhodospiraceae bacterium BW-2	Pan paniscus	Chromatiales	Primates	Bacteria	Eukaryota
Altererythrobacter sp. TH136	Homo sapiens	Sphingomonadales	Primates	Bacteria	Eukaryota
Nocardioidaceae bacterium	Callithrix jacchus	Propionibacteriales	Primates	Bacteria	Eukaryota
Nakamurella sp. PAMC28650	Macaca mulatta	Nakamurellales	Primates	Bacteria	Eukaryota
Clostridiales bacterium	Pan paniscus	Clostridiales	Primates	Bacteria	Eukaryota
Oceanicoccus sagamiensis	Homo sapiens	Cellvibrionales	Primates	Bacteria	Eukaryota
Qipengyuania seohaensis	Pan paniscus	Sphingomonadales	Primates	Bacteria	Eukaryota
Flammeovirgaceae bacterium	Homo sapiens	Cytophagales	Primates	Bacteria	Eukaryota
Enterobacteriaceae endosymbiont of Donacia ful...	Homo sapiens	Enterobacterales	Primates	Bacteria	Eukaryota
Aeromonas encheleia	Pan paniscus	Aeromonadales	Primates	Bacteria	Eukaryota
Nostoc punctiforme	Pan paniscus	Nostocales	Primates	Bacteria	Eukaryota
Pelagovum pacificum	Homo sapiens	Rhodobacterales	Primates	Bacteria	Eukaryota
Geobacter bemidjiensis	Pan paniscus	Desulfuromonadales	Primates	Bacteria	Eukaryota

1701

1702 **SI Table 12.** List of reagents and instruments per tissue used to generate negative control
1703 samples.

1704 **SI Table 13.** Absolute counts and fraction of total microbial hits, unique hits (based on
1705 UMIs), species, genera, cell-containing droplets with hits, and empty droplets with hits
1706 remaining after each filter is applied.

1707 **SI Table 14.** 95% AUROC confidence intervals for different machine learning models
1708 tested on unseen data. “auroc_test_95perc_ci_lower” and “auroc_test_95perc_ci_upper”
1709 columns correspond to the lower and upper bounds for the 95% confidence interval,
1710 respectively.

	auroc_test_95perc_ci_lower	auroc_test_95perc_ci_upper
gradient boosting classifier	0.82	0.836
random forest	0.785	0.807
multi-layer perceptron	0.765	0.797
support vector rbf	0.733	0.767
knn	0.71	0.758
logistic regression	0.703	0.727

SI Table 15. 95% AUPR confidence intervals for different machine learning models tested on unseen data. “aupr_test_95perc_ci_lower” and “aupr_test_95perc_ci_upper” columns correspond to the lower and upper bounds for the 95% confidence interval, respectively.

	aupr_test_95perc_ci_lower	aupr_test_95perc_ci_upper
gradient boosting classifier	0.748	0.776
random forest	0.715	0.753
multi-layer perceptron	0.69	0.736
support vector rbf	0.668	0.702
knn	0.636	0.69
logistic regression	0.63	0.66

SI Table 16. Evaluating Davinci model’s level of self-consistency to the same input prompt. Three independent outputs are listed for each species. The temperature parameter was set to default (0.5).

SI Table 17. Davinci model outputs for 100 test species using the GEM dataset as the truth dataset. “davinci_0”, “davinci_1”, “davinci_2” columns report the three independent outputs of the Davinci model for each species. “Davinci_human” is set to 0 if a given species is found in humans by at least one of the three Davinci outputs, and 1 otherwise. “Davinci_human_3x” is set to 0 if all three Davinci outputs report that a given species has been found in humans. The “gem_human” column is the truth dataset, set to 0 if a given species is found in humans in the GEM dataset, and 1 otherwise.

SI Table 18. Davinci model outputs for 1500+ species whose habitats were not identified by the HUE datasets. “davinci_0” , “davinci_1”, “davinci_2” columns report the three independent outputs of the Davinci model for each species. “habitat_assignment” column is set to 0 if all three outputs state the presence of a given species in the human body, and set to 1 otherwise.

SI Table 19. Fraction of microbial hits in the TSM F5 and F7 datasets that have taxonomic assignment at different levels of taxonomic categorization.

	index	f5	f7
0	species	1.00	1.00
1	genus	0.88	0.90
2	family	0.92	0.94
3	order	0.96	0.95
4	class	0.97	0.97
5	phylum	0.98	0.99
6	domain	1.00	1.00

SI Table 20. The table underlying the flow paths from **Figure 2.a** (Sankey plot). Columns: source, dest (destination), values. Source and destination columns represent the nodes in the Sankey plot, while the values demonstrate the weight applied onto the connecting edges. The suffixes “_phy”, “_ord”, “_tis”, “_tum”, “_cou”, “_hmp”, “_hab” are denoting phyla, orders, tissues, Nejman *et al.* tumor types, UHGG countries, HMP external facing sites, and GEM habitats, respectively. bm: bone marrow, li: large intestine, si: small intestine.

SI Table 21. Genera found in tumor microbiomes that are not found in the TSM F7 or TSM F5 datasets.

SI Table 22. The table underlying the flow paths from **SI File 2** (Sankey plot). Columns: tumor_type (Nejman *et al.*), genus and tissue (TSM F7), hmp_site (HMP), Country (UHGG), habitat2 (GEM). The suffixes are: “_phy”, “_ord”, “_tis”, “_tum”, “_cou”, “_hmp”, “_hab” are denoting phyla, orders, tissues, Nejman *et al.* tumor types, UHGG countries, HMP external facing sites, and GEM habitats, respectively. bm: bone marrow, li: large intestine, si: small intestine.

SI Table 23. Statistics for the distribution of unique hits per cell ("cell_umi" column) and empty droplets ("empty_umi column) in the TSM F7 dataset.

SI Table 24. Outlier cells with their associated species and domains, as well as their tissue, donor and cell type of origin. BM: Bone Marrow.

SI Table 25. Relative fraction of outlier cells and empty droplets from TSM F7, stratified by the domains where the hits map to. All outlier viral hits from cells and empty droplets map to EBV.

SI Table 26. Outlier cell types in TSM F7 dataset. Fraction and total number of cells in each cell type that had F7 hits are shown. Only cell types with a minimum of 10 cells sequenced are included.

SI Table 27. HERV K (HML-2) transcripts across donors, spanning a diverse range of tissues and cell types.

SI Files

SI File 1. The HTML file that corresponds to **Figure 2.a** (Sankey plot). This file can be opened using a browser for an interactive experience.

SI File 2. The HTML file of a Sankey plot showing the genera shared between several datasets: TSM F7, GEM, UHGG, Nejman et al.). This file can be opened using a browser. Columns from left to right are the same as those from the main Sankey plot (**Figure 2.a**). The suffixes are: "_phy", "_ord", "_tis", "_tum", "_cou", "_hmp", "_hab" are denoting phyla, orders, tissues, Nejman *et al.* tumor types, UHGG countries, HMP external facing sites, and GEM habitats, respectively. bm: bone marrow, li: large intestine, si: small intestine.

SI File 3. The HTML file for the network plot shown in **Figure 3.b**. Please see **Figure 3.b** caption for more information about node and edge weights.

SI File 4. The HTML file for EBV Sankey plot shown in **Figure 4.a**. The columns from left to right correspond to donors, tissues, cell types and compartments. The suffixes for these columns are "_don", "_tis", "_cel", and "_com". bm: bone marrow.

The Tabula Sapiens Consortium Author List

Overall Project Direction and Coordination

Robert C. Jones[1] , Jim Karkanias[2] , Mark Krasnow[3,4], Angela Oliveira Pisco[2] , Stephen R. Quake[1,2,5], Julia Salzman[3,6], Nir Yosef[2,7,8,9]

Donor Recruitment

Bryan Bulthaup[10], Phillip Brown[10], William Harper[10], Marisa Hemenez[10], Ravikumar Ponnusamy[10], Ahmad Salehi[10], Bhavani A. Sanagavarapu[10], Eileen Spallino[10]

Surgeons

Ksenia A. Aaron[11], Waldo Concepcion[10], James M. Gardner[12,13], Burnett Kelly[10,14], Nikole Neidlinger[10], Zifa Wang[10]

Logistical coordination

Sheela Crasta[1,2], Saroja Kolluru[1,2], Maurizio Morri2 , Angela Oliveira Pisco[2] , Serena Y. Tan[15], Kyle J. Travaglini[3] , Chenling Xu[7]

Organ Processing

Marcela Alcántara-Hernández[16], Nicole Almanzar[17], Jane Antony[18], Benjamin Beyersdorf[19], Deviana Burhan[20], Kruti Calcuttawala[21], Matthew M. Carter[16], Charles K. F. Chan[18,22], Charles A. Chang[23], Stephen Chang[3,19], Alex Colville[21,24], Sheela Crasta[1,2], Rebecca N. Culver[25], Ivana Cvijović[1,5], Gaetano D'Amato[26], Camille Ezran[3] , Francisco X. Galdos[18], Astrid Gillich[3] , William R. Goodyer[27], Yan Hang[23,28], Alyssa Hayashi[1] , Sahar Houshdaran[29], Xianxi Huang[19,30], Juan C. Irwin[29], SoRi Jang[3] , Julia Vallve Juanico[29], Aaron M. Kershner[18], Soochi Kim[21,24], Bernhard Kiss[18], Saroja Kolluru[1,2], William Kong[18], Maya E. Kumar[17], Angera H. Kuo[18], Rebecca Leylek[16], Baoxiang Li[31], Gabriel B. Loeb[32], Wan-Jin Lu[18], Sruthi Mantri[33], Maxim Markovic[1] , Patrick L. McAlpine[11,34], Antoine de Morree[21,24], Maurizio Morri[2] , Karim Mrouj[18], Shravani Mukherjee[31], Tyler Muser[17], Patrick Neuhöfer[3,35,36], Thi D. Nguyen[37], Kimberly Perez[16], Ragini Phansalkar[26], Angela Oliveira Pisco[2] , Nazan Puluca[18] , Zhen Qi18, Poorvi Rao[20], Hayley Raquer-McKay[16], Nicholas Schaum[18,21], Bronwyn Scott[31], Bobak Seddighzadeh[38], Joe Segal[20], Sushmita Sen[29], Shaheen Sikandar[18], Sean P. Spencer[16], Lea Steffes[17], Varun R. Subramaniam[31], Aditi Swarup[31], Michael Swift[1], Kyle J. Travaglini[3] , Will Van Treuren[16], Emily Trimm[26], Stefan Veizades[19,39], Sivakamasundari Vijayakumar[18], Kim Chi Vo[29], Sevahn K. Vorperian[1,40], Wanxin

Wang[29], Hannah N.W. Weinstein[38], Juliane Winkler[41], Timothy T.H. Wu[3] , Jamie Xie[38], Andrea R.Yung[3] , Yue Zhang[3]

Sequencing

Angela M. Detweiler[2] , Honey Mekonen[2] , Norma F. Neff[2] , Rene V. Sit[2] , Michelle Tan[2] , Jia Yan[2]

Histology

Gregory R. Bean[15], Vivek Charu[15], Erna Forgó[15], Brock A. Martin[15], Michael G. Ozawa[15], Oscar Silva[15], Serena Y. Tan[15], Angus Toland[15], Venkata N.P. Vemuri[2]

Data Analysis

Shaked Afik[7] , Kyle Awayan[2] , Rob Bierman[3,6], Olga Borisovna Botvinnik[2] , Ashley Byrne[2] , Michelle Chen[1] , Roozbeh Dehghannasiri[3,6], Angela M. Detweiler[2] , Adam Gayoso[7] , Alejandro A Granados[2] , Qiqing Li[2] , Gita Mahmoudabadi[1] , Aaron McGeever[2] , Antoine de Morree[21,24], Julia Eve Olivieri[3,6,42], Madeline Park[2] , Angela Oliveira Pisco[2] , Neha Ravikumar[1] , Julia Salzman[3,6], Geoff Stanley[1] , Michael Swift[1] , Michelle Tan[2] , Weilun Tan[2] , Alexander J Tarashansky[2] , Rohan Vanheusden[2] , Sevahn K. Vorperian[1,40], Peter Wang[3,6], Sheng Wang[2] , Galen Xing[2] , Chenling Xu[6] , Nir Yosef[2,6,7,8]

Expert Cell Type Annotation

Marcela Alcántara-Hernández[16], Jane Antony[18], Charles K. F. Chan[18,22], Charles A. Chang[23], Alex Colville[21,24], Sheela Crasta[1,2], Rebecca Culver[25], Les Dethlefsen[43], Camille Ezran[3] , Astrid Gillich[3] , Yan Hang[23,28], Po-Yi Ho[16], Juan C. Irwin[29], SoRi Jang[3] , Aaron M. Kershner[18], William Kong[18], Maya E Kumar[17], Angera H. Kuo[18], Rebecca Leylek[16], Shixuan Liu[3,44], Gabriel B. Loeb[32], Wan-Jin Lu[18], Jonathan S Maltzman[45,46], Ross J. Metzger[27,47], Antoine de Morree[21,24], Patrick Neuhöfer[3,35,36], Kimberly Perez[16], Ragini Phansalkar[26], Zhen Qi[18], Poorvi Rao[20], Hayley RaquerMcKay[16], Koki Sasagawa[19], Bronwyn Scott[31], Rahul Sinha[15,18,35], Hanbing Song[38], Sean P. Spencer[16], Aditi Swarup[31], Michael Swift[1] , Kyle J. Travaglini[3] , Emily Trimm[26], Stefan Veizades[19,39], Sivakamasundari Vijayakumar[18], Bruce Wang[20], Wanxin Wang[29], Juliane Winkler[41], Jamie Xie[38], Andrea R.Yung[3]

Tissue Expert Principal Investigators

Steven E. Artandi[3,35,36], Philip A. Beachy[18,23,48], Michael F. Clarke[18], Linda C. Giudice[29], Franklin W. Huang[38,49], Kerwyn Casey Huang[1,16], Juliana Idoyaga[16], Seung K Kim[23,28], Mark Krasnow[3,4], Christin S. Kuo[17], Patricia Nguyen[19,39,46], Stephen R. Quake[1,2,5],

Thomas A. Rando[21,24], Kristy Red-Horse[26], Jeremy Reiter[50], David A. Relman[16,43,46], Justin L. Sonnenburg[16], Bruce Wang[20], Albert Wu[31], Sean M. Wu[19,39], Tony Wyss-Coray[21,24]

Affiliations

[1]Department of Bioengineering, Stanford University; Stanford, CA, USA.
[2]Chan Zuckerberg Biohub; San Francisco, CA, USA.
[3]Department of Biochemistry, Stanford University School of Medicine; Stanford, CA, USA.
[4]Howard Hughes Medical Institute; USA.
[5]Department of Applied Physics, Stanford University; Stanford, CA, USA.
[6]Department of Biomedical Data Science, Stanford University; Stanford, CA, USA.
[7]Center for Computational Biology, University of California Berkeley; Berkeley, CA, USA.
[8]Department of Electrical Engineering and Computer Sciences, University of California Berkeley; Berkeley, CA, USA.
[9]Ragon Institute of MGH, MIT and Harvard; Cambridge, MA, USA.
[10]Donor Network West; San Ramon, CA, USA.
[11]Department of Otolaryngology-Head and Neck Surgery, Stanford University School of Medicine; Stanford, California, USA.
[12]Department of Surgery, University of California San Francisco; San Francisco, CA, USA. [13]Diabetes Center, University of California San Francisco; San Francisco, CA, USA.
[14]DCI Donor Services; Sacramento, CA, USA.
[15]Department of Pathology, Stanford University School of Medicine; Stanford, CA, USA.
[16]Department of Microbiology and Immunology, Stanford University School of Medicine; Stanford, CA, USA.
[17]Department of Pediatrics, Division of Pulmonary Medicine, Stanford University; Stanford, CA, USA.
[18]Institute for Stem Cell Biology and Regenerative Medicine, Stanford University School of Medicine; Stanford, CA, USA.
[19]Department of Medicine, Division of Cardiovascular Medicine, Stanford University; Stanford, CA, USA.
[20]Department of Medicine and Liver Center, University of California San Francisco; San Francisco, CA, USA.
[21]Department of Neurology and Neurological Sciences, Stanford University School of Medicine; Stanford, CA, USA.
[22]Department of Surgery - Plastic and Reconstructive Surgery, Stanford University School of Medicine; Stanford, CA, USA.

[23]Department of Developmental Biology, Stanford University School of Medicine, Stanford, CA, USA
[24]Paul F. Glenn Center for the Biology of Aging, Stanford University School of Medicine; Stanford, CA, USA.
[25]Department of Genetics, Stanford University School of Medicine; Stanford, CA, USA.
[26]Department of Biology, Stanford University; Stanford, CA, USA.
[27]Department of Pediatrics, Division of Cardiology, Stanford University School of Medicine; Stanford, CA, USA.
[28]Stanford Diabetes Research Center, Stanford University School of Medicine, Stanford, California
[29]Center for Gynecology and Reproductive Sciences, Department of Obstetrics, Gynecology and Reproductive Sciences, University of California San Francisco; San Francisco, CA, USA. [30]Department of Critical Care Medicine, The First Affiliated Hospital of Shantou University Medical College; Shantou, China.
[31]Department of Ophthalmology, Stanford University School of Medicine; Stanford, CA, USA. [32]Division of Nephrology, Department of Medicine, University of California San Francisco; San Francisco, CA, USA.
[33]Stanford University School of Medicine; Stanford, CA, USA.
[34]Mass Spectrometry Platform, Chan Zuckerberg Biohub; Stanford, CA, USA.
[35]Stanford Cancer Institute, Stanford University School of Medicine; Stanford, CA, USA.
[36]Department of Medicine, Division of Hematology, Stanford University School of Medicine, Stanford, CA, USA
[37]Department of Biochemistry and Biophysics, Cardiovascular Research Institute, University of California San Francisco; San Francisco, CA, USA.
[38]Division of Hematology and Oncology, Department of Medicine, Bakar Computational Health Sciences Institute, Institute for Human Genetics, University of California San Francisco; San Francisco, CA, USA.
[39]Stanford Cardiovascular Institute; Stanford CA, USA.
[40]Department of Chemical Engineering, Stanford University; Stanford, CA, USA.
[41]Department of Cell & Tissue Biology, University of California San Francisco; San Francisco, CA, USA.
[42]Institute for Computational and Mathematical Engineering, Stanford University; Stanford, CA, USA.
[43]Division of Infectious Diseases & Geographic Medicine, Department of Medicine, Stanford University School of Medicine; Stanford, CA, USA.
[44]Department of Chemical and Systems Biology, Stanford University School of Medicine, Stanford, CA, USA
[45]Division of Nephrology, Stanford University School of Medicine; Stanford, CA, USA.
[46]Veterans Affairs Palo Alto Health Care System; Palo Alto, CA, USA.

[47]Vera Moulton Wall Center for Pulmonary and Vascular Disease, Stanford University School of Medicine; Stanford, CA, USA.
[48]Department of Urology, Stanford University School of Medicine, Stanford, CA, USA
[49]Division of Hematology/Oncology, Department of Medicine, San Francisco Veterans Affairs Health Care System, San Francisco, CA, USA.
[50]Department of Biochemistry, University of California San Francisco; San Francisco, CA, USA.

Citations

1. Lynch, M. & Marinov, G. K. The bioenergetic costs of a gene. *Proc. Natl. Acad. Sci. U. S. A.* **112**, 15690–15695 (2015).
2. Mahmoudabadi, G., Milo, R. & Phillips, R. Energetic cost of building a virus. *Proc. Natl. Acad. Sci.* **114**, E4324–E4333 (2017).
3. Gilbert, J. *et al.* Current understanding of the human microbiome. *Nat. Med.* **24**, 392–400 (2018).
4. Lloyd-Price, J. *et al.* Strains, functions and dynamics in the expanded Human Microbiome Project. *Nature* **550**, 61–66 (2017).
5. Almeida, A. *et al.* A unified catalog of 204,938 reference genomes from the human gut microbiome. *Nat. Biotechnol.* **39**, 105–114 (2021).
6. Mahmoudabadi, G. & Phillips, R. A comprehensive and quantitative exploration of thousands of viral genomes. *eLife* **7**, e31955 (2018).
7. Nayfach, S. *et al.* A genomic catalog of Earth's microbiomes. *Nat. Biotechnol.* **39**, 499–509 (2021).
8. Kowarsky, M. *et al.* Numerous uncharacterized and highly divergent microbes which colonize humans are revealed by circulating cell-free DNA. *Proc. Natl. Acad. Sci.* **114**, 9623–9628 (2017).
9. Dickson, R. P., Erb-Downward, J. R., Martinez, F. J. & Huffnagle, G. B. The Microbiome and the Respiratory Tract. *Annu. Rev. Physiol.* **78**, 481–504 (2016).

1945 10. Turnbaugh, P. J. *et al.* A core gut microbiome in obese and lean twins. *Nature* **457**, 480–
1946 484 (2009).
1947 11. Qin, J. *et al.* A metagenome-wide association study of gut microbiota in type 2 diabetes.
1948 *Nature* **490**, 55–60 (2012).
1949 12. Cryan, J. F., O'Riordan, K. J., Sandhu, K., Peterson, V. & Dinan, T. G. The gut microbiome
1950 in neurological disorders. *Lancet Neurol.* **19**, 179–194 (2020).
1951 13. Sharon, G. *et al.* Human Gut Microbiota from Autism Spectrum Disorder Promote
1952 Behavioral Symptoms in Mice. *Cell* **177**, 1600-1618.e17 (2019).
1953 14. Asnicar, F. *et al.* Microbiome connections with host metabolism and habitual diet from 1,098
1954 deeply phenotyped individuals. *Nat. Med.* **27**, 321–332 (2021).
1955 15. Jie, Z. *et al.* The gut microbiome in atherosclerotic cardiovascular disease. *Nat. Commun.* **8**,
1956 845 (2017).
1957 16. Fujimura, K. E. *et al.* Neonatal gut microbiota associates with childhood multisensitized
1958 atopy and T cell differentiation. *Nat. Med.* **22**, 1187–1191 (2016).
1959 17. Wolter, M. *et al.* Leveraging diet to engineer the gut microbiome. *Nat. Rev. Gastroenterol.*
1960 *Hepatol.* 1–18 (2021) doi:10.1038/s41575-021-00512-7.
1961 18. Poore, G. D. *et al.* Microbiome analyses of blood and tissues suggest cancer diagnostic
1962 approach. *Nature* **579**, 567–574 (2020).
1963 19. Dohlman, A. B. *et al.* The cancer microbiome atlas: a pan-cancer comparative analysis to
1964 distinguish tissue-resident microbiota from contaminants. *Cell Host Microbe* **29**, 281-298.e5
1965 (2021).
1966 20. Narunsky-Haziza, L. *et al.* Pan-cancer analyses reveal cancer-type-specific fungal ecologies
1967 and bacteriome interactions. *Cell* **185**, 3789-3806.e17 (2022).
1968 21. Nejman, D. *et al.* The human tumor microbiome is composed of tumor type-specific
1969 intracellular bacteria. *Science* **368**, 973–980 (2020).
1970 22. Riquelme, E. *et al.* Tumor Microbiome Diversity and Composition Influence Pancreatic

1971 Cancer Outcomes. *Cell* **178**, 795-806.e12 (2019).
1972 23. Ghaddar, B. *et al.* Tumor microbiome links cellular programs and immunity in pancreatic
1973 cancer. *Cancer Cell* **40**, 1240-1253.e5 (2022).
1974 24. Aykut, B. *et al.* The fungal mycobiome promotes pancreatic oncogenesis via activation of
1975 MBL. *Nature* **574**, 264–267 (2019).
1976 25. Tzeng, A. *et al.* Human breast microbiome correlates with prognostic features and
1977 immunological signatures in breast cancer. *Genome Med.* **13**, 60 (2021).
1978 26. Hieken, T. J. *et al.* The Microbiome of Aseptically Collected Human Breast Tissue in Benign
1979 and Malignant Disease. *Sci. Rep.* **6**, 30751 (2016).
1980 27. Shao, D. *et al.* Microbial characterization of esophageal squamous cell carcinoma and
1981 gastric cardia adenocarcinoma from a high-risk region of China. *Cancer* **125**, 3993–4002
1982 (2019).
1983 28. THE TABULA SAPIENS CONSORTIUM. The Tabula Sapiens: A multiple-organ, single-cell
1984 transcriptomic atlas of humans. *Science* **376**, eabl4896 (2022).
1985 29. Forster, S. C. *et al.* A human gut bacterial genome and culture collection for improved
1986 metagenomic analyses. *Nat. Biotechnol.* **37**, 186–192 (2019).
1987 30. HOMD :: Human Oral Microbiome Database. https://www.homd.org/.
1988 31. Davis, J. J. *et al.* The PATRIC Bioinformatics Resource Center: expanding data and
1989 analysis capabilities. *Nucleic Acids Res.* **48**, D606–D612 (2020).
1990 32. Mölder, F. *et al.* Sustainable data analysis with Snakemake. *F1000Research* **10**, 33 (2021).
1991 33. Smith, T. S., Heger, A. & Sudbery, I. UMI-tools: Modelling sequencing errors in Unique
1992 Molecular Identifiers to improve quantification accuracy. *Genome Res.* gr.209601.116
1993 (2017) doi:10.1101/gr.209601.116.
1994 34. Dobin, A. *et al.* STAR: ultrafast universal RNA-seq aligner. *Bioinformatics* **29**, 15–21 (2013).
1995 35. Altschul, S. F., Gish, W., Miller, W., Myers, E. W. & Lipman, D. J. Basic local alignment
1996 search tool. *J. Mol. Biol.* **215**, 403–410 (1990).

1997 36. Salter, S. J. *et al.* Reagent and laboratory contamination can critically impact sequence-
1998 based microbiome analyses. *BMC Biol.* **12**, 87 (2014).
1999 37. Woellmer, A. & Hammerschmidt, W. Epstein-Barr virus and host cell methylation:
2000 Regulation of latency, replication and virus reactivation. *Curr. Opin. Virol.* **3**, 260–265
2001 (2013).
2002 38. Tierney, R. J., Shannon-Lowe, C. D., Fitzsimmons, L., Bell, A. I. & Rowe, M. Unexpected
2003 patterns of Epstein–Barr virus transcription revealed by a High throughput PCR array for
2004 absolute quantification of viral mRNA. *Virology* **474**, 117–130 (2015).
2005 39. Forbes, J. D., Bernstein, C. N., Tremlett, H., Van Domselaar, G. & Knox, N. C. A Fungal
2006 World: Could the Gut Mycobiome Be Involved in Neurological Disease? *Front. Microbiol.* **9**,
2007 3249 (2019).
2008 40. Qin, J. *et al.* A human gut microbial gene catalogue established by metagenomic
2009 sequencing. *Nature* **464**, 59–65 (2010).
2010 41. Al Bataineh, M. T. *et al.* Revealing links between gut microbiome and its fungal community
2011 in Type 2 Diabetes Mellitus among Emirati subjects: A pilot study. *Sci. Rep.* **10**, 9624
2012 (2020).
2013 42. Milo, R. & Phillips, R. *Cell Biology by the numbers*. (Garland Science, 2015).
2014 doi:10.1201/9780429258770.
2015 43. Schaechter, M., MaalØe, O. & Kjeldgaard, N. O. Y. 1958. Dependency on Medium and
2016 Temperature of Cell Size and Chemical Composition during Balanced Growth of Salmonella
2017 typhimurium. *Microbiology* **19**, 592–606.
2018 44. Scott, M., Gunderson, C. W., Mateescu, E. M., Zhang, Z. & Hwa, T. Interdependence of cell
2019 growth and gene expression: origins and consequences. *Science* **330**, 1099–1102 (2010).
2020 45. Milo, R., Jorgensen, P., Moran, U., Weber, G. & Springer, M. BioNumbers--the database of
2021 key numbers in molecular and cell biology. *Nucleic Acids Res.* **38**, D750-753 (2010).
2022 46. Grimm, C., Bartuli, J. & Fischer, U. Cytoplasmic gene expression: lessons from poxviruses.

2023 *Trends Biochem. Sci.* (2022) doi:10.1016/j.tibs.2022.04.010.
2024 47. Wylie, S. J., Luo, H., Li, H. & Jones, M. G. K. Multiple polyadenylated RNA viruses detected
2025 in pooled cultivated and wild plant samples. *Arch. Virol.* **157**, 271–284 (2012).
2026 48. Hajnsdorf, E. & Kaberdin, V. R. RNA polyadenylation and its consequences in prokaryotes.
2027 *Philos. Trans. R. Soc. B Biol. Sci.* **373**, 20180166 (2018).
2028 49. Maes, A. *et al.* Landscape of RNA polyadenylation in E. coli. *Nucleic Acids Res.* **45**, 2746–
2029 2756 (2017).
2030 50. Ozsolak, F. *et al.* Comprehensive Polyadenylation Site Maps in Yeast and Human Reveal
2031 Pervasive Alternative Polyadenylation. *Cell* **143**, 1018–1029 (2010).
2032 51. Mayer, A. *et al.* Native Elongating Transcript Sequencing Reveals Human Transcriptional
2033 Activity at Nucleotide Resolution. *Cell* **161**, 541–554 (2015).
2034 52. Chukkapalli, S. S. *et al.* Invasion of Oral and Aortic Tissues by Oral Spirochete Treponema
2035 denticola in ApoE−/− Mice Causally Links Periodontal Disease and Atherosclerosis. *Infect.*
2036 *Immun.* **82**, 1959–1967 (2014).
2037 53. Santos, P. B. do R. E. dos *et al.* Review- The periodontal pathogen Treponema denticola:
2038 an atherosclerosis risk factor. *Res. Soc. Dev.* **10**, e25810111637–e25810111637 (2021).
2039 54. Okuda, K. *et al.* Detection of Treponema denticola in Atherosclerotic Lesions. *J. Clin.*
2040 *Microbiol.* (2001) doi:10.1128/JCM.39.3.1114-1117.2001.
2041 55. Schenkein, H. A., Papapanou, P. N., Genco, R. & Sanz, M. Mechanisms underlying the
2042 association between periodontitis and atherosclerotic disease. *Periodontol. 2000* **83**, 90–
2043 106 (2020).
2044 56. Young, L. S., Yap, L. F. & Murray, P. G. Epstein–Barr virus: more than 50 years old and still
2045 providing surprises. *Nat. Rev. Cancer* **16**, 789–802 (2016).
2046 57. Dunmire, S. K., Verghese, P. S. & Balfour, H. H. Primary Epstein-Barr virus infection. *J.*
2047 *Clin. Virol.* **102**, 84–92 (2018).
2048 58. Thorley-Lawson, D. A. EBV Persistence—Introducing the Virus. in *Epstein Barr Virus*

2049 *Volume 1: One Herpes Virus: Many Diseases* (ed. Münz, C.) 151–209 (Springer
2050 International Publishing, 2015). doi:10.1007/978-3-319-22822-8_8.
2051 59. Smatti, M. K. *et al.* Epstein–Barr Virus Epidemiology, Serology, and Genetic Variability of
2052 LMP-1 Oncogene Among Healthy Population: An Update. *Front. Oncol.* **8**, 211 (2018).
2053 60. Bjornevik, K. *et al.* Longitudinal analysis reveals high prevalence of Epstein-Barr virus
2054 associated with multiple sclerosis. *Science* (2022) doi:10.1126/science.abj8222.
2055 61. Narita, Y. *et al.* Pin1 Interacts with the Epstein-Barr Virus DNA Polymerase Catalytic
2056 Subunit and Regulates Viral DNA Replication. *J. Virol.* **87**, 2120–2127 (2013).
2057 62. van Zyl, D. G., Mautner, J. & Delecluse, H.-J. Progress in EBV Vaccines. *Front. Oncol.* **9**,
2058 104 (2019).
2059 63. Chiu, S.-H. *et al.* Epstein-Barr Virus BALF3 Has Nuclease Activity and Mediates Mature
2060 Virion Production during the Lytic Cycle. *J. Virol.* **88**, 4962–4975 (2014).
2061 64. Wen, W. *et al.* Epstein-Barr Virus BZLF1 Gene, a Switch from Latency to Lytic Infection, Is
2062 Expressed as an Immediate-Early Gene after Primary Infection of B Lymphocytes. *J. Virol.*
2063 **81**, 1037–1042 (2007).
2064 65. Dervan, E., Bhattacharyya, D. D., McAuliffe, J. D., Khan, F. H. & Glynn, S. A. Ancient
2065 Adversary – HERV-K (HML-2) in Cancer. *Front. Oncol.* **11**, 1707 (2021).
2066 66. Agoni, L., Guha, C. & Lenz, J. Detection of Human Endogenous Retrovirus K (HERV-K)
2067 Transcripts in Human Prostate Cancer Cell Lines. *Front. Oncol.* **3**, 180 (2013).
2068 67. Chan, S. M. *et al.* The HERV-K accessory protein Np9 controls viability and migration of
2069 teratocarcinoma cells. *PLOS ONE* **14**, e0212970 (2019).
2070 68. Grow, E. J. *et al.* Intrinsic retroviral reactivation in human preimplantation embryos and
2071 pluripotent cells. *Nature* **522**, 221–225 (2015).
2072 69. Wang, T. *et al.* Regulation of stem cell function and neuronal differentiation by HERV-K via
2073 mTOR pathway. *Proc. Natl. Acad. Sci.* **117**, 17842–17853 (2020).
2074 70. Adawi, D., Molin, G. & Jeppsson, B. Gut–liver axis. *HPB* **1**, 173–186 (1999).

2075 71. Tripathi, A. *et al.* The gut–liver axis and the intersection with the microbiome. *Nat. Rev.*
2076 *Gastroenterol. Hepatol.* **15**, 397–411 (2018).
2077 72. Nguyen, S. *et al.* Bacteriophage Transcytosis Provides a Mechanism To Cross Epithelial
2078 Cell Layers. *mBio* **8**, e01874-17.
2079 73. Zhou, C.-B., Zhou, Y.-L. & Fang, J.-Y. Gut Microbiota in Cancer Immune Response and
2080 Immunotherapy. *Trends Cancer* **7**, 647–660 (2021).
2081 74. York, A. Gut microbiota sways response to cancer immunotherapy. *Nat. Rev. Microbiol.* **16**,
2082 121–121 (2018).
2083 75. Martel, C. de, Georges, D., Bray, F., Ferlay, J. & Clifford, G. M. Global burden of cancer
2084 attributable to infections in 2018: a worldwide incidence analysis. *Lancet Glob. Health* **8**,
2085 e180–e190 (2020).
2086 76. Evans, E. L., Becker, J. T., Fricke, S. L., Patel, K. & Sherer, N. M. HIV-1 Vif's Capacity To
2087 Manipulate the Cell Cycle Is Species Specific. *J. Virol.* **92**, e02102-17.
2088 77. Fan, Y., Sanyal, S. & Bruzzone, R. Breaking Bad: How Viruses Subvert the Cell Cycle.
2089 *Front. Cell. Infect. Microbiol.* **8**, 396 (2018).
2090 78. Gagnaire, A., Nadel, B., Raoult, D., Neefjes, J. & Gorvel, J.-P. Collateral damage: insights
2091 into bacterial mechanisms that predispose host cells to cancer. *Nat. Rev. Microbiol.* **15**,
2092 109–128 (2017).
2093 79. Russell, A. B., Trapnell, C. & Bloom, J. D. Extreme heterogeneity of influenza virus infection
2094 in single cells. *eLife* **7**, e32303 (2018).
2095 80. Zanini, F., Pu, S.-Y., Bekerman, E., Einav, S. & Quake, S. R. Single-cell transcriptional
2096 dynamics of flavivirus infection. *eLife* **7**, e32942 (2018).
2097 81. Xue, Y. *et al.* A single-parasite transcriptional atlas of Toxoplasma Gondii reveals novel
2098 control of antigen expression. *eLife* **9**, e54129 (2020).
2099 82. Weynberg, K. D., Wood-Charlson, E. M., Suttle, C. A. & van Oppen, M. J. H. Generating
2100 viral metagenomes from the coral holobiont. *Front. Microbiol.* **5**, 206 (2014).

2101 83. Wang, Q. *et al.* Computational methods and challenges in analyzing intratumoral
2102 microbiome data. *Trends Microbiol.* S0966842X23000306 (2023)
2103 doi:10.1016/j.tim.2023.01.011.
2104 84. Robinson, W. *et al.* scRNA-seq analysis of colon and esophageal tumors uncovers
2105 abundant microbial reads in myeloid cells undergoing proinflammatory transcriptional
2106 alterations. 2020.05.14.096230 Preprint at https://doi.org/10.1101/2020.05.14.096230
2107 (2023).
2108 85. Lloréns-Rico, V. *et al.* Clinical practices underlie COVID-19 patient respiratory microbiome
2109 composition and its interactions with the host. *Nat. Commun.* **12**, 6243 (2021).
2110 86. Walker, M. A. *et al.* GATK PathSeq: a customizable computational tool for the discovery and
2111 identification of microbial sequences in libraries from eukaryotic hosts. *Bioinformatics* **34**,
2112 4287–4289 (2018).
2113 87. Zhu, K. *et al.* Strain level microbial detection and quantification with applications to single
2114 cell metagenomics. *Nat. Commun.* **13**, 6430 (2022).
2115 88. Morgulis, A. & Agarwala, R. SRPRISM (Single Read Paired Read Indel Substitution
2116 Minimizer): an efficient aligner for assemblies with explicit guarantees. *GigaScience* **9**,
2117 giaa023 (2020).
2118 89. Kostic, A. D. *et al.* PathSeq: software to identify or discover microbes by deep sequencing of
2119 human tissue. *Nat. Biotechnol.* **29**, 393–396 (2011).
2120 90. Shen, W. & Ren, H. TaxonKit: A practical and efficient NCBI taxonomy toolkit. *J. Genet.*
2121 *Genomics* **48**, 844–850 (2021).
2122 91. Ye, S. H., Siddle, K. J., Park, D. J. & Sabeti, P. C. Benchmarking Metagenomics Tools for
2123 Taxonomic Classification. *Cell* **178**, 779–794 (2019).
2124 92. McIntyre, A. B. R. *et al.* Comprehensive benchmarking and ensemble approaches for
2125 metagenomic classifiers. *Genome Biol.* **18**, 182 (2017).
2126 93. Bazinet, A. L., Ondov, B. D., Sommer, D. D. & Ratnayake, S. BLAST-based validation of

2127 metagenomic sequence assignments. *PeerJ* **6**, e4892 (2018).
2128 94. Wood, D. E. & Salzberg, S. L. Kraken: ultrafast metagenomic sequence classification using
2129 exact alignments. *Genome Biol.* **15**, R46 (2014).
2130 95. Liebhoff, A.-M. *et al.* Pathogen detection in RNA-seq data with Pathonoia. *BMC*
2131 *Bioinformatics* **24**, 53 (2023).
2132 96. Jurado-Rueda, F. *et al.* Benchmarking of microbiome detection tools on RNA-seq synthetic
2133 databases according to diverse conditions. *Bioinforma. Adv.* **3**, vbad014 (2023).
2134 97. O'Leary, N. A. *et al.* Reference sequence (RefSeq) database at NCBI: current status,
2135 taxonomic expansion, and functional annotation. *Nucleic Acids Res.* **44**, D733-745 (2016).
2136 98. Huntemann, M. *et al.* The standard operating procedure of the DOE-JGI Microbial Genome
2137 Annotation Pipeline (MGAP v.4). *Stand. Genomic Sci.* **10**, 86 (2015).
2138 99. Schulz, F. *et al.* Hidden diversity of soil giant viruses. *Nat. Commun.* **9**, 4881 (2018).
2139 100. González-Pech, R. A., Stephens, T. G. & Chan, C. X. Commonly misunderstood
2140 parameters of NCBI BLAST and important considerations for users. *Bioinformatics* **35**,
2141 2697–2698 (2019).
2142 101. Hung, J.-H. & Weng, Z. Sequence Alignment and Homology Search with BLAST and
2143 ClustalW. *Cold Spring Harb. Protoc.* **2016**, pdb.prot093088 (2016).
2144 102. Hiseni, P., Rudi, K., Wilson, R. C., Hegge, F. T. & Snipen, L. HumGut: a comprehensive
2145 human gut prokaryotic genomes collection filtered by metagenome data. *Microbiome* **9**, 165
2146 (2021).
2147 103. Tiew, P. Y. *et al.* The Mycobiome in Health and Disease: Emerging Concepts,
2148 Methodologies and Challenges. *Mycopathologia* **185**, 207–231 (2020).
2149 104. Nash, A. K. *et al.* The gut mycobiome of the Human Microbiome Project healthy cohort.
2150 *Microbiome* **5**, 153 (2017).
2151 105. Wood, D. E., Lu, J. & Langmead, B. Improved metagenomic analysis with Kraken 2.
2152 *Genome Biol.* **20**, 257 (2019).

2153 106. Chawla, N. V., Bowyer, K. W., Hall, L. O. & Kegelmeyer, W. P. SMOTE: synthetic
2154 minority over-sampling technique. *J. Artif. Intell. Res.* **16**, 321–357 (2002).
2155 107. Lopes, M. & Bontempi, G. *On the Null Distribution of the Precision and Recall Curve*.
2156 337 (2014). doi:10.1007/978-3-662-44851-9_21.
2157 108. Zou, Y. *et al.* 1,520 reference genomes from cultivated human gut bacteria enable
2158 functional microbiome analyses. *Nat. Biotechnol.* **37**, 179–185 (2019).
2159 109. Chen, I.-M. A. *et al.* IMG/M v.5.0: an integrated data management and comparative
2160 analysis system for microbial genomes and microbiomes. *Nucleic Acids Res.* **47**, D666–
2161 D677 (2019).
2162 110. Pasolli, E. *et al.* Extensive Unexplored Human Microbiome Diversity Revealed by Over
2163 150,000 Genomes from Metagenomes Spanning Age, Geography, and Lifestyle. *Cell* **176**,
2164 649-662.e20 (2019).
2165 111. Carrero, P. *et al.* Report of six cases of human infection by Serratia plymuthica. *J. Clin.*
2166 *Microbiol.* **33**, 275–276 (1995).
2167 112. Al-Sardi, M., Radwan, H., Itbaileh, A. B. & AlMusa, Z. Leifsonia Species Bacteremia in a
2168 Hemodialysis Patient: A Difficult-to-Identify Organism. *Cureus* **13**, e17994.
2169 113. Rickettsia Japonica - an overview | ScienceDirect Topics.
2170 https://www.sciencedirect.com/topics/medicine-and-dentistry/rickettsia-japonica.
2171 114. Bai, H. *et al.* Lysobacter oculi sp. nov., isolated from human Meibomian gland
2172 secretions. *Antonie Van Leeuwenhoek* **113**, 13–20 (2020).
2173 115. Shkoporov, A. N. *et al.* The Human Gut Virome Is Highly Diverse, Stable, and Individual
2174 Specific. *Cell Host Microbe* **26**, 527-541.e5 (2019).
2175 116. Franzosa, E. A. *et al.* Identifying personal microbiomes using metagenomic codes. *Proc.*
2176 *Natl. Acad. Sci.* (2015) doi:10.1073/pnas.1423854112.
2177 117. Integrative HMP (iHMP) Research Network Consortium. The Integrative Human
2178 Microbiome Project: dynamic analysis of microbiome-host omics profiles during periods of

2179 human health and disease. *Cell Host Microbe* **16**, 276–289 (2014).

2180 118. Glass, J. I. *et al.* The complete sequence of the mucosal pathogen Ureaplasma

2181 urealyticum. *Nature* **407**, 757–762 (2000).

2182 119. Lindholm, M., Min Aung, K., Nyunt Wai, S. & Oscarsson, J. Role of OmpA1 and OmpA2

2183 in Aggregatibacter actinomycetemcomitans and Aggregatibacter aphrophilus serum

2184 resistance. *J. Oral Microbiol.* **11**, 1536192 (2019).